ABSTRACT

Title of Dissertation: INVESTIGATIONS INTO THE NATURE, SEVERITY, AND IMPACT OF PYROCUMULONIMBUS

Michael David Fromm, Doctor of Philosophy, 2008

Dissertation directed by: Professor Zhanqing Li
Department of Atmospheric and Oceanic Science &
Earth System Science Interdisciplinary Center

Pyrocumulonimbus (pyroCb) storms have been shown to have an eruptive dynamic and capacity similar to volcanic eruptions that penetrate into the stratosphere. Much remains unknown about pyroCb, for instance its storm structure, frequency, impact on satellite cloud imagery, and impact on regional/hemispheric climate. This study pursues in-depth exploration of pyroCb using observational data analysis and modeling. The observational aspect of this research will be founded in satellite data from imagers and profilers, going back to the late 1970s. These data are examined for clues that will eventually allow the characterization of a pyroCb-frequency climatology. The particular data sets include Total Ozone Mapping Spectrometer (TOMS) and Ozone Monitoring Instrument (OMI) aerosol index, nadir imagery in the visible and infrared, and aerosol profiles. In addition, available ground-based data (such as lidar) are also exploited. PyroCb radiative impact is explored by combining aerosol optical depth data with a long-term Microwave Sounding Unit (MSU) and radiosonde temperature archive and a radiative transfer model. This work comprises studies of two pyroCb events, in the southern and northern hemisphere, and an analysis of the radiative impact of stratospheric smoke comprising two seasons with multiple pyroCbs. The major findings include the revelation that pyroCb can generate tornadoes, significantly suppress precipitation due to super-abundance of condensation nuclei, increase by factors of 2 to 5 the zonal average stratospheric aerosol optical depth, pollute air mass regimes from tropics to polar, and perturb zonal average stratospheric temperature.

INVESTIGATIONS INTO THE NATURE, SEVERITY, AND IMPACT OF PYROCUMULONIMBUS

by

Michael David Fromm

Dissertation submitted to the Faculty of the Graduate School of the
University of Maryland, College Park in partial fulfillment
of the requirements for the degree of
Doctor of Philosophy
2008

Advisory Committee:

Professor Zhanqing Li, Advisor
Professor Russell Dickerson
Professor Robert D. Hudson
Professor Daniel Kirk-Davidoff
Professor Eric Kasischke

Acknowledgements

I am indebted to my advisor, Professor Zhanqing Li, who has provided continual, invaluable assistance to me. He has enabled me to pursue my educational goals while maintaining full-time employment, and facilitated entry into the doctoral program for me and similarly experienced professional scientists. I am deeply grateful to John Cahir, my graduate school advisor at Penn State, who encouraged me to pursue the Ph.D. and provided assistance in my application for candidacy. Kwon-Ho Lee has collaborated on an important aspect of my Ph.D. research, allowing me to pursue a critical line of investigation. My gratitude is also extended to co-authors of published papers that are central to this Ph.D. project. They are Andrew Tupper, Daniel Rosenfeld, Rick McRae, René Servranckx, Eric Shettle, Omar Torres, David Diner, Brian Vant-Hull, K. H. Fricke, Christoph Ritter, Thomas Trickl, Helmut Giehl, Michael Gerding, John Barnes, Michael O'Neill, Steven Massie, Ulrich Blum, Stuart McDermid, Thierry Leblanc, and Terry Deshler. Melanie Follette's help with formatting this document is gratefully acknowledged. This research was funded by a grant from the NASA Radiation Science Program.

Statement of Originality

The research reported herein is original in its entirety. It has been exclusively initiated and completed by Michael David Fromm (MDF), who bears all responsibility for the content herein. The following peer-reviewed publications have been completed while MDF has been a Ph.D. candidate.

Fromm M., A. Tupper, D. Rosenfeld, R. Servranckx, R. McRae (2006), Violent pyro-convective storm devastates Australia's capital and pollutes the stratosphere, Geophys. Res. Lett., 33, L05815, doi:10.1029/2005GL025161.

Fromm, M., E. P. Shettle, K. H. Fricke, C. Ritter, T. Trickl, H. Giehl, M. Gerding, J. Barnes, M. O'Neill, S. T. Massie, U. Blum, I. S. McDermid, T. Leblanc, and T. Deshler (2008), The stratospheric impact of the Chisholm PyroCumulonimbus eruption: Part II, vertical profile perspective, J. Geophys. Res., doi:10.1029/2007JD009147.

Fromm, M., O. Torres, D. J. Diner, D. Lindsey, **B. Vant-Hull**, R. Servranckx, E. P. Shettle, and **Z. Li** (2008), Stratospheric impact of the Chisholm pyrocumulonimbus eruption: 1. Earth-viewing satellite perspective, J. Geophys. Res., doi:10.1029/2007JD009153.

Fromm, M., **Z. Li**, and **K. H. Lee**, Pyrocumulonimbus eruptions warm the stratosphere and cool the troposphere on a hemispheric scale, to be submitted, (2008).

Summary of original findings reported herein:

- pyrocumulonimbus (pyroCb) storms have greatly suppressed cloud particle size, little precipitation, and can spawn destructive tornaodoes.
- pyroCb also occur in southern midlatitudes
- doubled zonal average stratospheric aerosol optical depth attributed to southern hemisphere pyroCb in January 2003 and Canadian pyroCb in May 2001
- smoke mass injected by single pyroCb into lower stratosphere ~20,000 t.
- transport into lower stratosphere contains smoke-ice mixture
- stratospheric smoke transport from a single pycoCb from polar to tropical meteorological regimes
- observations and modeling indicate a zonal average warming of the stratosphere and possible tropospheric cooling associated with pyroCb smoke.

Table of Contents

Acronyms and Abbreviations

ACT	Australian Capital Territory
AI	Aerosol Index
amsl	above mean sea level
AMSU	Advanced Microwave Sounding Unit
AOD	Aerosol Optical Depth
BOM	Bureau Of Meteorology
BT	Brightness Temperature
BTD	Brightness Temperature Difference
CALIPSO	Cloud-Aerosol Lidar and Infrared Pathfinder Satellite Observation
CFC	ChloroFluoroCarbon
CTP	Cloud-Top Pressure
CRYSTAL-FACE	Cirrus Regional Study of Tropical Anvils and cirrus Layers – Florida Area Cirrus Experiment
GOES	Geostationary Operational Environmental Satellite
HALOE	HALogen Occultation Experiment
IR	InfraRed
JPL	Jet Propulsion Laboratory
LMS	LowerMost Stratosphere
LST	Lower Stratospheric Temperature
LTT	Lower Tropospheric Temperature
MISR	Multi-angle Imaging SpectroRadiometer
MLO	Mauna LOa
MLS	Microwave Limb Sounder
MODIS	MODerate resolution Imaging Spectroradiometer
MPLNET	Micro-Pulse lidar NETwork
MSU	Microwave Sounding Unit
NASA	National Aeronautics and Space Administration
NCEP	National Centers for Environmental Prediction
NDACC	Network for the Detection of Atmospheric Composition Change
NDSC	Network for the Detection of Stratospheric Change
Nd:YAG	Neodymium-doped Yttrium Aluminum Garnet
NOAA	National Oceanic and Atmospheric Administration
NOAA/ESRL	NOAA/ Earth System Research Laboratory
NOAA/GMD	NOAA/Global Monitoring Division
NT	Northwest Territories
OCS	carbonyl sulfide
OPC	Optical Particle Counter
POAM	Polar Ozone and Aerosol Measurement
PPI	Plan Position Indicator
PSC	Polar Stratospheric Cloud
pv	potential vorticity
pyroCb	pyrocumulonimbus
RHI	Range Height Indicator

RMR	Rayleigh/Mie/Raman
SAGE	Stratospheric Aerosol and Gas Experiment
SBDART	Santa Barbara DISORT Atmospheric Radiative Transfer
SO	Solar Occultation
SPARC	Stratospheric Processes And their Role in Climate
SVC	SubVisual Cirrus
THIR	THermal IR
TOMS	Total Ozone Mapping Spectrometer
TNT	TriNitroToluene
TPM	Total Particulate Matter
UARS	Upper Atmosphere Research Satellite
UTC	Coordinated Universal Time
UTLS	Upper Troposphere, Lower Stratosphere
UV	UltraViolet
WGS84	World Geodetic System earth reference frame revised in 1984

List of Tables

List of Figures

Chapter 1: Introduction

Wild fires sometimes achieve sufficient size and heat energy to spawn pyroconvective storms that penetrate well into the lower stratosphere. Fire emissions at such altitudes will remain in the atmosphere for long periods. The episodic introduction of smoke and other biomass burning effluents to the upper troposphere and lower stratosphere thus alters the "normal" composition there and can have an important chemical or radiative impact. The discovery of this phenomenon, called pyrocumulonimbus (pyroCb for short), is relatively recent [Fromm et al., 2000]. This dissertation's subject is a characterization of the physical effects, geographic scope and radiative impact of these special pyroconvective storms.

It has long been accepted that there are only two major sources of stratospheric aerosol [Brasseur and Solomon, 1986]:

1. slow upward transport of carbonyl sulfide (OCS) generated at the surface and eventually oxidized into sulfuric acid droplets, and
2. injection of ash and SO_2 (which subsequently produces sulfuric acid droplets) from volcanic eruptions.

Even the recently released SPARC Aerosol Assessment [SPARC, 2006] constrains stratospheric aerosol processes to those mentioned above. Now it is recognized that extreme pyroconvection, spawned by a combination of heating due to forest fires and weather disturbances, must be added to this list of sources of stratospheric aerosol. However, the global magnitude of this source, compared to the other known sources, is by no means clear. It is also important to point out that the implications of the stratospheric forest fire smoke discovery are not limited to the stratospheric aerosol budget. Transport of material (both aerosol and gaseous compounds) from the troposphere to the stratosphere is a key issue in atmospheric science for a number of reasons. For example, the global ozone depletion problem is primarily the result of the transport into the stratosphere of chlorofluorocarbons (CFC) produced anthropogenically and released into the atmosphere near the surface. These chemicals are inert and long-lived in the troposphere, but become photochemically

active in the stratosphere, and take part in catalytic chemical cycles that destroy ozone. In addition, the transport of greenhouse gases into the stratosphere is a critical part of the atmospheric global warming conundrum. It is generally assumed in models used to study these phenomena that transport from the troposphere to the stratosphere occurs only in the tropics--outside of the tropics only transport from the stratosphere to the troposphere is considered. The discovery of pyroCb shows that the extratropical tropopause is not an iron lid, and that transport across it can and does occur.

The discovery of smoke from boreal forest fires in the stratosphere [Fromm et al., 2000] is fundamental in atmospheric science, with far reaching potential implications in many important areas including climatology and atmospheric chemistry. First, aerosols in the atmosphere reflect light from the sun back to space, resulting in a cooling of the earth's surface. Moreover, these carbonaceous aerosols absorb a considerable amount of sunlight, which will induce local warming and perhaps self lofting. The added significance of stratospheric aerosols is that, in the stratosphere, aerosols can be efficiently disbursed globally because winds are strong and because aerosol residence times are long. The potential importance of large stratospheric aerosol loading on global climate has been known for quite some time. The most extreme example occurred after the eruption of Tambora in 1815, which is believed to have injected the largest amount of aerosol material in the stratosphere of any volcano in the historical record. The following summer (1816) has become known as the "year without a summer" in the USA and Western Europe, with snow in July, frost in all summer months, and total crop failures [Robosk, 2000].

Stocks et al. [1998] project a significant increase in the frequency and severity of boreal fires under a changing climate. In fact, there is speculation that climate change has contributed directly to the severe forest fire seasons across Russia and Canada in recent years, including an unprecedented 21 million hectares burned in Siberia in 2003. Projected climate change will result in longer fire seasons, and greater areas burned under drier conditions, resulting in greater fuel consumption and fire intensity

levels (both major contributors to convection column development) resulting in more extensive hemispheric transfer of boreal fire smoke. Larger areas burned will also result in a younger age-class structure in boreal forests and a net loss of carbon from the biosphere to the atmosphere, creating the possibility of a positive feedback loop between climate change, boreal fire activity, and perhaps pyroCb.

In the northern summer of 1998, many large fires burned in the boreal zone of Canada and Russia [Forster et al., 2001; Kasischke et al., 1999]. According to Fromm et al. [2000] a few of the Canadian fires were responsible for creating plumes of smoke that entered the lower stratosphere in July and August, and resided in detectible amounts well into October. The postulated mode of entry: a combination of intense (and extensive) crown-fire burning, and extreme convection in thunderstorms: pyroCb. At its greatest extent, the stratospheric smoke layers resided at 16 km (430 K potential temperature), a full 6 km above the tropopause [Fromm et al., 2005]. In late summer and early fall this stratospheric smoke cloud was seen to spread completely around the globe at middle and high latitudes. There were no reported volcanic eruptions in 1998 to explain such an extensive, deep intrusion.

The pyroconvection of 1998 was not an isolated event--in 2001 a similar phenomenon occurred. Detailed vertical profiles of aerosol extinction from the Naval Research Laboratory's Polar Ozone and Aerosol Measurement (POAM) III and NASA's Stratospheric Aerosol and Gas Experiment (SAGE) II and HALogen Occultation Experiment (HALOE), as well as an assortment of ground-based lidars in Europe, North America, the tropical Pacific, and the high Arctic recorded an extensive and enduring stratospheric aerosol enhancement [Fromm et al., 2008]. Once again, there was no reported volcanic eruption of sufficient magnitude to explain these observations. One of the remarkable revelations of this case was that the smoke cloud on the day immediately following the "eruption" was optically opaque to the nadir viewers at the tropopause level. This finding alone gives a compelling stimulus to take a new look at the power of extreme convection to

exacerbate combustion and smoke production, and then deposit copious amounts of boundary layer material deep into the atmosphere.

In addition to the extensive observations in 1998 and 2001, there is evidence of pyroCb leading to long-distance and/or stratospheric intrusion in other years as well. In 1992, a pyroCb in Idaho was found to be the origin of stratospheric measurements of methyl cyanide [Livesey et al., 2004], a gas emission known to be released by biomass burning. Waibel et al. [1999], using aircraft measurements over the United Kingdom, measured biomass burning emissions in the UTLS and speculated that fires in Canada were the source. During the Cirrus Regional Study of Tropical Anvils and Cirrus Layers – Florida Area Cirrus Experiment (CRYSTAL-FACE), several stratospheric in situ measurements of biomass-burning materials were traced back to pyroconvection in Canada in June 2002 [Jost et al., 2004]. Damoah et al. [2006] reported on and simulated transport from pyroconvection in Alaska in summer 2004 was the source of regional pollution in the lower stratosphere. As far back as 1950, a long-burning fire in western Canada was known to be the starting point for a smoke plume that darkened skies in the eastern USA and caused observations of blue suns and moons over Europe. In that case, aircraft observations of the plume were made over Scotland at an altitude of 11 km [Penndorf, 1953]. The literature contains multiple references to observations of mystery clouds in the stratosphere (i.e. in the absence of a known source such as a volcano). Perhaps an explanation of these puzzling observations is to be found in the above-mentioned recent discovery.

Some attempts have been made to model pyroconvection. Trentmann et al. [2006] and Luderer et al. [2006] used a high-resolution convection model to study the Chisholm pyroCb. Certain physical characteristics of the convective cloud top and outflow, e.g. penetration into the stratosphere, were successfully simulated. Moreover the simulation of Luderer et al. [2006] found that sensible heat release by the fire dominated the vertical penetration of the storm and that cloud dynamics were only weakly sensitive to cloud condensation nucleus abundance.

"Regular" (i.e. air mass or frontal) convection has been shown to inject material into the stratosphere. Poulida et al. [1996] showed highly resolved measurements in and above "regular" thunderstorm (i.e. unassociated with fire) anvils revealing irreversible transport of tropospheric gases above the local tropopause. Wang [2007] has used a convection cloud model to simulate regular deep convection and show features of water-ice plumes and related cloud phenomena above the storm anvil in the lowermost stratosphere.

The incomplete historical record of pyroCb and our limited knowledge of the generality of transport by regular convection into the stratosphere indicate that there is much more that needs to be learned about both processes. Moreover, the relationship between regular, pyro- and volcanic convection are almost totally unexplored. The revelation of pyroconvective influence on the stratosphere thus heightens the need to take a unified look at the process of atmospheric convection from an observational and theoretical perspective.

The discovery that boreal forest fire smoke can be injected into the stratosphere via intense thunderstorms is surprising, and has a large range of potential ramifications for key atmospheric science problems. Because the details and significance of this potentially important process remain largely unexplored, this Ph.D. research project undertakes some of these topics. Chapter 2 is an analysis of a pyroCb in the southern summer of 2002/2003. The major event was a pyroCb in Canberra on 18 January 2003 [Fromm et al., 2006]. The analysis covers both the pyroconvection and the stratospheric smoke spread. Chapter 3 is an investigation, exploiting nadir-viewing satellites, into the Chisholm pyroCb [Fromm and Servranckx, 2003] in Alberta Canada in May 2001. This is the first attempt to glean quantitative information on the amount of smoke aerosol injected into the stratosphere from a pyroCb. Chapter 4 presents the downstream impact of the Chisholm eruption from the viewpoint of space-based and ground-based aerosol profiles. Chapter 5 is an analysis of aerosol and temperature data to explore the radiative impact of lower stratospheric smoke plumes.

Chapter 2: The January 2003 Canberra pyroCb

2.1 Introduction

Headline-making firestorms in southeast Australia in 2003, responsible for at least 500 destroyed buildings and four lost lives, culminated with pyroCb eruptions that ravaged Canberra on 18 January. Here it is revealed that in their 3-hour lifetime, the Canberra pyroCbs also produced a stratospheric smoke injection that perturbed the hemispheric compositional and radiative background. We use an unprecedented array of sensors to analyze the Canberra pyroCbs' stratospheric injection, distinctive microphysics, energetics, and surface manifestations,—including suppressed precipitation, an F2 tornado, and black hail.

2.2 Bushfire Setup Conditions

Devastating fires over the Canberra and Snowy Mountains regions of southeastern Australia (see Figures 2.1, 2.2, and 2.4 for maps) started from lightning strikes on 8 January [Webb et al., 2004]. Prior to the fire season, the 2002/03 El Niño event had brought abnormally low rainfall and high temperatures to large parts of eastern Australia [Webb et al., 2004]. Between 8 and 17 January, the fires persisted as drought levels remained elevated in mild, anti-cyclonic weather conditions. On 18 January the passage of a low pressure trough brought strong, dry westerly winds across the area. Day-time heating caused mixing downward of the stronger upper level winds. Wind speeds of 13 m/s with gusts to 22 m/s were recorded shortly after 0420 UTC (1520 LT). High temperatures (maximum 37.4 ºC at Canberra airport, roughly 12 km from the fires) and low relative humidity (minimum 8%), combined with the very dry vegetation and the strong wind, produced extreme fire danger conditions [Webb et al., 2004]. The upper air sounding from Wagga Wagga, 163 km to the west (Figure 2.4a), suggests the regional atmosphere was potentially unstable despite dry air near the surface. In fact, thunderstorms did form on the ranges and the coast to the north of Canberra on the afternoon of 18 January. In this environment the Canberra pyroCb grew explosively (Figure 2.2a-d).

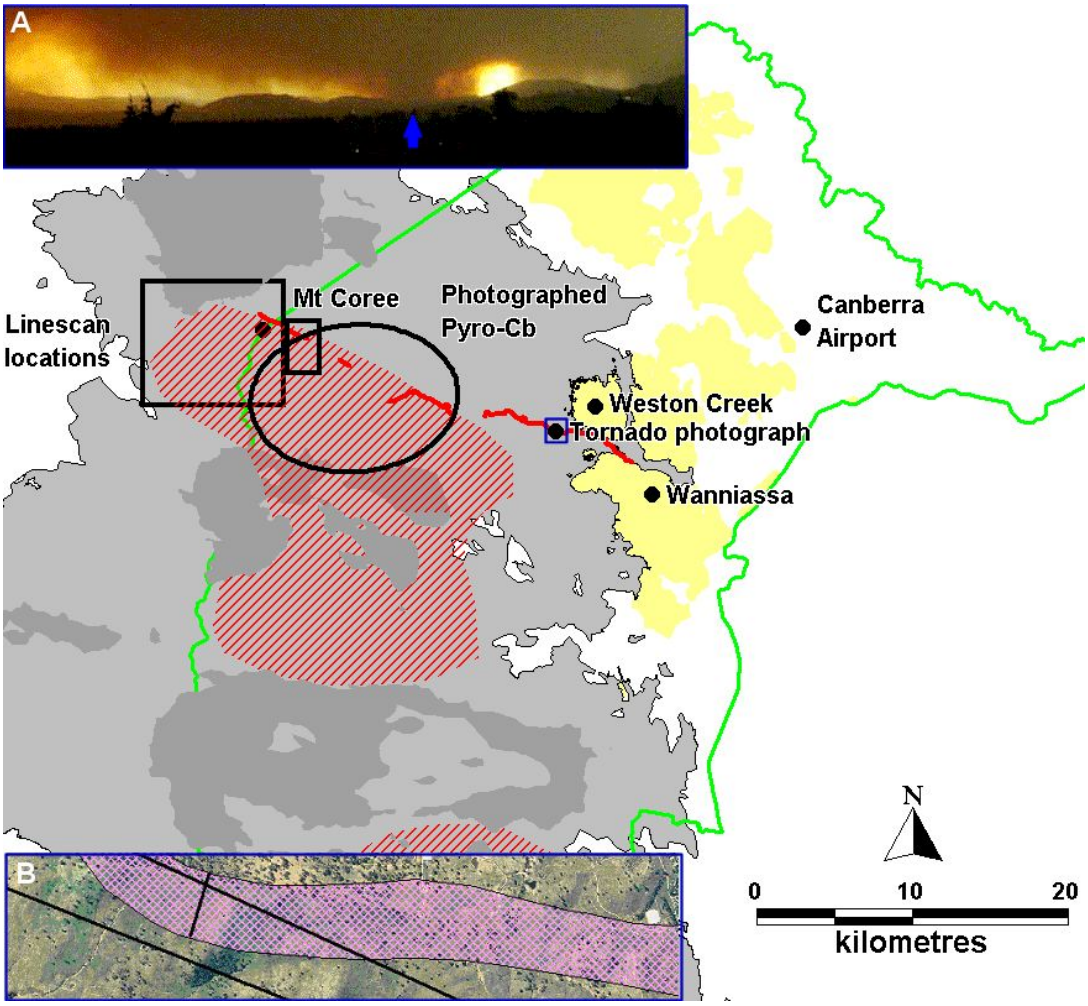

Figure 2.1: Locations and observed phenomena discussed in the text. Green outline--border of the ACT; yellow--urban area; light gray--final burnt area; dark gray--fire extent before 18 January 2003; red hatched--most intense convection at about 0400 UTC (1500 LT) 19 January (1500 18 January LT). Red line--mapped tornado damage trail. A) photograph from Wanniassa, at 0408 UTC (1508 LT), 18 January, looking WNW. Blue arrow points to apparent tornado. Photographer: Jim Venn. B) detail from photogrammetric reconstruction of tornado path. Hatched area is the damage zone; the black lines are sightlines from the photo. GIS-measured width of the damage zone (blue line) gives a 440m basal diameter.

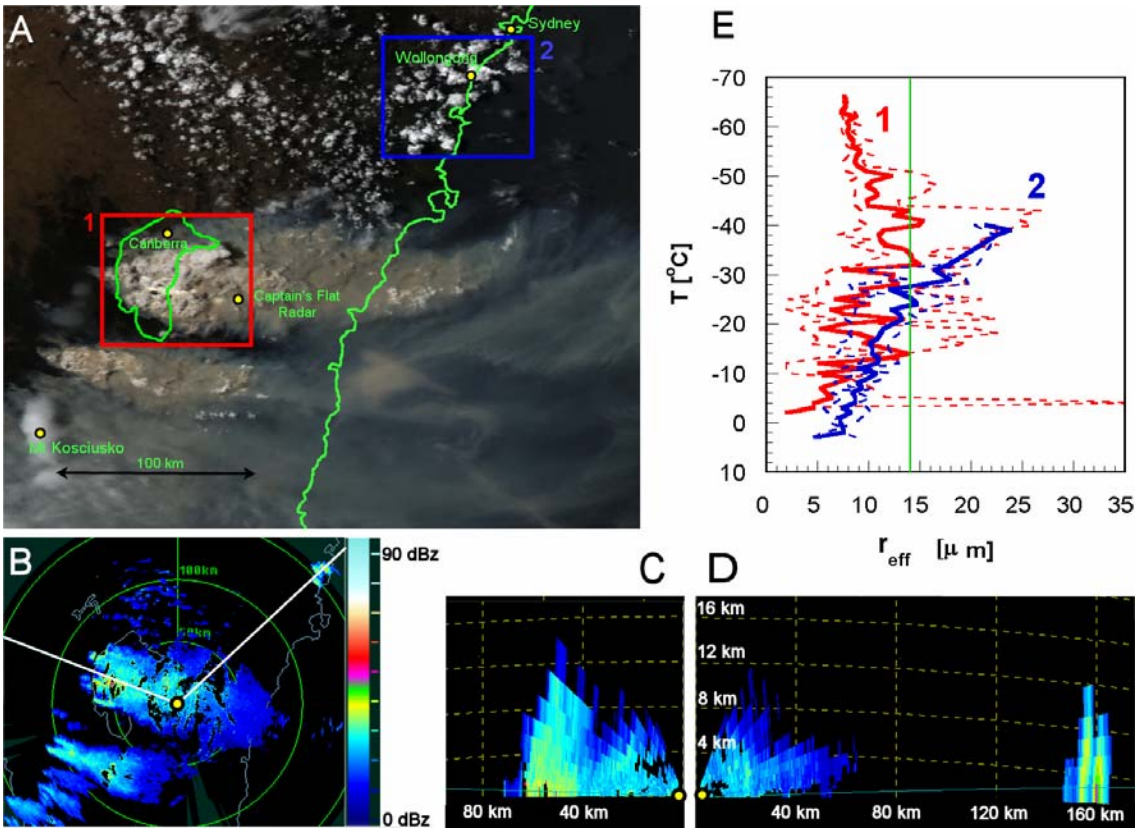

Figure 2.2 A) Aqua/MODIS true-color image, 0330 UTC, 18 January 2003, of smoke plumes, pyroconvection, and "regular" convection. Outline of ACT and NSW coast in green. B) Plan Position Indicator (PPI) view from Captain's flat radar at 0340 UTC. C) Range Height Indicator (RHI) view through pyroCb along WNW-ESE axis indicated in B. D) RHI view through SW-NE axis showing smoke (0-60 km) and developing Cb near Wollongong (160 km). E) Particle effective radius (r_{eff}) and cloud top temperature relations, using MODIS 0330 UTC data, for pyroCb area (red) and storms near Wollongong (blue). Shown are the 15% (dashed line), 50% (solid line) and 85% (dashed line) percentiles of the r_{eff} for each 1ºC interval. The vertical line at 14 μm represents the precipitation threshold [Rosenfeld and Gutman, 1994].

2.3 The 18 January PyroCb

During the peak flaming and fire spread in the afternoon of 18 January we use infrared linescans to estimate that the instantaneous flaming zone of the combined firefronts close to Canberra occupied 5000 ha, generating an energy release of 4.3×10^{13} kJ. In the peak 10 minutes of flaming at about 0410 UTC (1510 LT), 3.5×10^{12} kJ were released. This is equivalent to 22 kT of TNT, more than the Hiroshima atomic bomb (15 kT), and exceeds typical energy release in thunderstorm

cells by 1-2 orders of magnitude [Doswell, 1996]. The Australian Bureau of Meteorology (BOM) weather radar east of Canberra at Captains Flat captured the entire sequence of cloud development as well as the flying ash in the dry smoke plumes from the fires. The radar sequence shows four main complexes of pyroCb over the Australian Capital Territory (ACT) with smaller complexes developing over the Snowy Mountains further south. The life of the Canberra pyroCb complex was ~3 hours, with individual cells of diameter ~10 km developing near the fire fronts and collapsing as they were advected to the east in westerly winds. The echoes from within the pyroCb were surprisingly and persistently weak when contrasted with the vigor of the clouds. We find no obvious supercell characteristics in the radar sequence. The maximum height of the echoes observed on radar was ~15 km at 0450 UTC (1550 LT), a conservative estimate of the true cloud/plume height considering the radar particle-size resolution.

Effective particle radii have been calculated for the Canberra pyroCb cluster and a cell to the northeast (Figure 2.2a,e), using established 3.7μm-based reflectivity techniques [Rosenfeld and Gutman, 1994; Rosenfeld and Lensky, 1998]. Figure 2.2e shows that the cloud particle effective radii in the pyroCb over Canberra were grossly reduced. The cloud above the -40ºC isotherm was composed of ice particles with extremely small effective radius (consistent with the weak radar echoes), suggesting homogeneous freezing of most condensates while still in the form of small cloud droplets, which implies strongly inhibited precipitation-forming processes. The cloud to the northeast had cloud droplets exceeding the precipitation threshold of 14 μm at and above -28ºC, indicating greater precipitation potential. No precipitation was observed in or near Canberra apart from some "black hail" 30 km to the east, a manifestation of the strong updrafts and suppressed precipitation within the smoky pyroCb. The few precipitation particles that managed to form had a large supply of highly supercooled water to feed on, and only the large sooty hailstones could fall through the strong updrafts. The blackness of the hailstones shows that they were formed in the smoke plume that was the core of the pyroCb.

Eyewitnesses reported multiple vortices in the pyroCb. Figure 2.3 shows quasi-simultaneous observations near the developing pyroCb, close to the origin of the tornado damage path in Figure 2.1, near Mount Coree. Views include a photograph of a possible tornadic vortex (and antecedent tree damage), IR linescan hot spot, a photograph of active and mature pyroconvection, and a radar echo-top map. Damage consistent with an F2 [Fujita, 1971] tornado occurred near Weston Creek (Figure 2.1). Three aspects of the damage path indicate a tornado rather than fire-induced whirls or roll vortices: 1. the path dimensions--20 km long, up to 450 m across; 2. breaks in the damage path (consistent with the vortex temporarily lifting); and 3. damage extent well beyond the burn zone. Moreover, the vortex observations occurred close in time and space to the most rapid cell growth and pyroCb maturity. For example, the photograph in Figure 2.1, aligned with the damage path, near pyroCb maturity, indicates a possible funnel cloud. The observed cells and vortices are most consistent with relatively intense forms of non-supercell tornadoes [Wakimoto and Wilson, 1989], fire-induced vortices stretched by updrafts from rapidly growing pyroCb cells, forming F2-strength tornadoes.

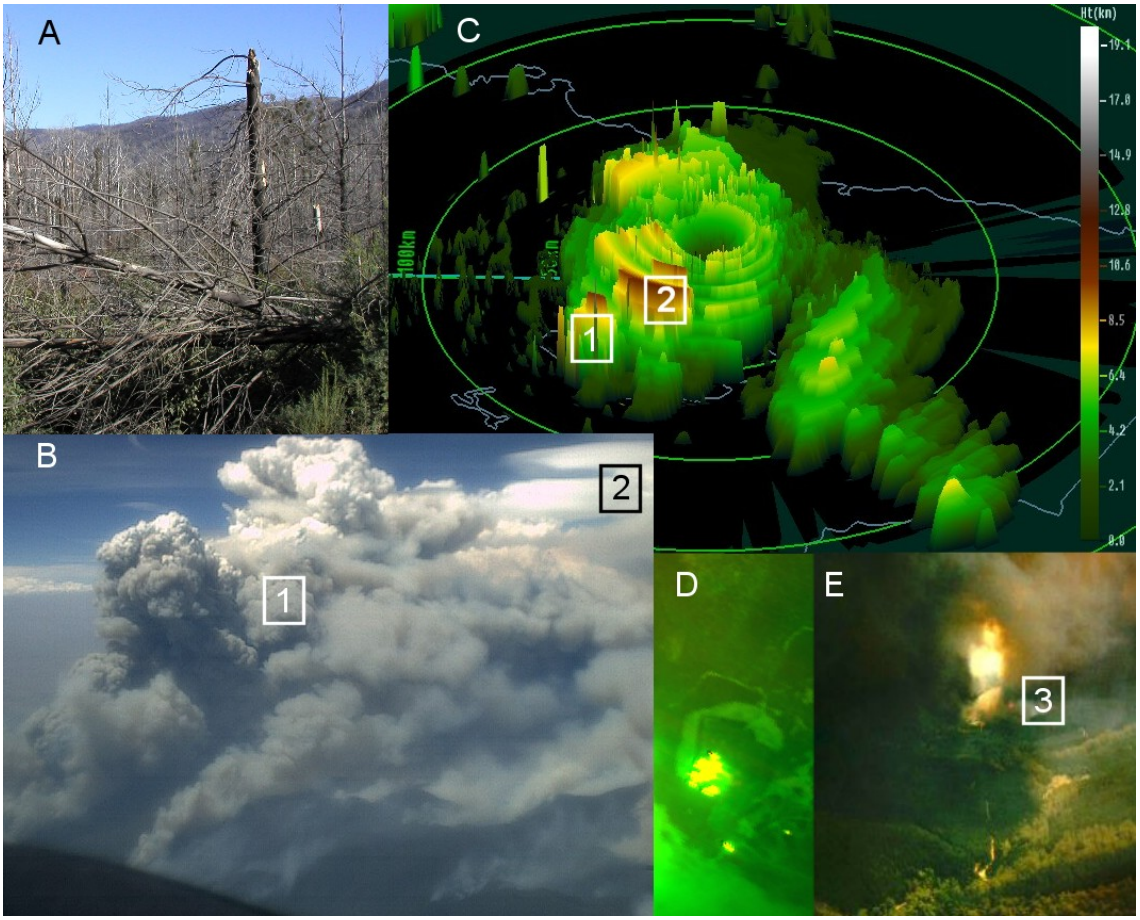

Figure 2.3. A) Damage in pine trees east of Mount Coree on NW border of ACT, showing trunks snapped ~3m above ground and fine branches stripped off limbs (image taken 0200UTC, 31 May 2005). B) Aircraft photo looking eastward, of pyroCb growing above location of panel A at 0404UTC, 18 January 2003 (‘1’), and mature pyroCb tops in distance (‘2’). C) 3D view of 1 dBz radar contour at 0410UTC, looking eastward to show the pyroCb complexes ‘1’ and ‘2’ identified in panel B. D) Fire linescan above location of ‘A’, showing spot-fire in clearing at ~0412UTC. E) Apparent tornadic vortex (‘3’) to right of spot fire in panel D at 0408UTC. The damage shown in panel A occurred in the , presumably after the photo was taken.

Taken together, the observations of weak echoes, small effective radii, black hail, and tornadic vortices are all consistent with fire-enhanced deep convection having suppressed particle aggregation and precipitation processes [Andreae et al., 2004; Rosenfeld, 2000], which inhibits the formation of strong downdrafts and hence the efficient removal of the smoke from the atmosphere. As we shall see next, the

resultant violent updrafts penetrated the tropopause and injected smoke into the stratosphere.

2.4 Stratospheric Impact

The first indication of the Canberra pyroCb's potential climate impact came from satellites. Aerosol Index (AI) data from NASA's Total Ozone Mapping Spectrometer (TOMS), which has been successfully employed to identify large-scale stratospheric smoke transport [Fromm et al., 2005; Jost et al., 2004; Livesey et al., 2004], detected several extreme smoke outbreaks from southeastern Australia between 18 January and 1 February. The 18 January pyroCb ejecta were detected on 19 January (Figure 2.4a), when several distinctly brown clouds over the Tasman Sea were captured in Moderate Resolution Imaging Spectroradiometer (MODIS) true-color imagery. The 19 January AI map (Figure 2.4b), within one hour of MODIS, reveals a super-intense node of smoke aerosols at 32˚S, 162˚E. AI is a strong function of plume altitude [Fromm et al., 2005 and references therein] -values of this extreme have only been observed on one other occasion in the 25-year TOMS era, after the Chisholm pyroCb [Fromm and Servranckx, 2003]. We constrain the effective altitude of the plume with isentropic back trajectories, calculated on a dense vertical grid, all beginning at the TOMS measurement time and ending at 0330 UTC 18 January, when the Canberra pyroCb was active. The best temporal-spatial match was found at the 385K potential temperature surface, in the stratospheric overworld.

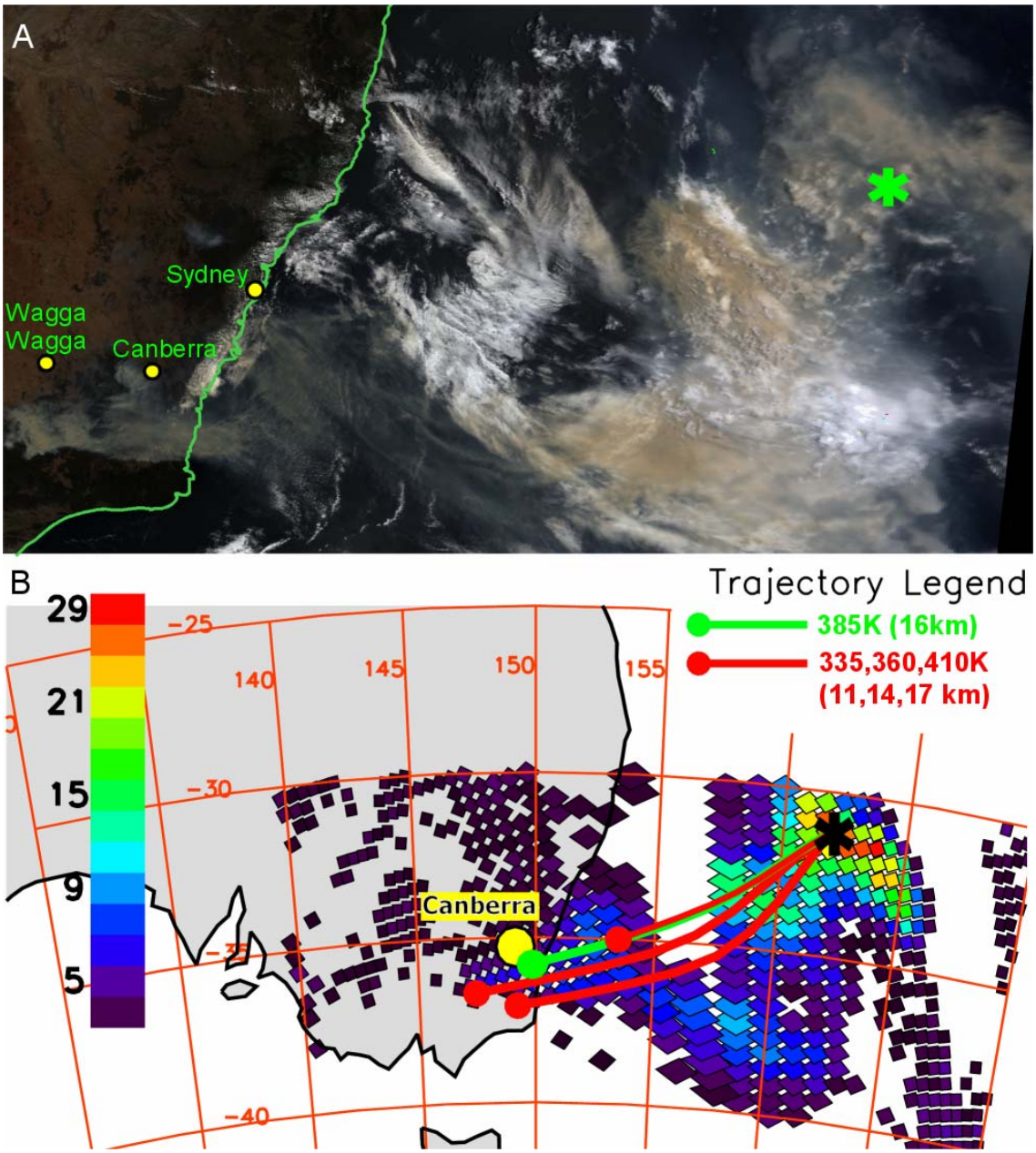

Figure 2.4. A) Terra/MODIS true color image of southeast Australia, 0000 UTC, 19 January 2003. B) TOMS AI image for the same time. Backward isentropic trajectories,using analyses from the Met Office, from the location of extreme AI (denoted by an asterisk on both images) for potential temperatures 300K to 440K at 5K intervals. The trajectory start time is the TOMS observation time, ~0100 UTC 19 January. The 385K back-trajectory is a close (and the best) match for smoke from the Canberra fires, 20 hours previously. Other selected trajectories, from above and below the optimal match, are in red.

Within one week of 18 January, stratospheric aerosol-layer detections were recorded by NASA's Stratospheric Aerosol and Gas Experiment (SAGE) III instrument. The enhancements in SAGE III aerosol extinction profiles increased in frequency after 18 January and became a hemispheric feature within one month. Daily mean and median aerosol extinction at 385 K are shown in Figure 2.5, along with median extinction at 435 K (above the injection altitude). Figure 2.5 shows three periods. The pre-blowup quiescence—relatively low levels of aerosol extinction—is evident in early January. The post-blowup regional stratospheric impact (25 January -14 February) is manifested by the early increases in zonal mean and latter rise in the median. The full hemispheric pollution and decay period (14 February on) is characterized by the meeting of the mean and median, and the gradual decrease through March. At its peak hemispheric impact, the zonal median 385K aerosol loading was nearly 2.5 times the pre-injection level.

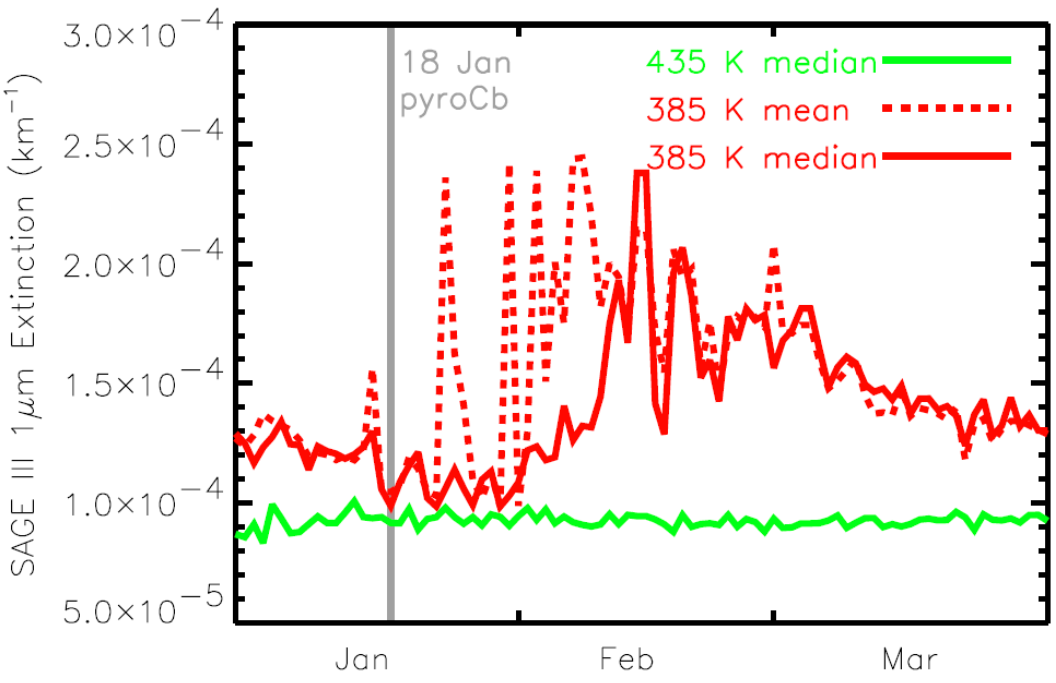

Figure 2.5. Daily mean and median SAGE III 1020 nm extinction at 2 isentropic levels. SAGE III made 14 profile measurements equally spaced longitudinally each day, at latitudes between 34˚ and 46˚S, between January and March 2003.

2.5 Summary

This is the first major pyroCb event detected and analyzed for the Southern Hemisphere. Three aspects of this remarkable phenomenon require increased understanding. First, the tornadic and fire-induced destruction underneath the Canberra pyroCb indicates the necessity of developing appropriate forecasting/warning techniques. Second, the pyroCb appears to be a unique storm, combining elements of "normal" (i.e. instability-related) convection with explosive heat-energy release at the ground. The heat-aided convection produces a plume akin to certain volcanic eruptions. Indeed, the grossly suppressed cloud-top particle sizes in the convection are quite similar to the 1991 Mt. Pinatubo eruption clouds [Tupper et al., 2005]. Lastly, it appears that the brief (~3 hrs) and microscale (~10 km diameter) pyroCb has now been shown to have the explosive capacity to pollute the austral stratosphere with absorbing aerosols that intercept solar radiation--with significant implications for weather and climate [Fromm et al., 2004].

Chapter 3: Stratospheric impact of the Chisholm PyroCb: earth-viewing satellite perspective

3.1 Introduction

The pyrocumulonimbus storm near Chisholm, Alberta on 28 May 2001 has been studied in depth. However the impact of this eruption on the lower stratosphere has not been characterized. Here and in chapter 4 we explore this topic. This chapter focuses on the "young" Chisholm smoke plume, from the age of ~3 hr to 1 week, as observed by earth-viewing satellite instruments. (The next chapter presents strictly profile data.) Geostationary Operational Environmental Sateliite (GOES) visible and infrared image loops reveal the pyroconvective lifecycle and initial transport of the smoke cloud. Multi-angle Imaging Spectroradiomenter (MISR) stereographic heights are the first of their kind for a stratospheric cloud, showing smoke up to 5 km above the tropopause on 29 May. MODIS IR and visible images are analyzed to give constraints on plume height, thickness, and particle size. Infrared brightness temperature (BT) analyses reveal unique aspects of the "day after" Chisholm plume. Particle sizes are 1/3 to 1/2 compared to normal cirrus crystals. The daytime 29 May plume is optically thick at tropopause temperatures yet smoky brown. A transition from deep anvil blow off to "dry" smoke is still occurring after ~1.5 days. TOMS AI is used as a proxy for areas of particularly high smoke-plume altitude. The Chisholm smoke in the upper troposphere and lower stratosphere (UTLS) is traced with AI for one week as the plume blows across North America to western Europe. First estimates are made of stratospheric smoke-mass in relation to emissions during pyroconvection. The 29 May stratospheric Chisholm pyroCb plume contains a mass between ~1.39×10^4 and 1.09×10^5t. This represents between ~10% and 121% of total particle mass emitted from the fire on 28 May, calling into question some frequently assumed values for smoke single scatter albedo and/or emission estimates. Strictly in terms of mass, the stratospheric Chisholm plume amounted to ~15% of background northern hemispheric stratospheric sulfate aerosol. Overall the young pyroCb plume is seen to be a peculiar mixture of smoke aerosols and water-ice that confounds

operational cloud/aerosol detection routines and exhibits extreme—and still mysterious—composition and lifecycle features.

In section 3.2 we describe the data sets used. Section 3.3 contains an analysis of the "day after" Chisholm plume as observed by GOES, TOMS, MODIS, and MISR. In Section 3.4 we compare MODIS and TOMS views of the Chisholm plume on 30 May 2001 with the 29 May "day after" plume. Section 3.5 contains the analysis of the movement of the plume in its first week revealed by TOMS AI maps. Discussion and summary are contained in Section 3.6.

3.2 Data Sets

3.2.1 MISR

MISR provides continuous multi-angle imagery of the sunlit Earth. The instrument contains nine charge-coupled-device-based pushbroom cameras to observe the Earth at nine discrete view angles: One view points toward nadir, and the other eight are symmetrical views at 26º, 46º, 60º, and 70° forward and backward of nadir. Images at each angle are obtained in four spectral bands centered at 446, 558, 672, and 866 nm. The swath width of the MISR imaging data is 400 km. It takes 7 minutes for any particular scene to be observed at all nine viewing angles. In its global observing mode, data from the red band of all of MISR's off-nadir cameras, and in the four bands of the nadir camera, are acquired at 275-m spatial resolution; all other channels are averaged on-board to 1.1-km resolution to conserve data rate. See Diner et al. [1998] for more details.

Ground data processing maps MISR radiances to a Space Oblique Mercator projection, which geolocates and co-registers the data from all instrument channels to both the WGS84 (World Geodetic System earth reference frame revised in 1984) ellipsoid and to the surface terrain altitude. Geolocation uncertainty is estimated to be ±50 m, and co-registration errors are < 1 pixel (275 m). Ongoing assessments of

image geolocation and co-registration are performed to ensure product quality [Jovanovic et al., 2002, 2007]. The high resolution, ellipsoid-projected red-band radiances are operationally used in an automated algorithm to derive cloud-top and aerosol plume-top heights relative to the surface. Pattern matching is used to determine the geometric parallax (horizontal displacement) for elevated atmospheric features, and stereo-photogrammetric algorithms transform these parallaxes into cloud-top or plume-top heights [Moroney et al. 2002; Muller et al. 2002; Zong et al. 2002]. In the standard MISR Level 2 Stereo Product, which uses the nadir and 26º cameras in the height retrievals, the quantized precision of the resulting height field is ±560 m. Altitudes for clouds as well as smoke and dust plumes are routinely retrieved and reported on a 1.1-km resolution geolocated grid. Because the heights are derived geometrically, they are insensitive to atmospheric temperature profile, emissivity, and absolute radiometric calibration uncertainties. Validation using ground-based 35/94 GHz radar and lidar retrievals of single-layer clouds shows instantaneous accuracies typically in the 500 m – 1 km range [Naud et al., 2002, 2004, 2005a,b; Marchand et al., 2007]. Since the technique is purely geometric, comparable accuracy is expected for aerosol layers.

Owing to the 7-minute interval from when MISR first sees a scene with the forward 70º camera to its last view with the backward 70º camera, the motion of clouds or aerosols during this time contributes to the disparity between image pairs and therefore must be distinguished from the parallax due to height. Consequently, a "wind correction" should in general be applied to the derived stereoscopic heights. This can be derived from a triplet of views (nadir, 46º, and 70º) [Horváth, and Davies, 2001; Zong et al., 2002]. Only the along-track component of motion contributes to the uncorrected parallax error. The magnitudes of wind corrections are typically < 1 km in height. Given the better density of coverage typically obtained with the non-wind-corrected heights, and the generally small height error associated with winds, it is often more convenient to ignore the wind corrections when the resulting uncertainty is tolerable.

Many aerosol plumes are too tenuous to be reliably detected in the nadir and 26º views which are used in MISR's operational height retrievals. However, the MISR 60º and 70º views are much more sensitive to thin plumes due to the oblique slant path. Specialized runs of the MISR stereo retrieval algorithm demonstrate that it works well with the oblique cameras and improves the height coverage for thin clouds, elevated aerosol layers, and near-surface plumes that the operational product currently misses.

3.2.2 TOMS Aerosol Index

The TOMS sensor detects UV absorbing aerosols with the well known AI parameter [Herman et al, 1997]. The AI is a measure of the spectral contrast change in the UV (331 and 360 nm) resulting from the presence in the atmosphere of light absorbing particles. Thus, the AI is primarily a measure of the 'missing' Rayleigh-scattered (and cloud-reflected) radiation at the top of the atmosphere that has been absorbed by the aerosols. The AI magnitude depends strongly on the aerosol layer height above the ground and its optical depth [Torres et al., 1998]. The sensitivity of AI to aerosol layer height can be advantageously used for the unambiguous detection of UTLS absorbing aerosol layers generated by pyro-convection. These highly elevated aerosol layers yield unusually high AI values (10 or larger) clearly associated with their UTLS location. Aerosol Index values for large tropospheric aerosol loads associated with biomass burning or desert dust aerosols are typically no larger than about 8. The ability to detect UTLS absorbing aerosols is a clear improvement of the TOMS version 8 data [Bhartia, 2007]. In version 7 the AI data was artificially truncated at a value of 12.8. By removing this arbitrary limit the TOMS aerosol data has become a very useful tool for the detection and tracking of pyro-convection activity [e.g. Fromm et al., 2005].

3.2.3 MODIS

We use Terra MODIS collection 5 level 1b data [Yang et al. 2007 and references therein]. Our analysis uses 1 km resolution data from visible channels 1 (0.645μm), 3 (0.469 μm), and 4 (0.555 μm) for true-color imagery and radiance data from the thermal infrared (THIR) channels 31 and 32 (11 and 12 μm), expressed as brightness temperature. In addition to the leve1b data, we also exploit MODIS level 2 aerosol [Remer et al., 2005] and cloud [King et al.,1992 and 2003] products.

3.3.0 The Chisholm "day after" Smoke Plume: 29 May 2001

The Chisholm fire erupted into pyroconvection in the late afternoon on 28 May 2001, at approximately 00 UTC 29 May [Fromm and Servranckx, 2003]. The active convection persisted for about three hours and created an opaque smoke/ice anvil with 11 μm brightness temperatures lower than -60°C, ~2°C lower than the tropopause temperature [Rosenfeld et al., 2007]. After 03 UTC the pyroconvection ceased and the residual plume, spanning the tropopause into the lowermost stratosphere, moved north toward the Northwest Territories (NT).

The evolution from pre-pyroCb to residual plume was captured with a day-long animation of GOES imagery, for the period 22 UTC 28 May to 2345 UTC 29 May (see http://rammb.cira.colostate.edu/projects/pyrocu/28may01/visloop.asp http://rammb.cira.colostate.edu/projects/pyrocu/28may01/ch4loop.asp http://rammb.cira.colostate.edu/projects/pyrocu/28may01/ch2loop.asp). The visible frames contain 3.9 μm hot-spot pixels. The animation shows the apparently expanding/heating Chisholm fire, the pyroCb pulsing in two main phases, and the expansive cold/opaque cloud persisting through the night. The THIR animation is summarized by a time series in Figure 3.1, which shows the transformation of the peculiarly and persistently cold Chisholm plume. After cessation of pyroconvection the plume continued to emit at BT < -60°C for ~13 hours, well after sunrise 29 May. Surrounding radiosonde observations at 12 UTC all record temperature minima

greater than that of the plume-top. Moreover, the area with BT < -60°C expanded throughout the night and into daylight, to roughly 46000 km^2 8 hours after pyroconvection. THIR cooling in time of an individual tropospheric cloud would normally be interpreted as a thickening and/or rising thick cloud. We do not have a satisfactory explanation for this cooling of a post-convection cloud top. However we have observed it in other pyroCb cases (not shown), yet not for "regular" convection.

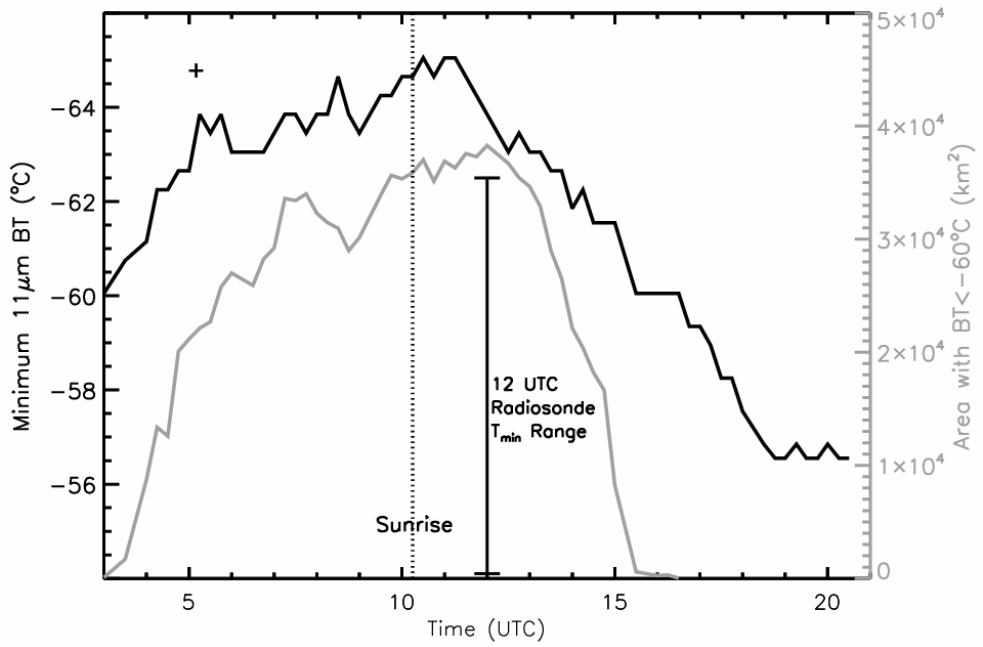

Figure 3.1. Timeline of GOES 11μm BT minimum (black) and pixel area (gray) for pixels with BT < -60ºC following the Chisholm smoke plume between 3 and 21 UTC 29 May 2001. Vertical bar gives range of 12 UTC radiosonde T_{min} for four closest and surrounding launch sites: Fort Smith (60ºN, 112ºW), Fort Nelson (59ºN, 123ºW), Norman Wells, (65ºN, 127ºW), and Cambridge Bay (69ºN, 105ºW). Sunrise time at vertical dotted line. MODIS 0510 UTC BT minimum, plus symbol.

After sunrise on 29 May the plume is a large, smooth gray cloud that spreads and arcs through NT and then southeastward toward Hudson Bay. Next we will analyze the post-pyroCb plume with polar-orbiting satellite views at two times during this "day after."

3.3.1 Nighttime MODIS View

Here we introduce MODIS THIR image data to gain insights into the Chisholm plume's height, opacity, and plume-particle size. The wealth of IR channels provided by MODIS is quite valuable; here we focus on two THIR wavelengths (11 and 12 μm) that have been successfully used on clouds and volcanic plumes, and which are common among the operational geostationary and polar orbiting imagers. We use a THIR BT-difference technique that gives information on cloud-particle physical properties in darkness and daylight.

The 29 May Terra MODIS nighttime IR imagery (0510 UTC, 2210 LST) captures the young plume about 3 hours after pyroconvection collapsed. Figure 3.2a gives the THIR BT. The Chisholm plume has a substantial area colder than -60°C. As Rosenfeld et al., [2007] reported, this represents an optically opaque surface above the local tropopause. It is obvious from the low BT that the young Chisholm pyroCb plume is distinctive from all the other clouds in this scene, even though deep nonpyro-convection occurred the prior evening [Rosenfeld et al., 2007]. Note that the MODIS 0510 UTC BT minimum is even lower than the GOES value at that time (shown in Figure 3.1).

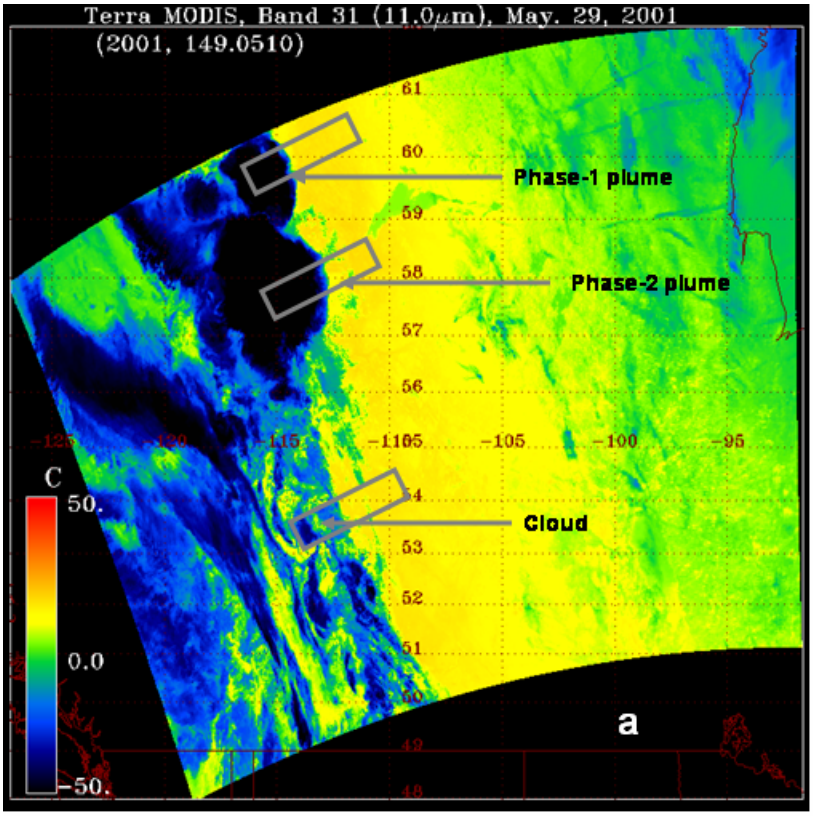
Terra MODIS, Band 31 (11.0μm), May. 29, 2001
(2001, 149.0510)
Phase-1 plume
Phase-2 plume
Cloud
C
50.
0.0
-50.
a

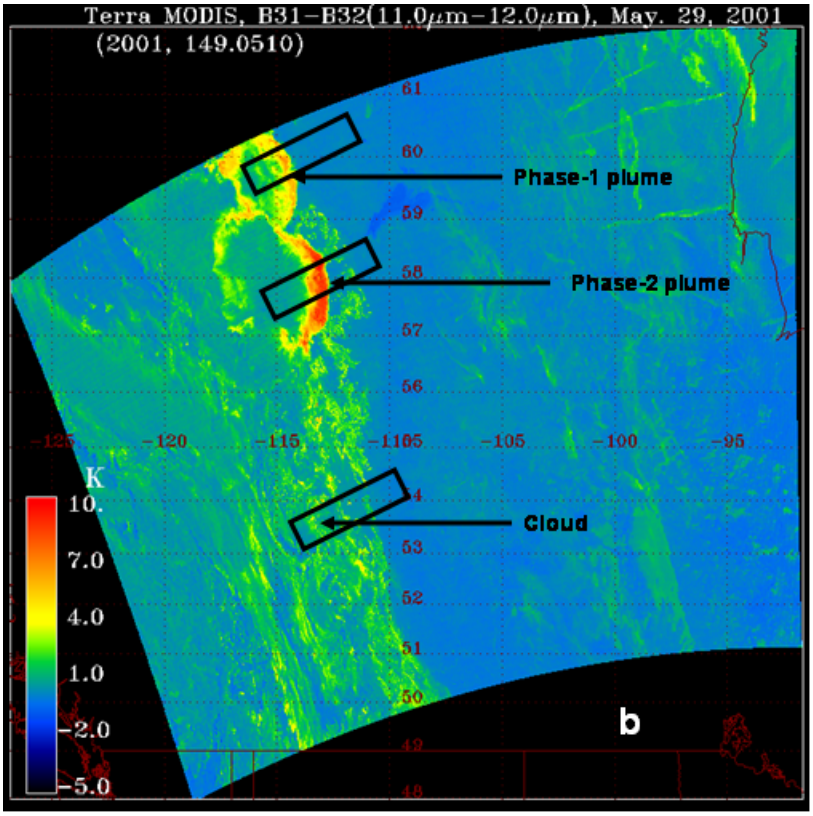

Figure 3.2. Terra MODIS IR nighttime brightness temperature (BT) imagery at 0510 UTC 29 May 2001. (a) 11 μm BT. (b) 11-12 μm brightness temperature difference (BTD). Boxes show scenes for which a BTD analysis is performed.

3.3.1.1 THIR Brightness Temperature Difference

Figure 3.2b contains a brightness-temperature difference (BTD) image. BTD is defined as 11 μm BT minus 12 μm BT. This so-called "split-window" technique has been used to evaluate volcanic cloud composition [e.g. Wen and Rose, 1994] and meteorological cloud-particle size [Gothe and Grassl, 1993]. Split-window BTD is expected to be zero to slightly positive (i.e. generally < +1.0 K) for optically thick water-ice clouds. However, for high-altitude optically thin meteorological or volcanic cloud, BTD departs considerably from zero. Thin water-ice clouds over a warmer surface typically give a positive BTD [Yamanouchi et al., 1987]; ash-rich optically thin volcanic clouds may have the reverse effect, leading to negative BTD

[Prata, 1989]. BTD has been used effectively as a detection method for yet another peculiar cloud form, the ice-rich high-tropospheric volcanic plume [e.g. Rose et al., 1995 and 2003]. The implication in such cases is that large positive BTD signifies anomalously small ice crystals populating a plume dominated by ice and ice-coated ash. In the present case of the 0510 UTC Chisholm pyroCb blowoff, BTD is near zero in the innermost portions of both residual anvils (where THIR BT is quite cold), and strongly positive on the perimeter, especially the eastward side. In this zone the cloud edge overlies cloudless skies (note the adjacent "warm" THIR BT in Figure 3.2a). The BTD here approaches +10°C, much larger than anywhere else in the MODIS scene.

According to the radiative transfer modeling framework in Figure 4a of Guo et al. [2004], BTD in this range is reserved for a population of cloud particles with exceptionally small effective radius compared to typical cirrus ice crystals. Prata and Barton [1993] used both a radiative transfer model and satellite THIR observations to demonstrate the relation of BTD to 11μm BT for a range of cloud optical depth and ice crystal effective radius. Figure 6 therein shows that BTD is near zero for clear sky (warm THIR) and optically thick, cold ice clouds, and increasingly positive in between. The positive departure from zero at a given optical depth or BT increases with decreasing particle size. Maximum BTD for cirrus cloud with nominal effective radius (~30 μm) is ~+3K in simulation and observation (their Figure 14).

We replicate that type of analysis with the 0510 UTC MODIS data in Figure 3.3, BTD as a function of 11μm BT. Three color-coded samples were taken from separate scenes (shown in Figure 3.2) sampling Phase I and II Chisholm plume segments and meteorological cloud. Each scene spans between cloud core and clear air to the east. Also in Figure 3.3 are curves from a radiative transfer model assuming spherical ice particles [Prata and Grant, 2001], showing BTD vs. BT for three values of effective radius. Like the simulation and observations of Prata and Barton [1993], the BTD at the warm (clear-air) and cold (optically thick cloud) extremes of each scene cluster near BTD=0ºC. The otherwise most obvious feature in Figure 3.3 is the

arcing BTD in between these limits for the Phase I and II plume segments, reaching a maximum of roughly +6ºC and +9ºC, respectively. These arcs conform well to theoretical arcs for ice particles of 16 and 12µm, respectively. The plume arcs are distinctive in comparison to the BTD pattern for the meteorological cloud, the core of which is cold enough (< -40ºC) to indicate ice. The conforming theoretical effective radius for the cloud/plume pixels at BT=-40ºC suggests that the plume segments are distinctive from one another (in terms of effective radius), yet both are distinctive from a nearby cold meteorological cloud. In this first application of the BTD vs. BT analysis to a smoke plume we make no claim in terms of absolute value of the particle effective radius, but rather conclude that such a young, deep, optically thick smoke plume is characterized by particles smaller by a factor of 2-3 compared to average meteorological-cloud ice. Interestingly though, the 0510 UTC plume-top effective radius (~10-15µm) is quite similar to the retrieved effective radius for the Chisholm pyroCb reported by Rosenfeld et al., [2007].

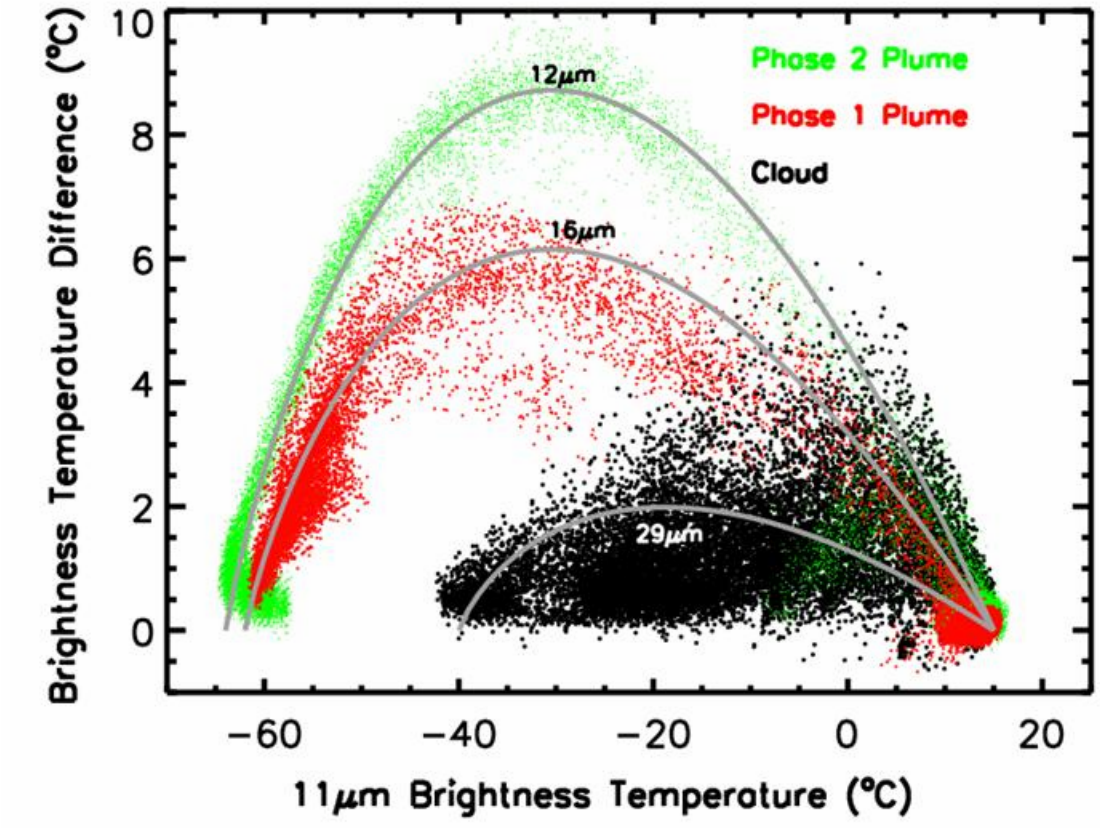

Figure 3.3. MODIS split-window BTD analysis, 0510 29 May 2001. Independent variable is 11µm BT (°C); dependent variable is 11-12µm BTD. Target scenes are color coded and labeled on the figure. Gray lines are theoretical curves from a radiative transfer model (see text for details) for ice-cloud particles of the labeled effective radius.

3.3.2 Daytime 29 May Views

3.3.2.1 MODIS Visible

Daytime (1840 UTC; 1140 LST) 29 May Terra MODIS views of the "day after" Chisholm plume are shown in Figure 3.4. A stretched true-color rendering in Figure 3.4a illustrates the breadth and abundance of smoke. Along the west, north, and east perimeter the smoke overlies pure white water ice cloud, with weak yet discernable shadowing suggesting higher smoke altitude. To the south a tongue of smoke is translucent over cloud-free sky. The perimeter smoke is relatively gray and smooth, and becomes dark brown and textured toward the core.

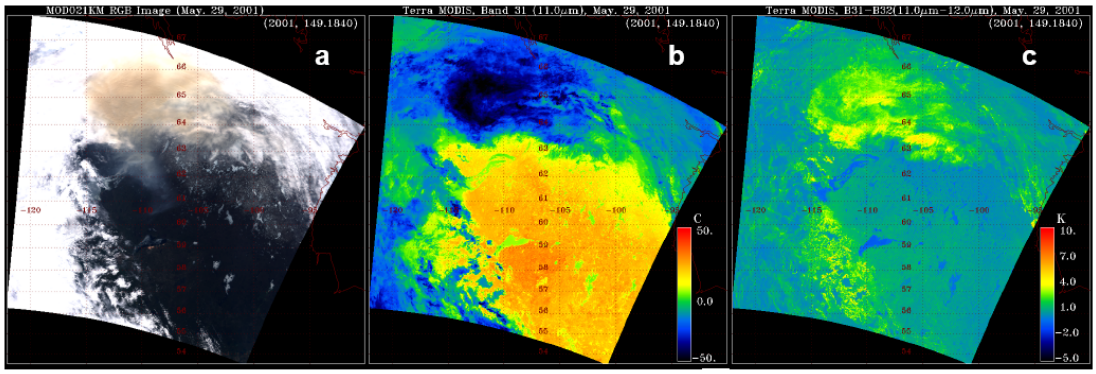

Figure 3.4. MODIS daytime true-color and infrared imagery at 1840 UTC 29 May 2001. (a) stretched true color. (b) 11µm BT. (c) 11-12µm BTD.

3.3.2.2 MODIS THIR

Figure 3.4b shows the THIR image. Much of the smoke plume core is opaque at BT < -40°C, which is a proxy for upper tropospheric altitude and represents a condition assuring homogeneous freezing [Wallace and Hobbs, 1977]. Thus any conventional cloud particles inside this contour would be in the form of ice. We see by comparison with the nighttime view in Figure 3.2a that the general cloud-top BT has increased but is still quite low within the smoke plume —and lower than

anywhere else in the image. Considering the spatial correspondence of low BT and smoky color—and the likelihood that this correspondence also applied during the overnight observation—we conclude from this plume-top "warming" that an evolutionary drying out of the smoke plume is taking place. Smoke-polluted ice is sublimating, thereby transitioning to smaller crystals and "dry" smoke. The Chisholm plume's BT is still distinctively low compared with other clouds in this scene, and that there is no clear evidence of other convective blow off from the prior evening's "regular" convection. Hence the smoke-ice pyroCb plume appears to be a particularly persistent form of anvil blow off compared with "regular" Cb blow off.

3.3.2.3 Daytime Brightness temperature Difference

The BTD at 1840 UTC is shown in Figure 3.4c. Here again the Chisholm plume has a distinctive signature—generally large BTD—albeit transformed from the nighttime view ½ day earlier. Here the area with the generally smoky color (Figure 3.4a) is notably positive in BTD, however the maximum BTD is depressed in comparison to the nighttime view.

A BTD versus BT analysis like that of section 3.1.1 and supplemental data are shown in Figures 3.5 and 3.6. Figure 3.5 gives the true color and THIR images with boxes showing where the BTD analysis is performed. We chose an exclusively meteorological cloud subscene (A), the plume and surrounding cloudy/clear area (B), and the core of the cold smoke plume (C). The BTD for A (Figure 3.6) is uniformly close to zero, from clear-sky through thick/cold cloud BT. For guidance and comparison, the vertical bar at BT~-40°C is placed to isolate the coldest cloud tops. The plume BTD not as large as at 0510 UTC. However it is positively offset from BTD=0 compared to the meteorological clouds at BT < -40°C, even in the inner core (i.e. optically thickest section) of the plume.

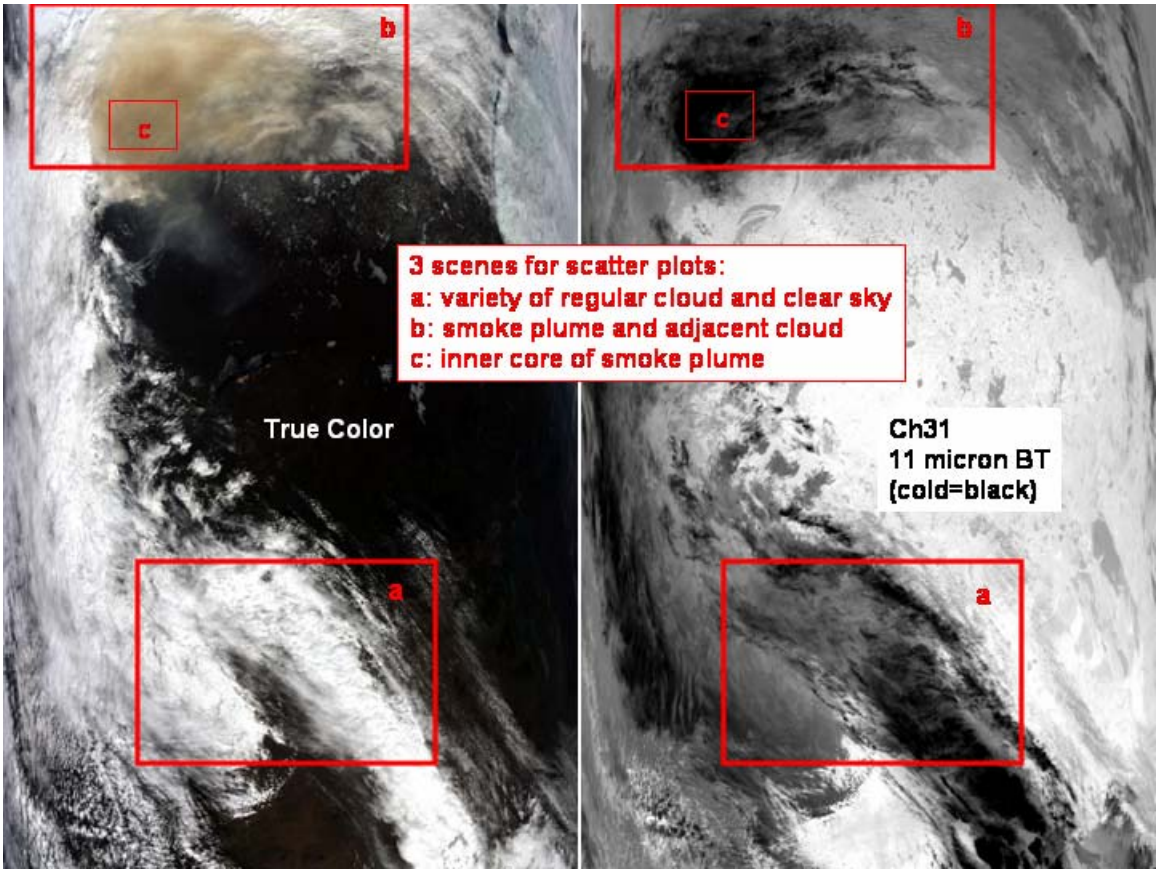

Figure 3.5. MODIS true color and 11μm BT at 1840 UTC 29 May, with boxes discriminating 3 scenes for split-window BTD analysis. Scene (a) contains only meteorological cloud. Scene (b) contains the smoke plume and surrounding meteorological cloud. Scene (c) is restricted to the smoky core of the plume.

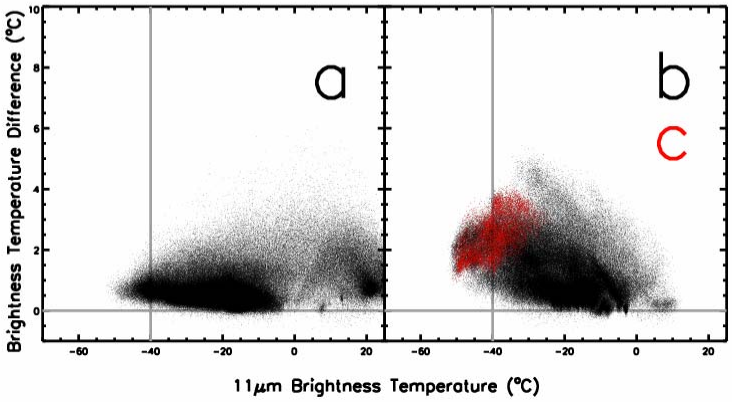

Figure 3.6. BTD analysis for 1840 UTC 29 May. Abscissa and ordinate ranges are identical to 0510 UTC analysis in Figure 3.2. Panel (a) is for scene a of Figure 3.4. Panel (b) has both scenes b (black dots) and c (red dots).

To our knowledge this peculiar condition is not documented in the literature. The BTD signature at 1840 UTC indicates that the plume-top composition and/or prevailing particle size is unique, a conclusion reinforced by the strong smoky coloration. Thus it appears that deep, optically thick "day after" pyroCb plumes can create a uniquely positive BTD signature in sunlit conditions. It would be valuable in future work to study other similar plumes from both an observational and radiative transfer modeling standpoint.

3.3.2.4 MODIS Aerosol and Cloud Product

The GOES and MODIS visible and IR data shown so far have revealed several strong peculiarities in the Chisholm smoke plume, both with respect to "normal" smoke and meteorological cloud. That impression is reinforced in the MODIS level 2 aerosol and cloud products for the 1840 UTC 29 May scene. Figure 3.7a gives a composite of true-color with aerosol optical depth (AOD); Figure 3.7b shows cloud-top pressure (CTP) with AOD. The true-color/AOD composite reveals

that the MODIS aerosol retrieval delivered results only for the fringe of the plume around what is labeled “dry” smoke (a characterization based on the transparency of the plume there in the THIR (see Figure 3.4b), and its apparent extension beyond the large water-ice cloud deck). This portion of the overall smoke plume was what the MISR footprint revealed to be low-mid-tropospheric smoke. Notice the gradient in AOD toward the visible thicker smoke; AOD values peaked here between 2.0 and 3.0. The CTP/AOD composite in Figure 3.7b reveals the reason for the aerosol retrieval boundary—the majority of the plume was identified as cloud. Not shown, but worth noting, the MODIS cloud optical depth map showed the plume to have cloud optical depth values at the lowest CTP (i.e. highest altitude) significantly smaller than for the adjacent water-ice clouds, generally by a factor of 5. Thus the peculiar, combined visible and IR signals from the young Chisholm plume confounded the operational MODIS cloud and aerosol retrievals. It may be instructive though to note that the MODIS visible AOD at the fringe of the plume was strongly increasing and peaking at values ~3, suggesting that the true visible AOD of the plume core was much greater.

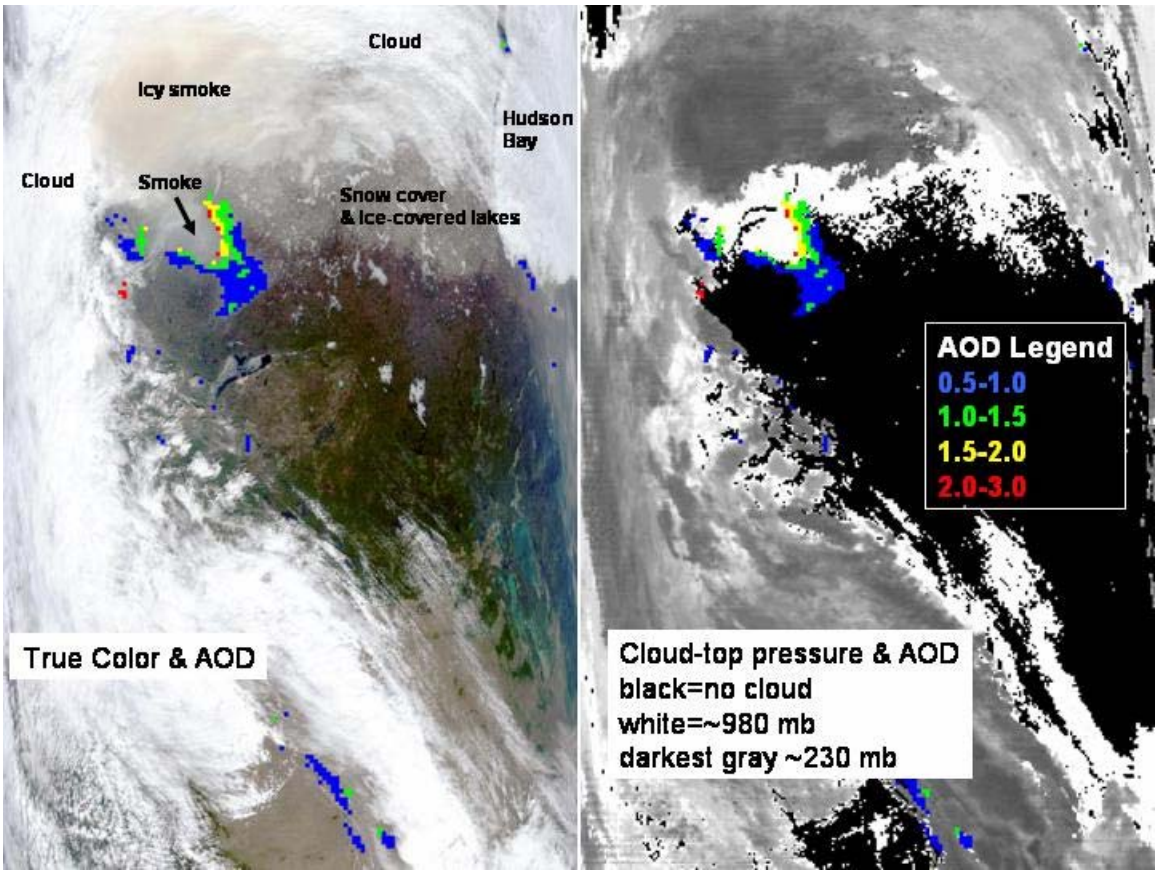

Figure 3.7. Composite of MODIS true-color and level 2 AOD (left); level 2 cloud-top pressure and AOD (right). Image date/time is 29 May 2001, 1840 UTC. Features are labeled.

3.3.2.5 MISR

The eastern portion of the Chisholm plume sampled by MODIS was simultaneously sampled by MISR also on the Terra satellite (Figure 3.8). The natural color view is from the MISR 60° forward viewing camera. A pall of yellowish smoke is apparent both above the surface and clouds. The smoke appears thicker at the oblique view angle, thus better areal coverage is obtained and the height retrievals are less sensitive to the underlying cloud deck. The right-side panel is a specially-generated stereo height product using MISR's 46° and 60° forward-pointing cameras. The southern portion of the smoke cloud is at an altitude of about 3.5 km; however, the smoke further to the north is at heights of about 12-13 km above mean sea level

(amsl). The height fields pictured here are uncorrected for wind effects; wind-corrected heights (which have higher accuracy but sparser spatial coverage) for this smoke pall are about 0.5 km higher.

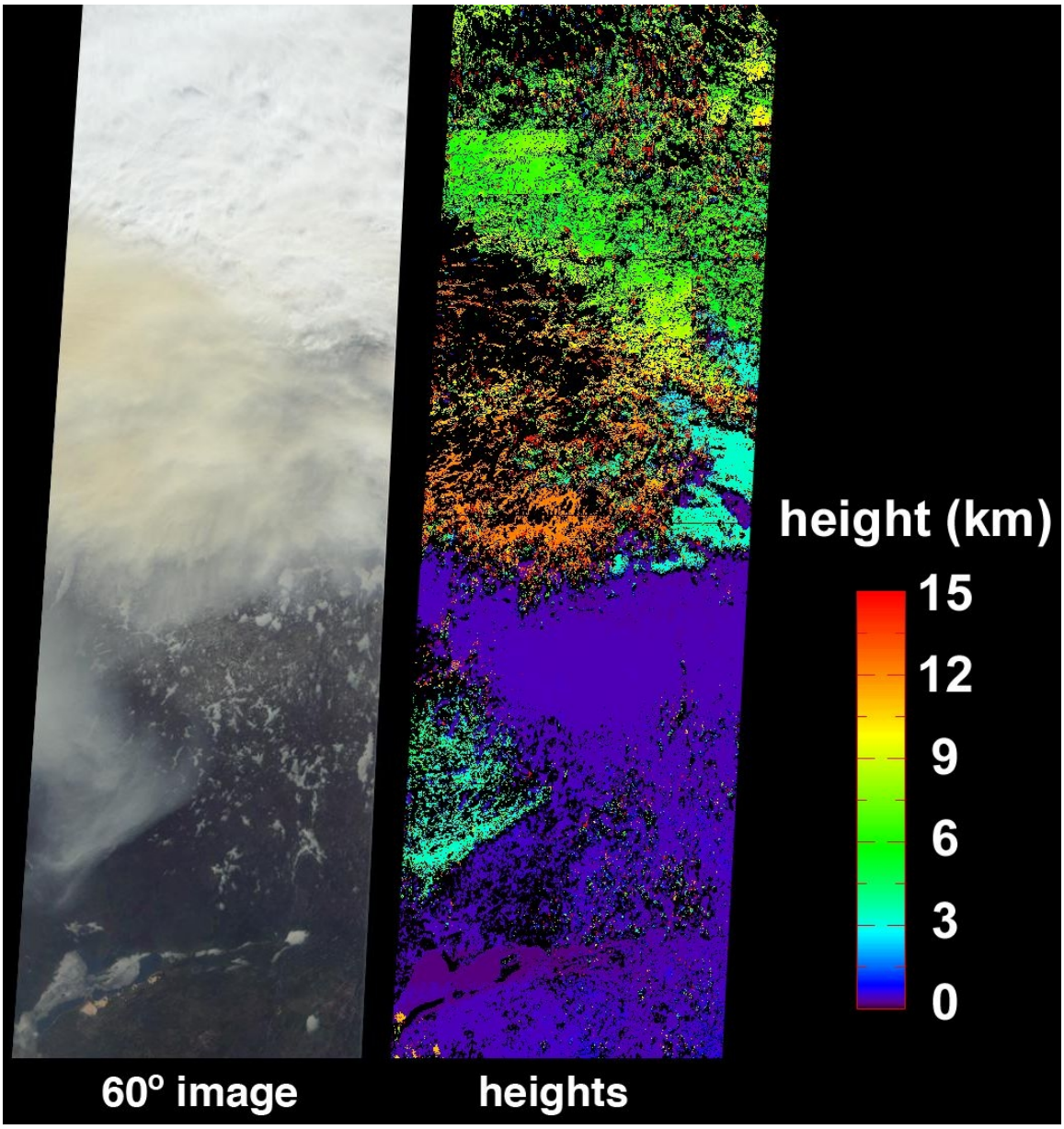

Figure 3.8. MISR true-color and stereo heights of 1840 UTC 29 May 2001 Chisholm plume and meteorological cloud to the northeast. The true-color image is from the 60° forward camera. The stereo heights are a special retrieval using MISR's 46° and 60° forward-pointing cameras.

Figure 3.9 shows a "profile" of MISR stereo height from the scene in Figure 3.8. This is simply a frequency distribution of the heights, and we focus on the local

maxima. From these we conclude that there are primarily three cloud or plume decks in the MISR scene. By sub-setting the stereo height image we can identify the distinct compositions to the three decks. The lowest deck, at ~3.2 km amsl, is the tongue of smoke in the southern portion of the MISR scene. The water-ice cloud deck is mostly between 6.5 and 8.0 km. The high smoke is grouped at 12.0 km, 2-3 km above the tropopause, which here is determined from the 12 UTC 29 May radiosonde from Fort Smith, NT (not shown). The MISR stereo height retrievals of the "day-after" Chisholm plume are the first independent, objective assessments of the initial stratospheric injection potential of a pyroCb.

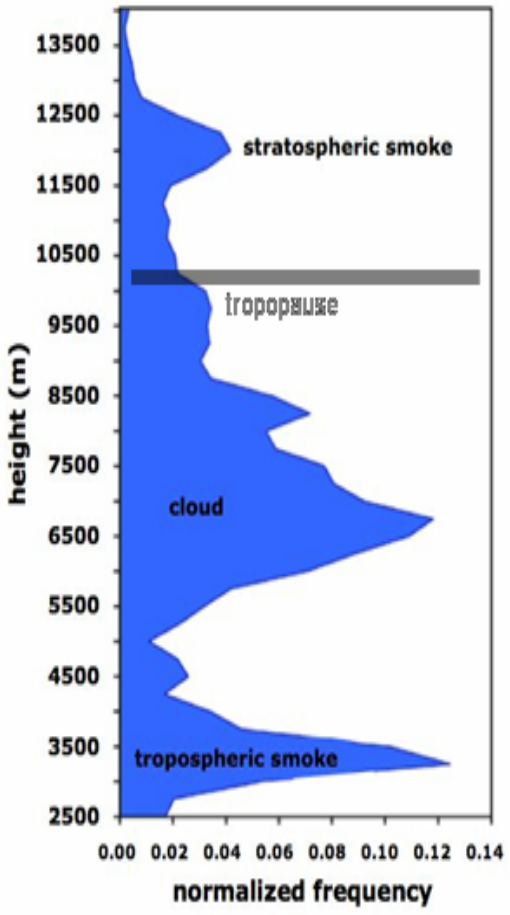

Figure 3.9. "Profile" of MISR stereo heights. This is a stereo-height frequency distribution. Local maxima and the cloud/plume subscenes which they represent are labeled. Tropopause height from Fort Smith (60°N, 110°W) radiosonde is marked by the gray bar.

3.3.2.6 TOMS AI

Next we introduce level 2 TOMS AI (Figure 3.10). Each pixel is mapped at its effective resolution taking into account the TOMS scan pattern. The time of these measurements is ~18 UTC, about 45 minutes earlier than the Terra overpass, thus sampling approximately the same scene as Terra. The peak AI is 31.2 in the core of the smoke plume, roughly where the MODIS color of the smoke is intense brown. In the version 7 result reported by FS03, the plume core AI had an artificial limit of 12.8, thus we see an immediate advantage to the version 8 AI retrieval. In our investigation of level 2 AI for other thick and deep smoke plumes (which includes published cases cited in Section 1 and several other works in progress), the peak value of 31.2 is unrivaled. Although the aerosol index is ultimately a qualitative indicator, the relevance of values in the 20s and 30s is evident in the context of the MODIS smoke color, low brightness temperature, and MISR stereo heights—they signify a plume with particularly high absorption optical depth and high altitude aerosols. Next we attempt to explore these relations more exhaustively.

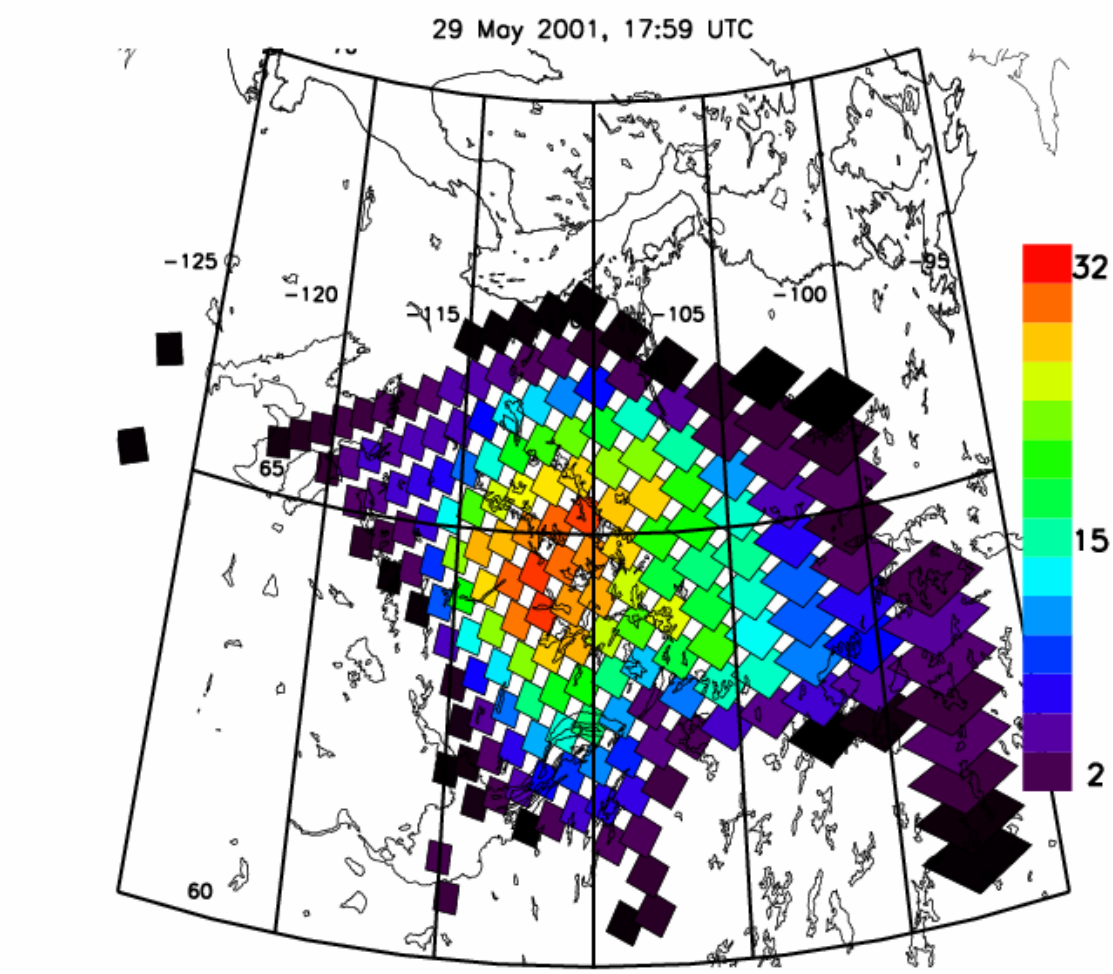

Figure 3.10. Earth-Probe TOMS level 2 aerosol index at ~18 UTC 29 May 2001.

3.3.3 Plume and Cloud Height

The combination of satellites viewing the 29 May Chisholm day-after plume allows us to obtain greater insights into the cloud/plume complex. We choose 65°N for a slice through the core of the smoke. In Figures 3.11 and 3.12 we show MISR, MODIS, and TOMS data within ±2° latitude, from 125° to 95°W, which spans the smoke pall and continues through a solid deck of pure water-ice clouds to the east and west. In each figure we plot individual pixel values and a solid line, a boxcar average chosen to discern a general pattern but preserve small-scale structure.

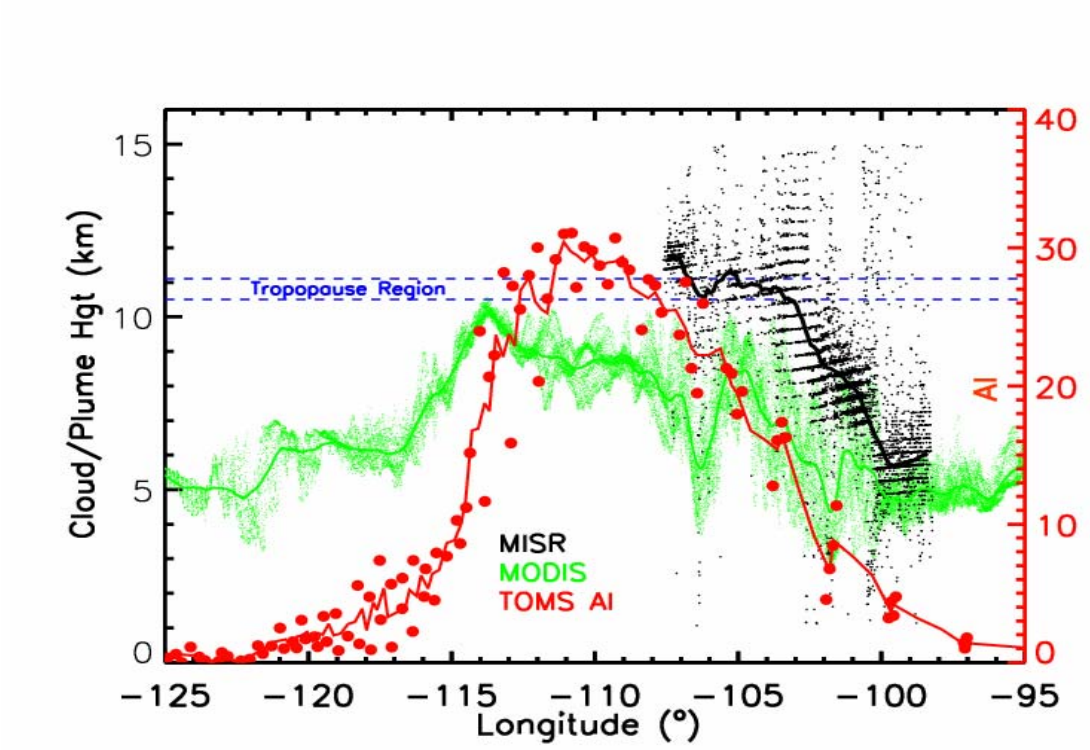

Figure 3.11. Analysis of MISR stereo heights, TOMS AI, and MODIS IR-inferred cloud tops along the 65°N parallel. All pixels within 2° of 65°N are shown. For details of MODIS BT-to-cloud-top altitude determination, see text. Lines through each data item are from boxcar smoothing. For tropopause-region determination, see text.

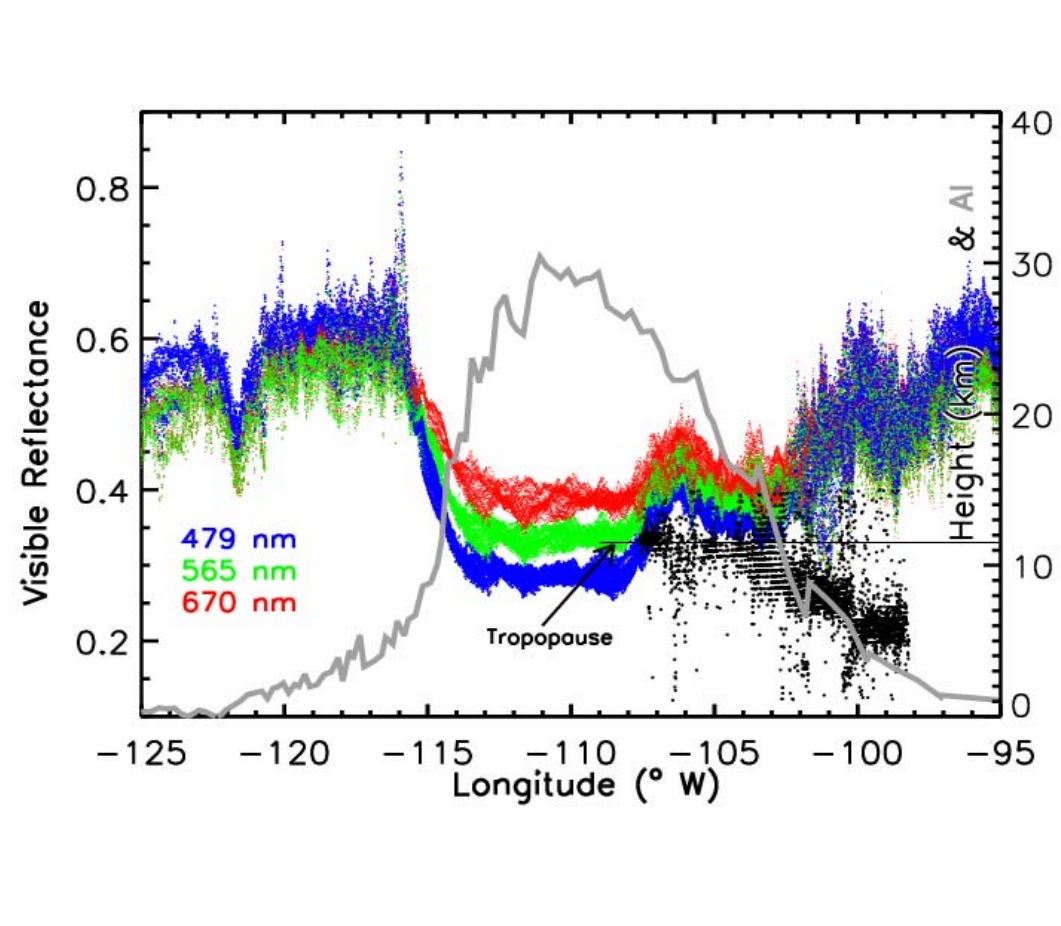

Figure 3.12. Analysis as in Figure 3.9, but with MODIS true-color-channel reflectances instead of cloud-top. Each color channel is appropriately color coded.

Figure 3.11 contains MISR stereo heights and TOMS AI, and an effective opaque cloud-top height derived from MODIS THIR BT. Here we use a temperature profile from National Centers for Environmental Prediction (NCEP) Reanalysis [Kalnay et al., 1996] for 12 UTC 29 May interpolated to 65°N, 110°W for the BT-height relation. We see that the entire slice is comprised of cloud; i.e. BT gives an unbroken stretch of elevated heights, from 3.0 to 10.5 km. Cloud tops estimated in this way are near 5 km amsl at the east and west ends, and rise toward the center longitudes. To assess cloud altitude with respect to the tropopause, we determine the local tropopause region using two approaches. The top of the tropopause region is the altitude of the temperature minimum, averaged from the radiosonde profiles at Fort Smith (60ºN, 110ºW) and Cambridge Bay (69ºN, 105ºW) for each station's two

29 May measurements. This value is 11.1 km. The tropopause height is calculated by the dynamical definition, using potential vorticity equal to 2.5 potential vorticity units, for the 12 UT 29 May NCEP reanalysis fields. That gives a tropopause height at 65N, 110W of 10.5 km. The opaque cloud tops rise to the tropopause at 114°W. Both AI and BT-estimated cloud heights rise toward the center of this slice at 65°N. At the east and west edges, the AI is essentially zero, which means no absorbing aerosol above the surface observed by TOMS. The sharpest gradients of AI are where the MODIS BT-height gradients are also largest, between ~114°-116°W and 102°-105°W. In the plume-core longitudes, where the BT-height is greatest, the correlation with AI breaks down. The peak AI is at ~111°W, about 3° east of the deepest opaque cloud top. Considering the very strong aerosol signal in the MODIS color throughout the core of the plume, the peaking of AI at 111°W may well indicate a local maximum in plume altitude instead of an increase in optical depth. This decoupling of the correlation between THIR BT and AI would occur if the smoke aerosols here were small enough to be transparent to emitted 11μm radiance. In summary the strong positive correlation between the AI and BT-height gradients approaching the plume core indicates that the plume-core AI variation reveals a local maximum in smoke altitude.

We can assess this independently with the MISR stereo heights. Even though the MISR swath does not cover the entire slice in Figure 3.11, these data offer a distinct advantage over MODIS THIR BT, because the stereo height retrieval does not depend on THIR opacity. Moreover, the MISR swath contains both meteorological cloud and smoke, and covers a portion of the AI swath where values range from marginal to extreme. We see that in the eastern edge of the MISR swath, where AI is ~3 (just above noise levels), the typical MISR stereo height (~5.7 km) is relatively close to the BT-height estimate (~5km). Here the dominant reflecting layer is the water-ice cloud deck. But the rapidly "thickening" smoke to the west gives MISR stereo heights that increase more rapidly than the MODIS BT-height estimate. Near the western edge of the MISR swath, where AI is over 20, the MISR-MODIS height difference is between 2-5 km. At the western edge the central values of MISR

stereo height are above the tropopause and the east-to-west slope is still positive. Here the AI slope is also positive. Thus it appears that the smoke plume to the west of the MISR swath at 65°N continues to increase in height and is mainly in the lowermost stratosphere. It is not possible to resolve the relative contribution of increasing AOD and plume altitude for the peaking of AI, but we attempt to address that by invoking MODIS visible data in Figure 3.12.

In Figure 3.12 we keep the MISR stereo heights and TOMS AI, but replace MODIS IR data with visible reflectance at the three wavelengths used in the true-color imagery. By plotting these, color coded accordingly, we can infer changes in AOD by changes in color with respect to the general whiteness of the water-ice cloud deck that covers the west and east extrema of the slice at 65°N. The white water-ice cloud by definition gives approximately equal reflectances at the three true-color wavelengths. The brown hue of the smoke plume (see Figure 3.4a) is a result of relatively small reflectance contribution at the short (i.e. blue) wavelength, and dominance of red plus green wavelengths. Total brightness of the scene can be inferred by the "sum" of the three channels' reflectances. On the west and east edges of the scene in Figure 3.12, where the water-ice cloud deck dominates, the total visible reflectance is large while the red and green reflectances are equal to or even less than the blue-channel reflectance. Toward the center from each direction the blue-channel reflectance diminishes preferentially, first in a transition zone, and bottoms out between 108.5 and 113W, where there is no discernable change in the intensity of the red+green versus blue reflectance. This may be viewed as a zone where the color-inferred aerosol abundance is both large and essentially unchanging. But it is within this zone that the smoothed AI line increases to a peak at 111°W. Considering our earlier interpretation of the increasing AI being strongly driven by plume altitude, this peaking of AI in the zone of thickest—and approximately constant--smoke aerosol suggests increasing plume altitude even above the high west-end MISR values.

3.3.4 Stratospheric Smoke Mass

We can estimate the mass of smoke injected into the lower stratosphere using inferences gained from the previous analysis. The synthesis of the AI with MODIS and MISR allows us to conclude that the parts of the Chisholm plume with AI greater than a certain threshold are above the tropopause. The analysis of Figures 3.11 and 3.12 lead us to use AI=15 for a stratospheric-aerosol threshold. For comparison we will also use a larger (i.e. more conservative) threshold of AI=19.

The use of the TOMS near-UV measurements to retrieve aerosol properties over clouds is a challenging enterprise. The cloud-free approach [Torres et al., 1998, 2002b] is not directly applicable here because, in addition to the known dependences of the AI on aerosol micro-physical properties and total optical depth, the albedo of the bright reflecting background must also be known. Although the aerosol-layer height-dependence when the aerosol is above a bright surface is reduced [Torres et al., 1998, de Graaf et al., 2005] the relative cloud-aerosol separation must also be accounted for. However we can use the heights of the smoke plume and the cloud layer from MISR. In spite of these difficulties we have attempted a quantification effort taking advantage of current ongoing work by Omar Torres towards the development of a retrieval approach of aerosol absorption over clouds. Sensitivity analyses (not shown) indicate that the conversion of AI to extinction optical depth and single scattering albedo by an inversion procedure requires accurate characterization of the reflecting lower boundary. It is possible however, to directly derive an estimate of the aerosol absorption optical depth because the uncertainty attributable to cloud albedo affects the derived extinction optical depth and single scattering co-albedo in opposite directions. Therefore, a cancellation of errors takes place, and a realistic estimate of the absorption optical depth can be obtained provided that other relevant input (i.e., aerosol particle size distribution, and aerosol layer height) are accurately characterized. We have preliminarily applied this inversion approach to the TOMS observations of Chisholm plume on May 29. The particle size distribution is based on Aeronet observations for biomass burning

aerosols [Torres et al., 2002b]. The aerosol layer height derived from MISR observations is assumed in the retrieval. A cloud top at 600 hPa was also assumed. Under these assumptions the distribution of the absorption optical depth was obtained. These results are just an attempt to express the qualitative AI parameter into a more physically meaningful quantity and should be regarded as very preliminary. The derived aerosol absorption optical depth could be off by as much as a factor of two.

We calculate smoke mass using extinction AOD, derived from absorption AOD divided by the co-single-scatter-albedo (1- ω_0). The extinction AOD for 29 May is shown in Figure 3.13, where a typical value for forest fire smoke of 0.9 is used for ω_0 [Reid et al., 2005b]. Mass per pixel is then the product of the extinction optical depth, specific extinction, and pixel area. We assumed a specific extinction-mass factor of 5 m^2/kg [Reid et al., 2005a]. We will calculate aerosol mass this assumption and two bounding values for ω_0, 0.7 and 0.95 to cover a suitable range given for smoke in the literature. Hence the derived extinction AOD will vary by a factor of 1/3 to 2 from those shown in Figure 3.13.

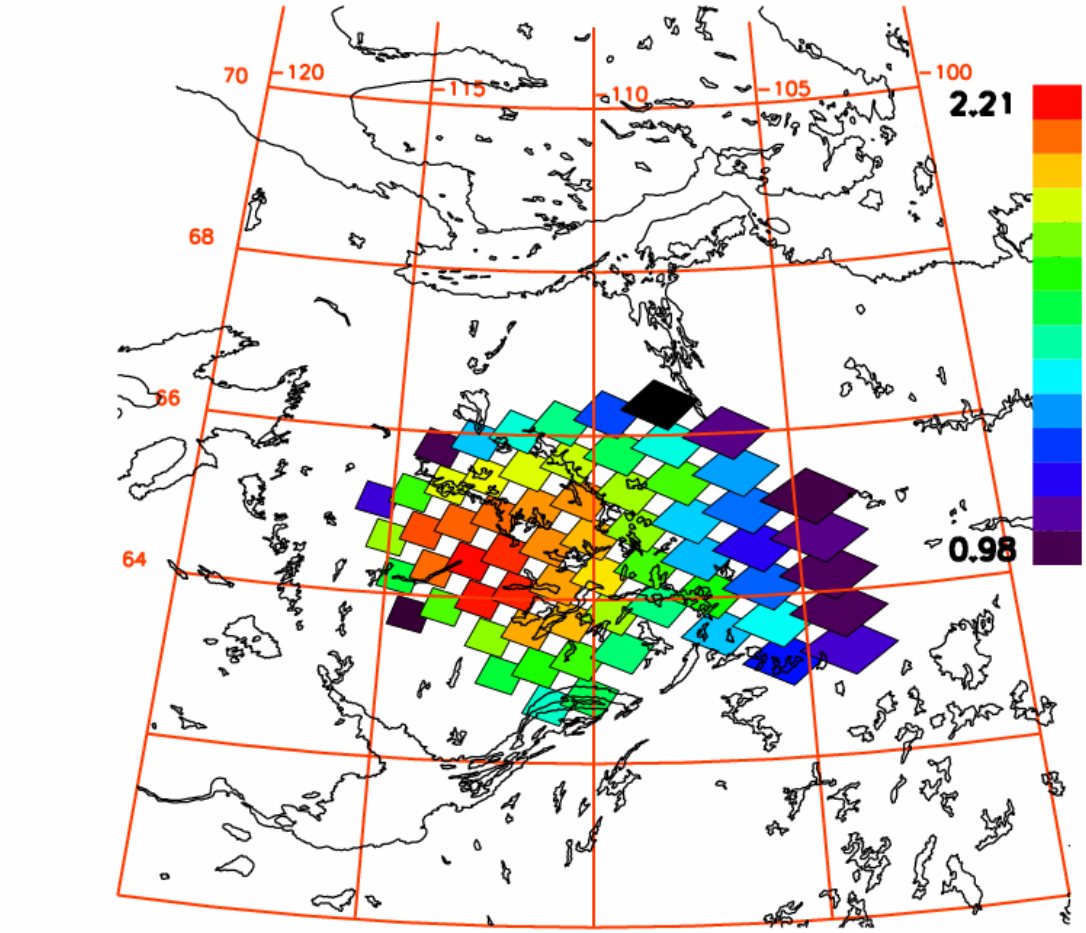

Figure 3.13. Derived extinction AOD on 29 May 2001 from TOMS AI for pixels with AI >= 15. Single scatter albedo assumed as 0.9. See text for details.

Integrating the TOMS pixel footprint for the above-mentioned AI threshold gives an area range of 1.17×10^5 to $1.69 \times 10^5 km^2$ (mean=$1.43 \times 10^5 km^2$). The resultant mass of smoke is for the two AI thresholds and five ω_0 is summarized in Table 3.1. As a point of qualitative comparison, we relate this burden to the integrated northern hemispheric stratospheric aerosol burden for near background conditions (1979) calculated by Kent and McCormick [1984]: ~$3 \times 10^5 t$. The Chisholm pyroCb injected a mass of smoke aerosol equivalent to between 4.6% and 36.3% of the background hemispheric aerosol load. The mean value, for the AI=15 threshold, is 14.8%.

Table 3.1. Chisholm stratospheric smoke plume mass (10^4 tons) for two stratospheric AI thresholds and six ω_0 assumptions.

ω_0	AI=15	AI=19
0.70	1.8	1.4
0.75	2.2	1.7
0.80	2.7	2.2
0.85	3.6	2.8
0.90	5.5	4.2
0.95	10.9	8.3
Mean	4.4	3.4

Now we reconcile the stratospheric smoke injection with the emission from the Chisholm fire during pyroconvection. Area burned during the blowup on 28 May was approximately 50000 ha [Luderer et el., 2006 and references therein]. Total particulate matter emitted (TPM) from an area burned is expressed per equation (1)

TPM = Emission factor x Fuel load/area x Area burned (1).

Combusted fuel consists of surface and crown matter. For the area burned during the 28 May pyroconvection this is the sum of ~9.0 kg/m^2 for the surface [ASRD, 2001] and 1.0 kg/m^2 for the crown [Brian J. Stocks, personal communication, 2007], giving a fuel consumption of 5x10^{6}t. For emission factor we take two values from Table 6 of Reid et al., [2005a] for temperate/boreal forest, to give a range of emissions (expressed as the ratio of kg emitted to kg consumed): those of Hobbs et al. [1996] (.018) and Nance et al. [1993] (.029). These bracketing values result in total particulate emissions between 9.0x10^{4}t and 1.45x10^{5}t. From Table 3.1, the stratospheric smoke-mass injection from the Chisholm pyroCb was between 0.3% and 2.2% of fuel consumed during pyroconvection. In relation to TPM, the fraction of stratospheric smoke was between 9.6% and 121.0%. The mean, for the AI=15 threshold, and mean TPM (1.175x10^{5}t), is 37.9%. The simulation of the Chisholm pyroCb by Trentmann et al. [2006] resulted in a stratospheric aerosol injection proportion of 8%, near the low end of the range reported here. Obviously the fact that

the upper value exceeds 100% suggests that ω_0=0.95 is unrealistically large for the Chisholm plume or TPM estimates in this case are too low.

3.4.0 Comparison of 29 and 30 May Views

Figure 3.14 contains the MODIS daytime views of the Chisholm smoke one day later, on 30 May (1745 UTC). The plume has been stretched and advected under the influence of anticyclonic wind. At this time the plume extends from Northwest Territories, across Hudson Bay and into the Great Lakes and Michigan. UTLS-level wind direction in the Hudson Bay and USA part of the plume is northerly (not shown). According to the true color image in Figure 3.14a the smoke is evidently thinner than on 29 May. Skies over land surfaces adjacent to the plume in Canada and the USA are apparently cloud free. Hudson Bay appears to contain widespread ice and some overlying water-ice cloud, detectable through the translucent smoke. The THIR image of Figure 3.14b reinforces the determination that land areas of the upper Midwest US and Manitoba are cloud free. Northern Hudson Bay has opaque low and mid-tropospheric cloudiness. The smoke plume from James Bay to Lake Superior appears to have a residual signal in THIR, indicating that the transition from opaque smoky ice to transparent smoke is not yet complete, ~1.5 days after pyroconvection.

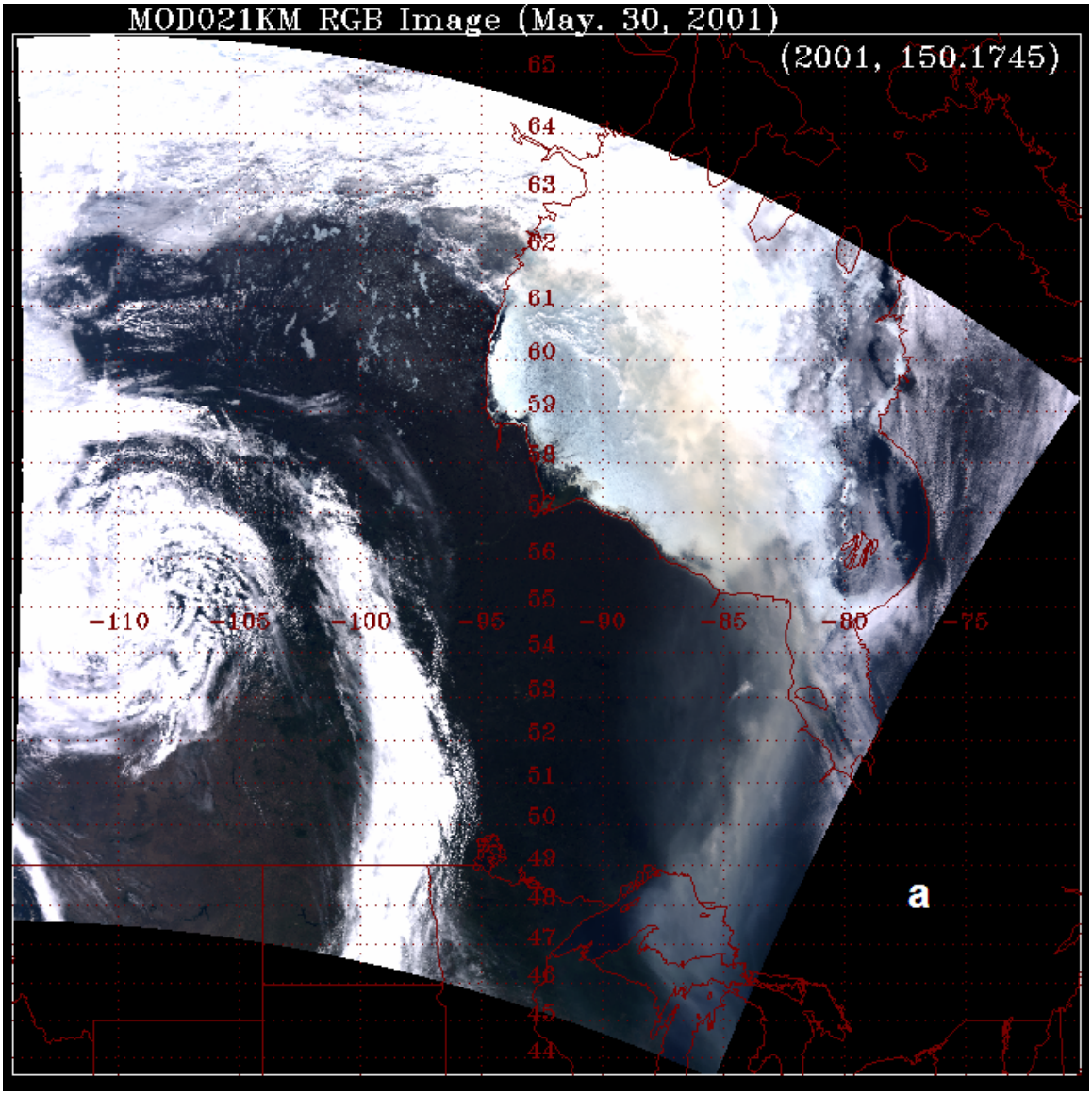
MOD021KM RGB Image (May. 30, 2001)
(2001, 150.1745)
65
64
63
62
61
60
59
58
57
56
55
54
53
52
51
50
49
48
47
46
45
44
-110
-105
-100
-95
-90
-85
-80
-75
a

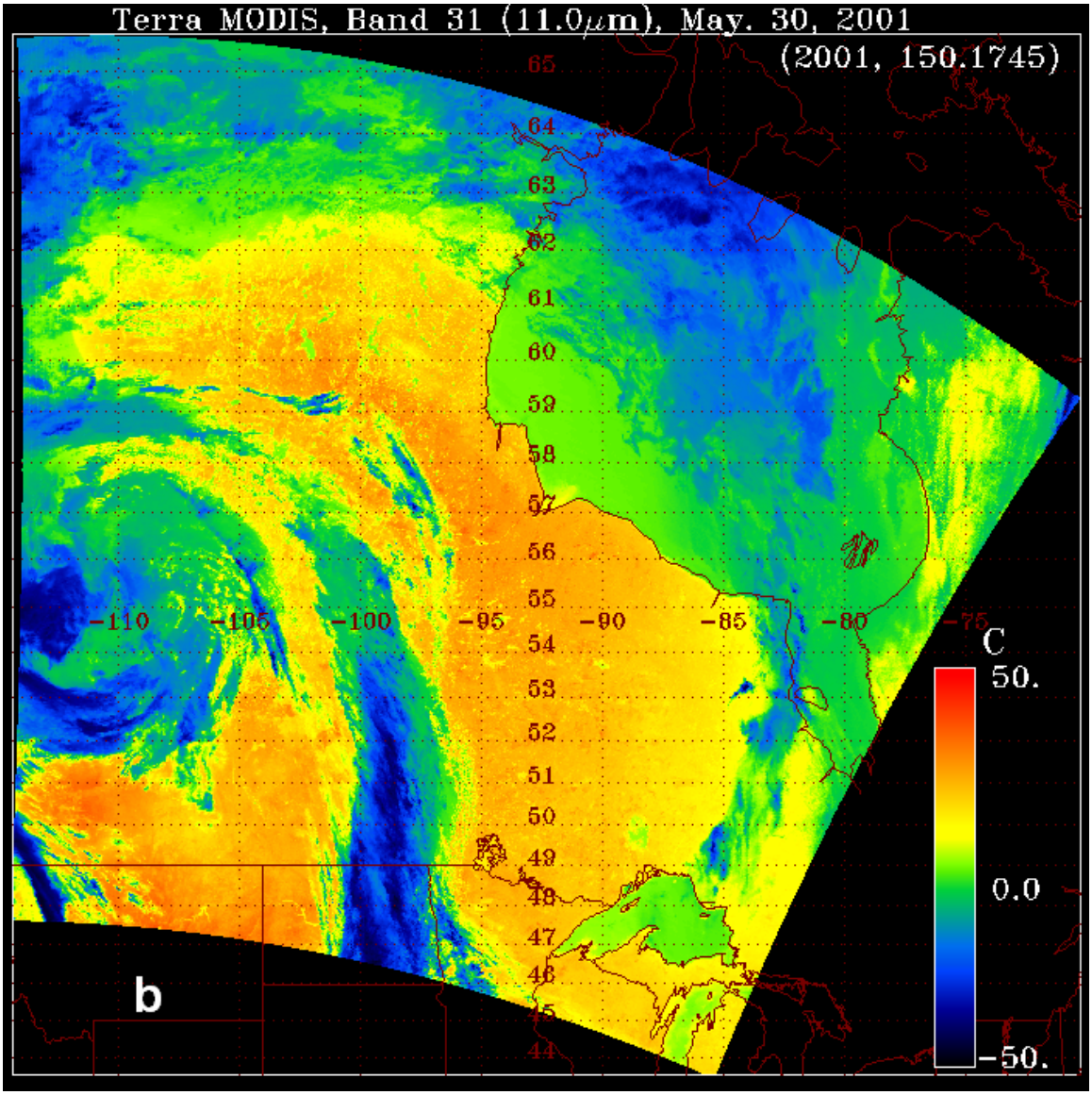

Figure 3.14. MODIS stretched true color (a) and 11μm BT (b) images for 1745 UTC 30 May 2001.

TOMS AI map for 30 May is shown in Figure 3.15a. The times of the Terra and Earth-Probe overpasses coincide within two hours. Not surprisingly, the same general shape of the MODIS view of the plume is reproduced. However, the AI gives detail that allows us to infer local extrema in plume altitude. There are two local AI maxima. In both areas AI>20, values representative of the core of the 29 May plume. At neither AI maximum is the visible optical thickness (as inferred from Figure 3.14a) apparently as large as it was on 29 May—thus the local AI extrema may

indicate plume altitude extremes. One of the maxima is west of James Bay. Here the plume in the true-color MODIS view is obvious, but portions of the plume south of the AI maximum and north of the Canada/US border are equally optically thick in the visible--and THIR--but do not have such a large AI signal. Thus this and the other AI maximum to the north may identify where the plume protrudes most deeply into the stratosphere.

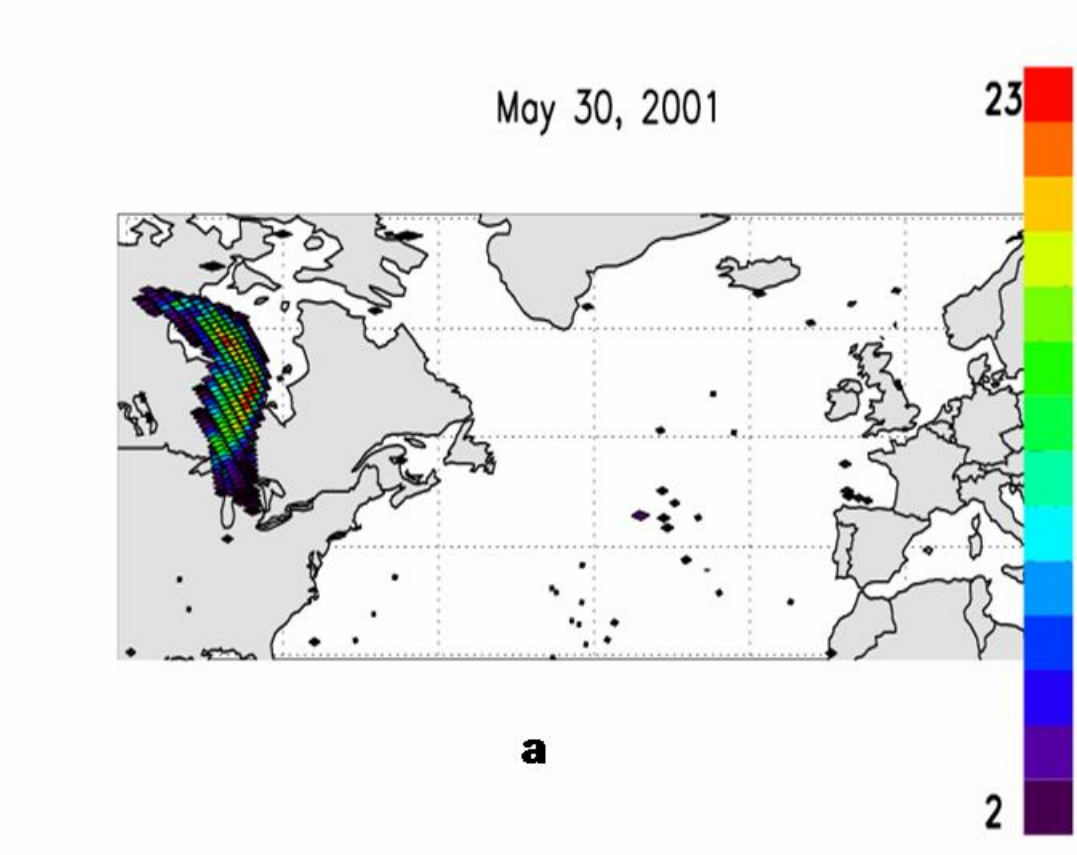

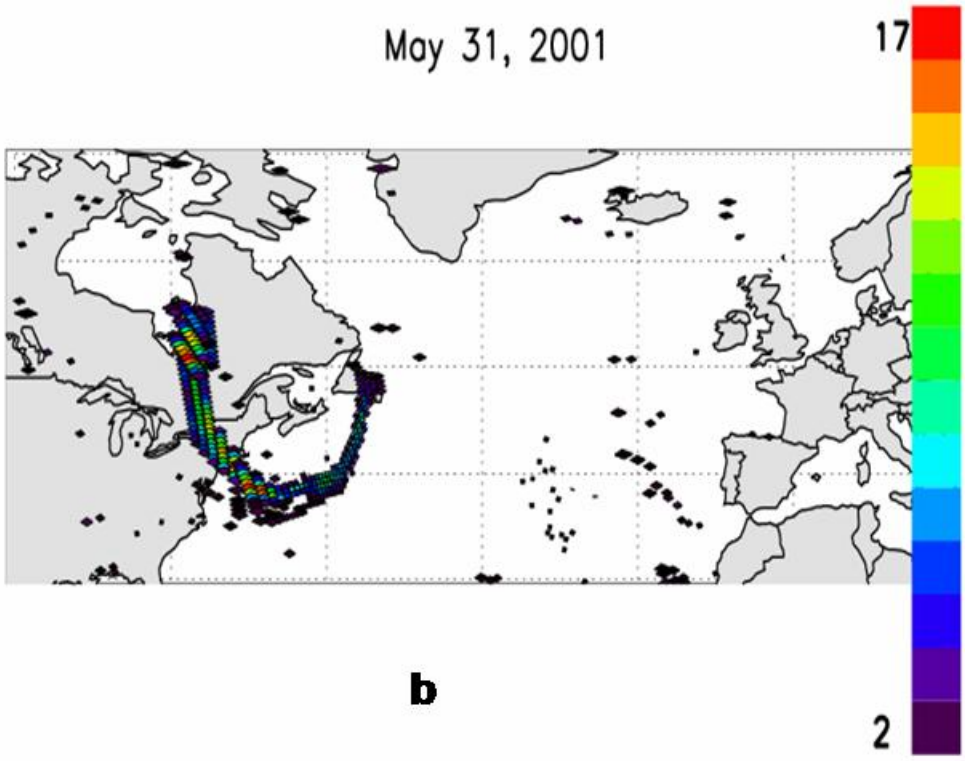

b

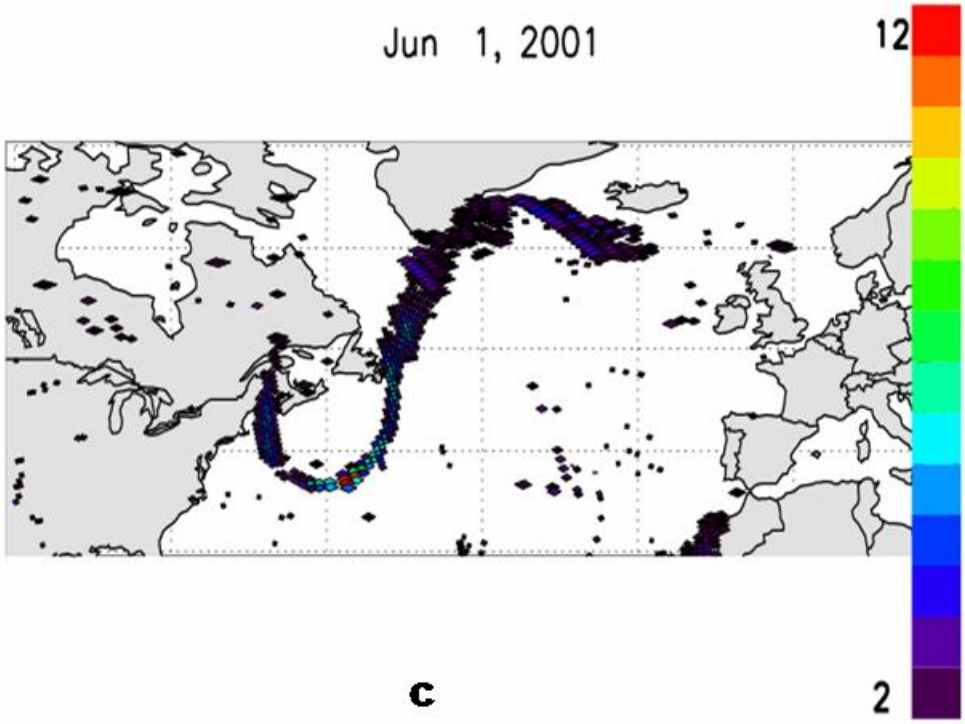

c

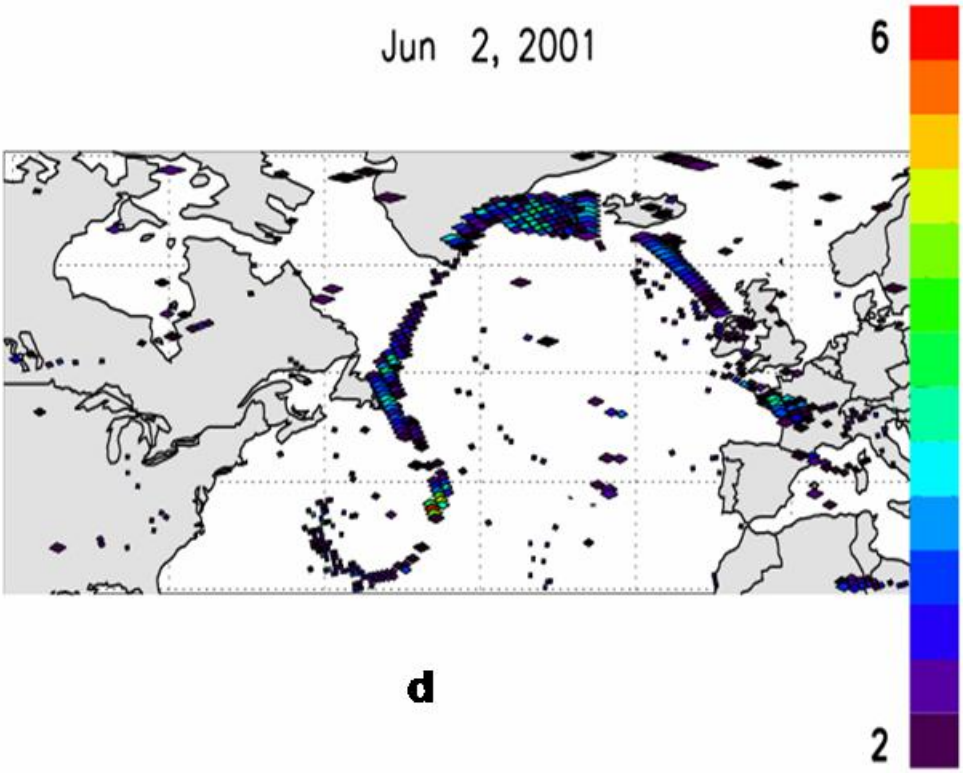

d

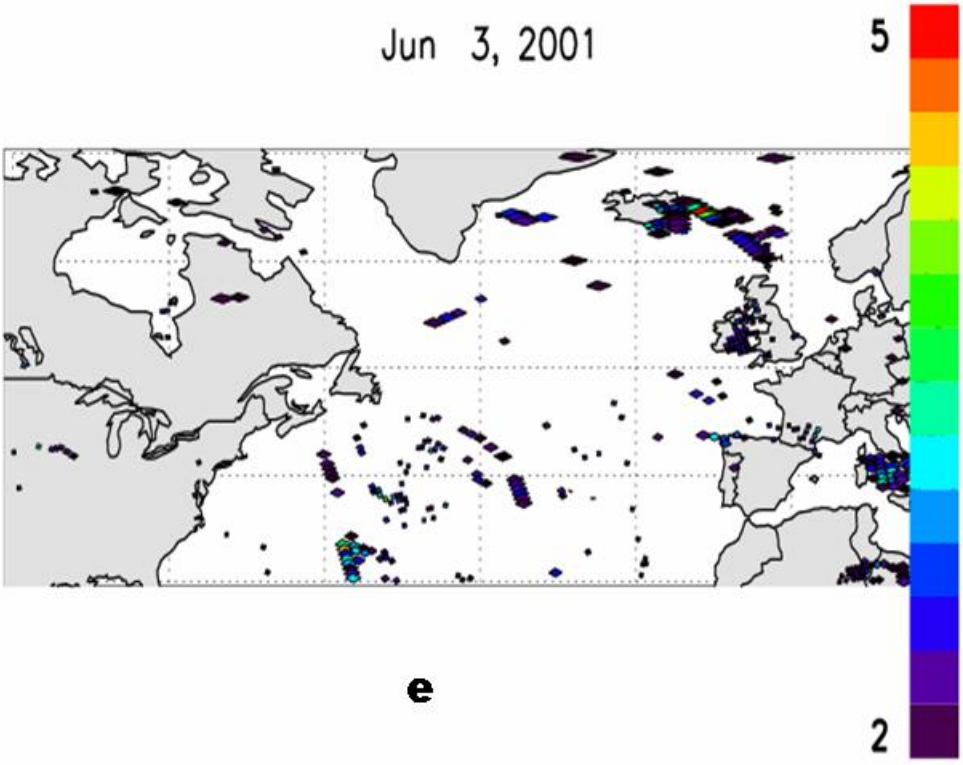

e

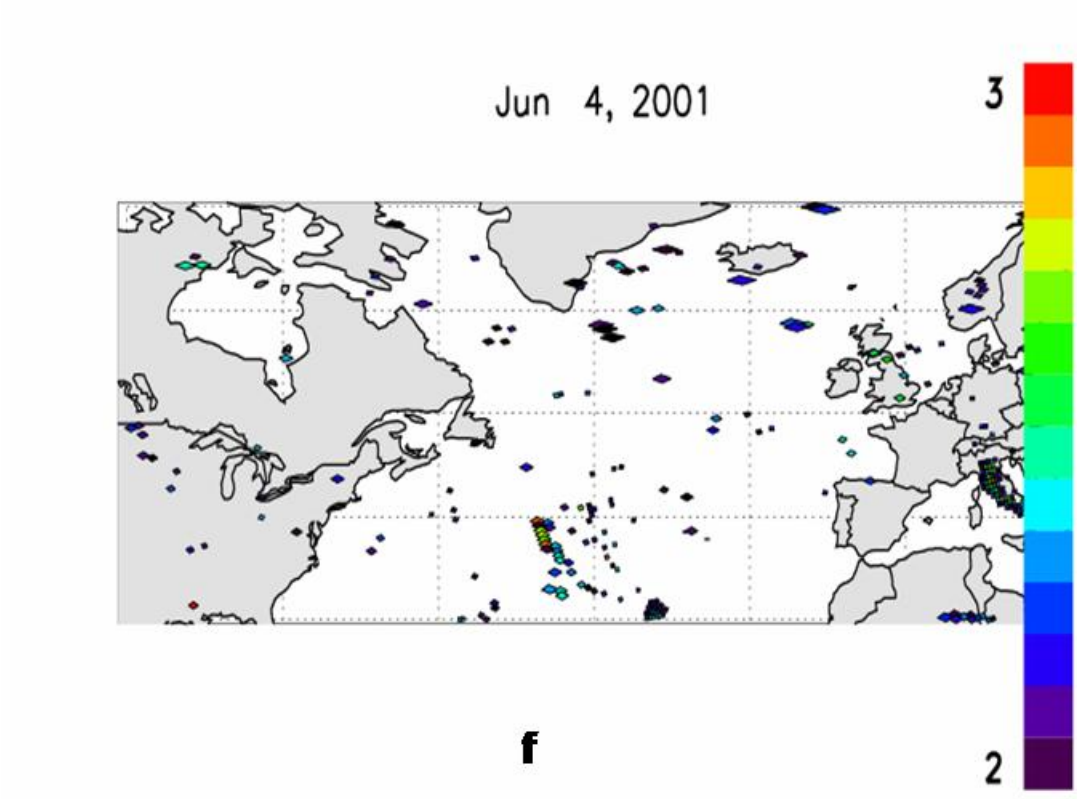

Figure 3.15. TOMS level 2 AI for 30 May – 4 June 2001 (a-f). Pixel rainbow color scaling goes from AI=2 to the daily maximum.

The two afore-mentioned AI maxima lag upstream of plume's forward edge over Michigan. Considering our determination that the core of the 29 May plume topped out in the lower stratosphere—hence above jet stream altitude—it is reasonable to conclude that the vertical range of the young Chisholm smoke plume spanned the UTLS; and as it deformed during advection the smoke at jet-stream level advanced far beyond (i.e. to Michigan on 30 May) the highest stratospheric smoke over and/or near Hudson Bay.

3.5.0 The Chisholm Plume's First Week

The evolution of the Chisholm smoke plume for the balance of its first week of existence is captured in the AI maps of Figure 3.15. As expected, the maximum AI on each day between 31 May and 4 June declines as the plume shears horizontally.

The plume snakes into a wave signature on 31 May, crossing the US Atlantic coast and extending to Labrador. Note the reproduction of two localized AI maxima, one in "mid" plume and the other lagging over James Bay. On 1 June, as the plume takes on a complete wave signature between Quebec and just south of Iceland, a distinct AI maximum appears in the "trough" of the wave over the Atlantic near 38N (again lagging far behind the plume's leading edge). By 2 June the leading portion of the Chisholm smoke plume passes over the United Kingdom and resides as far eastward as France, while the western portion (including the AI maximum) starts to form into an apparent cyclonic shape over the central Atlantic. On 3 and 4 June the AI pattern breaks up; the downwind (i.e. eastern) edge enters the Mediterranean region while the lagging plume over the central Atlantic appears to swirl and stagnate. In general the persistence of an AI plume for one week and the distance between Alberta and the Mediterranean Sea is by itself an indicator of an extremely unusual aerosol perturbation. This perturbation consists of a large abundance of aerosol material and a residence altitude likely from upper tropospheric jet stream levels to several km into the lower stratosphere.

3.6.0 Summary

Our aim was to quantify important parameters related to a young stratospheric smoke plume. The Chisholm (Alberta) pyroCb of 28 May 2001 is an excellent example of the most extreme form of pyroconvection because of the many space- and ground-based observations of the blowup and aftermath. Here the focus was on the immediate aftermath (from hours to 1 week old), which is an important timeframe for regional or global transport/chemistry/cloud-process models to consider as initial conditions.

The Chisholm pyroCb has now been confirmed to have injected a large quantity of smoke into the lower stratosphere, even above the altitude of the local temperature minimum, as evidenced from satellite imagery less than ½ day after the pyroconvection ended. MISR stereoscopic height retrievals give the first

independent, objective, and detailed confirmation of stratospheric smoke in a young pyroCb plume. MODIS true-color and IR imagery, TOMS aerosol index and MISR stereo heights together allowed us to gain advanced insights into these peculiar UTLS pyroCb plumes. For instance, level 2 AI can reveal variations of plume altitude within a broad or optically thick plume.

The Chisholm pyroCb stratospheric plume on the day after injection covered an area of approximately1.43×10^{5} km^2, with a mass estimated at between 1.39×10^{4} and 10.89×10^{4}t. This represented between 0.3% and 2.2% of the total fuel consumed during pyroconvection. It also represented between 10 and 121% of the total particulate emissions, calling into question typical assumptions for single scatter albedo of forest fire smoke or emissions estimates/assumptions in this case. The stratospheric mass injection also was related to hemispheric sulfate aerosol background burden; estimated to be roughly 15% of hemispheric aerosol by mass.

Several peculiar traits of the Chisholm plume were in evidence in the earth-viewing satellite data. For instance, the THIR GOES animation of the first day of plume existence showed that the core BT was close to or even colder than the ambient atmosphere's temperature minimum for ~13 hours after pyroconvection. During that time the BT minimum actually decreased for about 8 hours. The plume was obviously smoke-dominated as inferred from the brown color in MODIS imagery, but was also distinctly colder than all neighboring clouds, a combination that confounded both the operational MODIS cloud and aerosol retrieval algorithms. Split window BTD analyses were useful in distinguishing the smoke plume from water-ice clouds, indicating the smoky-ice was composed of particles less than half the ice-particle effective radius.

Visible reflectance and THIR analysis of the "day after" Chisholm plume led us to conclude that the uppermost particles in the young plume were a peculiar mixture of unadulterated dry smoke and smoky ice crystals significantly smaller than normal high cirrus ice crystals. The color of the plume and AI proved that the

dominant material in the plume was smoke. This smoky cloud's core was effectively opaque in THIR at the tropopause.

The Chisholm smoke plume "dried out" into transparent (in THIR) smoke in a process that exceeded 1.6 days, a significantly longer sublimation time scale than for normal cumulonimbus cirrus blow off. AI of the aging Chisholm plume was used to locate the maximum stratospheric plume height, which lagged far behind the leading edge. After one week the plume's leading edge had snaked as far east as the central Mediterranean; a portion (perhaps the highest smoke) of the plume lagged, stagnated, and circulated over the mid-Atlantic. The companion paper by Fromm et al. [2007] presents initial profile measurements of the Chisholm plume there on 5 June and upstream over Quebec (near the tail end of the AI plume) on 1 June.

For the first time, several important initial constraints are placed on an extreme pyroCb event that polluted an entire hemisphere (see the companion paper, Fromm et al. [2007]). A single pyroconvective explosion has now been documented from the ground to the stratosphere with metrics that will enable comparisons with other pyroCbs, volcanoes, and conventional aerosol measures for the stratosphere.

Chapter 4: Stratospheric impact of the Chisholm PyroCb: vertical profile perspective

4.1 Introduction

Extreme pyrocumulonimbus blowups that pollute the stratosphere have been documented on at least five occasions. However the frequency of these events is still uncertain. This chapter synthesizes a broad array of space-, balloon-, and ground-based profile measurements. The Chisholm pyroCb, which we identify as the singular cause of stratospheric aerosol increase in northern spring/summer of 2001, created a doubling of the zonal average AOD in the lowermost stratosphere. The meridional spread of the plume was from the tropics (20°N) to the high Arctic (79°N) within the first month. The stratospheric Chisholm smoke became a hemispheric phenomenon in midlatitudes and northern tropics, and persisted for at least three months. A size-resolved particle-concentration profile over Laramie, Wyoming indicated a lower stratospheric aerosol with a 2-3-fold increase in volume of particles with radii between 0.3 and 0.6 μm. We also find evidence of localized warming in the air masses of four of the lidar-measured smoke layers. This work contains the first reported stratospheric smoke layers measured by lidar at Ny Ålesund, Esrange, Kühlungsborn, Garmisch Partenkirchen, Boulder, and Mauna Loa. In addition, the first detection of smoke-enhanced aerosol extinction at near IR wavelengths by the Halogen Occultation Experiment (HALOE) is introduced.

4.2. Data

4.2.1 Solar Occultation (SO)

POAM III version 4 aerosol extinction profiles (see Randall et al. [2001] and Russell et al. [2005] for a validation/comparison studies) have been used for analysis of background aerosols, volcanic plumes [Rose et al., 2003], and polar stratospheric clouds (PSC) [Bevilacqua et al., 2002; Fromm et al., 2003; Palm et al., 2005; Alfred

et al., 2007; Daerden et al., 2007], in addition to the above-mentioned stratospheric smoke. Individual profiles of aerosol extinction have an uncertainty of ~10% in the UTLS [Randall et al., 2001]. In the northern hemisphere spring and summer—the period of study—POAM III's measurement latitude is nearly invariant on a daily basis, starting at ~55°N in May, reaching minimum ~54°N at solstice, and increases to ~65°N by September.

SAGE II aerosol extinction profiles have been used in a wealth of applications over its years of operation (1984-2005). For instance, Thomason et al. [1997] used SAGE II extinction coefficient for a global stratospheric aerosol climatology; Rizi et al. [2000] analyzed the plume from the eruption of Shishaldin volcano in April 1999; Wang et al., [1994] presented a climatology of sub-visual cirrus (SVC); Palm et al. [2005] showed SAGE II-measured Antarctic PSCs in 2003; and Fromm et al. [2000] showed both SAGE II and POAM III smoke layers in the lowermost stratosphere in boreal summer 1998. In the northern spring/summer SAGE II sweeps rapidly/episodically through mid and high latitudes, creating a seasonal pattern characterized by brief periods of measurements with slightly longer gaps in between. In northern summer 2001 SAGE II mid- and high-latitude measurements were only available for roughly one-week periods early in May, June, July, and August. In this work we use SAGE II profiles poleward of 25°N.

HALOE [Russell et al., 1993] aboard the Upper Atmosphere Research Satellite (UARS) [Reber et al. 1993] operated from September 1991 until December 2005. Over this span HALOE delivered an impressively continuous and stable record of aerosol extinction coefficient at four near infrared wavelengths (2.54, 3.40, 3.46, and 5.25 μm). Hervig [1999] analyzed a PSC observed by HALOE over the United Kingdom in March 1996. Hervig and McHugh [1999] also used the multiple aerosol extinction wavelengths to analyze and model the characteristics of SVC.

4.2.2 Lidar

We assembled measurements of enhanced aerosols in the lowermost stratosphere from seven lidar instruments. The locations and basic characteristics are listed in Table 1. The search for applicable measurements included searching the NDACC (Network for the Detection of Atmospheric Composition Change, formerly named the Network for the Detection of Stratospheric Change (NDSC)) and consulting instrument principal investigators. The list below represents those data sets offered for this study that had any UTLS measurements between May and August 2001.

Table 4.1. Summary of aerosol lidar instruments and dates of measurement presented in this paper

Location	**Latitude (°N)**	**Longitude (+°east; -°west)**	**Wavelength (nm)**	**Measurement Dates**
Ny Ålesund	78.9	13.9	532	May: 11 June: 24, 29
Esrange	67.9	21.1	532	July: 25-28 August: 3, 14
Kühlungsborn	54.1	11.8	532	July: 9
Garmisch Partenkirchen	47.5	11.1	532	May: 2 June: 12, 23, 26 July: 3
Boulder	40.0	-105.0	532	May: 8, 9, 13, 23 June: 1, 15, 16, 23, 29 July: 15, 17, 28 Aug: 8, 17
Mauna Loa (NOAA)	19.5	-155.6	355	May: 2, 10, 24, 30 June: 21, 26 July: 18, 24 Aug: 3, 8, 15, 23, 29
Mauna Loa (JPL)	19.5	-155.6	532	May: 5, 8-10, 15, 18, 22, 24-26, 30, 31 June: 2, 4, 5, 12, 15, 16, 26, 27, 30 July: 7, 10, 13, 14, 17-20, 23, 24, 27, 31 Aug: 1-4, 8-10, 14, 15, 17, 18, 21, 24, 25, 28, 30

4.2.2.1 Ny Ålesund

Lidar data from Spitsbergen were obtained by the Koldewey Aerosol Raman Lidar which is located in Ny Ålesund at 78.9°N and 13.9°E at the west coast of Spitsbergen. The lidar is integrated in the NDACC station and consisted at that time of a Nd:YAG laser operating at 1064 nm and 532 nm with 30 Hz repetition rate and about 150 mJ pulse energy. Signals for this work have been collected by a 30 cm Zerodur mirror with a field of view of 0.83 mrad. More information regarding the system can be found in Ritter et al. [2004].

In this work data have been averaged over 60 m in space and around 11 minutes in time. The aerosols were retrieved according to Klett [1985] with a lidar ratio (ratio between aerosol extinction and backscatter) of 30 sr in the stratosphere. The necessary boundary condition was chosen to be: average backscatter ratio =1.05 in an interval between 18 and 21 km. Hence, the altitude where the boundary condition was applied is located at least 4 km above the presented smoke layers to decrease the influence of the choice of the boundary condition.

At 14 km altitude the signal-to-noise ratio of the lidar profile is roughly 25, giving rise to an uncertainty of the backscatter ratio of +/- 0.02 per height increment (10 minutes temporal and 60m spatial resolution).

4.2.2.2 Esrange

The University of Bonn lidar at Esrange in northern Sweden (68°N, 21°E) is optimized for operating at a wavelength of 532 nm. The beam direction is fixed vertically and the atmosphere echo is recorded with counting electronics on a 150-m grid for both parallel and perpendicular polarizations during day and night-time operations. In darkness the return from the vibrational Raman scattering on N_2 molecules and the return at 1064 nm are also recorded. The power aperture product is 7 Wm^{-2}. With a clear boundary layer a net signal from 80 km altitude is obtained in 5

minutes of integration time in darkness. The polarization measurements discriminate rotationally symmetric scatterers (e.g. liquid droplets) from asymmetric scatterers (solid particles). Technical and performance details for this lidar have been described by Blum and Fricke [2005].

4.2.2.3 Kühlungsborn

The Rayleigh/Mie/Raman (RMR) lidar at Kühlungsborn, Germany (54°N, 12°E) is designed for the observation of aerosol parameters like backscatter ratio or backscatter coefficient [Alpers et al., 1999], since summer 2002 complemented by temperature profiles derived from a combination of Rayleigh and Raman backscatter measurements [Alpers et al., 2004; Rauthe et al., 2006]. It uses an injection seeded Nd:YAG laser as the lidar transmitter. The laser simultaneously emits the fundamental wavelength (1064 nm) as well as the second and third harmonic wavelengths (532 and 355 nm). The pulse energies are 500, 400, and 200 mJ, respectively, and the pulse repetition rate is 30 Hz. In this study, only the backscatter at 532 nm is examined. For the signal detection two telescopes with parabolic principal mirrors of 50 cm diameter are used. One of the mirrors is equipped with a polarizer plate that is adjusted perpendicular to the polarization plane of the 532 nm laser light. The backscattered photons are pre-integrated over 4000 laser pulses (about 2.5 min). Further integration is applied depending on the purpose. The altitude resolution is 50 m. For the calculation of backscatter ratios we use the N_2 vibrational Raman signal at 387 nm as measure of the pure molecular signal. The Raman signal is normalized to the elastic signal in the altitude range of 28.5 to 30.5 km or 17.0 to 20.0 km for the unpolarized or cross-polarized backscatter at 532 nm, respectively. The backscatter ratio is smoothed with a ±10 bin Hanning window.

Most of the soundings in summer 2001 were performed for tropospheric aerosol detection [Schneider and Eixmann, 2002], the others for the examination of noctilucent clouds in the mesosphere [Alpers et al., 2000]. A limited number of observations focus on the UTLS. In this study only the latter can be used for

quantitative studies. The mesospheric studies provide only qualitative information in the lowermost stratosphere because the signal is partly blocked by a chopper, inhibiting quantitative analysis below about 18 km.

The radiosonde data are from the routine operations of the German Weather Service at Lindenberg (52°N, 14°E, ~261 km from the lidar site). Out of the four daily launches we have chosen the midnight launch because it is closest to the time of the lidar soundings. The radiosonde data are available with a height resolution of 50 m, and the temperature error is less than 0.2 K in the region below 20 km. The tropopause is defined as the altitude where the temperature gradient is larger than -2 K/km for at least 2 km.

4.2.2.4 Garmisch Partenkirchen

The aerosol lidar at Garmisch-Partenkirchen (47.5º N, 11.1º E) was built in 1973 and 1974. Quantitative data were first retrieved in 1976. This has yielded one of the longest records of the stratospheric aerosol [Jäger, 2005; Deshler et al., 2006]. In 1990/1991 high-resolution angular scanning was introduced for the investigation of contrails [Freudenthaler et al., 1994], and the ruby laser (694.3 nm) was replaced by a more powerful, frequency-doubled Nd:YAG laser (Quanta Ray, GCR-4). The laser transmits 550 mJ at 532 nm, with a 10-Hz repetition rate, in combination with the original 0.52 m-diameter receiver. The upgraded system subsequently became a primary instrument of the NDACC network.

4.2.2.5 Mauna Loa (JPL)

The Jet Propulsion Laboratory (JPL) lidar at Mauna Loa Observatory (MLO) was installed in 1993. It makes nighttime measurements averaged over 2 hours, usually beginning at the end of astronomical twilight, and 3-4 nights per week on average. While it is primarily an ozone and temperature lidar system for measurements in the upper troposphere and above, good aerosol backscatter

measurements at 355 nm are also obtained. At 355 nm the lidar transmits >120 mJ per pulse at 50 Hz. Backscattered radiation from the atmosphere is collected with a 1 m diameter telescope and for aerosol measurements, the elastic backscatter at 355 nm and the nitrogen Raman scattering at 387 nm are accumulated. The ratio of the 355 nm and 387 nm signals is normalized in a region believed to be aerosol free, typically >30 km, to give the aerosol backscatter ratio. This method, utilizing the nitrogen Raman signal, eliminates the need for a reference density profile from another source, e.g., sonde or model, and provides a more accurate measure of the backscatter ratio.

4.2.2.6 Mauna Loa and Boulder (NOAA GMD)

The National Oceanic and Atmospheric Administratrion (NOAA)/Global Monitoring Division (GMD) has been measuring aerosol backscatter with an Nd:YAG (532 nm, 1064 nm) lidar system since March, 1994 at the MLO. MLO is located at 19.5° N, 155.6° W, 3.4 km above sea level on the north slope of the Mauna Loa volcano on the island of Hawaii and samples both tropical and mid-latitude air depending on season and atmospheric circulation patterns. The lidar also measures water vapor and temperature. A smaller Nd:YAG (532 nm) aerosol system has been operated in Boulder, Colorado (40.0° N, 105.3° W, 1.6 km altitude) since August, 1999. Both systems are operated weekly and are part of the NDACC.

4.2.3 In Situ Size Distributions

In addition to the remote measurements there was one in situ profile measurement with a balloon-borne optical particle counter (OPC) which appears to have sampled the smoke. These OPCs have been flown regularly from Laramie, Wyoming (41ºN, 105ºW) since the early 1970s [Hofmann et al., 1975; Hofmann, 1990; Deshler et al., 2003]. The instrument initially developed by Rosen [1964] was modified in the early 1990s to increase the number of size bins and improve sensitivity [Hofmann and Deshler, 1991]. The instrument is presently capable of

measuring particles between 0.15 and 2.0 μm in 12 radius ranges. Sizing errors are on the order of 10%. Concentration errors are dependent on the square root of the concentration, ranging from ~90 to 10% for concentrations ranging from 0.001 to 0.1 cm^{-3} [Deshler et al., 2003]. Data from these measurements are publicly available through the World Wide Web (http://www-das.uwyo.edu/~deshler/).

4.2.4 Tropopause Height

Tropopause-height data used herein come either from radiosonde reports or determined by the dynamical definition, that being the height of a prescribed potential vorticity (pv) surface. The most frequently chosen pv values for the mid- and high-latitude tropopause are between 1.5 and 2.0 pvu (potential vorticity units, 1 pvu = 10^{-6} K m^2 kg^{-1} s^{-1}; see [Holton et al., 1995, Beekmann et al., 1997]. We chose 3 pvu as a buffer to avoid troposphere overlap. For the tropopause height calculation we use the daily (12 UTC) UK Met Office analyses [Swinbank and O'Neill, 1994] of temperature, wind, and geopotential height collocated both in time and space to the profile.

4.3 Results

This paper synthesizes a large variety of measurement types, locations, and frequency on a seasonal time scale. Hence we introduce Figure 4.1, an overview of the measurement instruments, date, and latitude discussed in detail next. Figure 4.1 shows POAM III data as vertical bars whose length is scaled by stratospheric AOD (details in 4.3.1.2). All other instruments have individual symbols (see figure caption for details), which are filled in black if a stratospheric aerosol layer was measured. For SAGE II, a circle represents a full day of profiles; filled if any profiles had an aerosol layer.

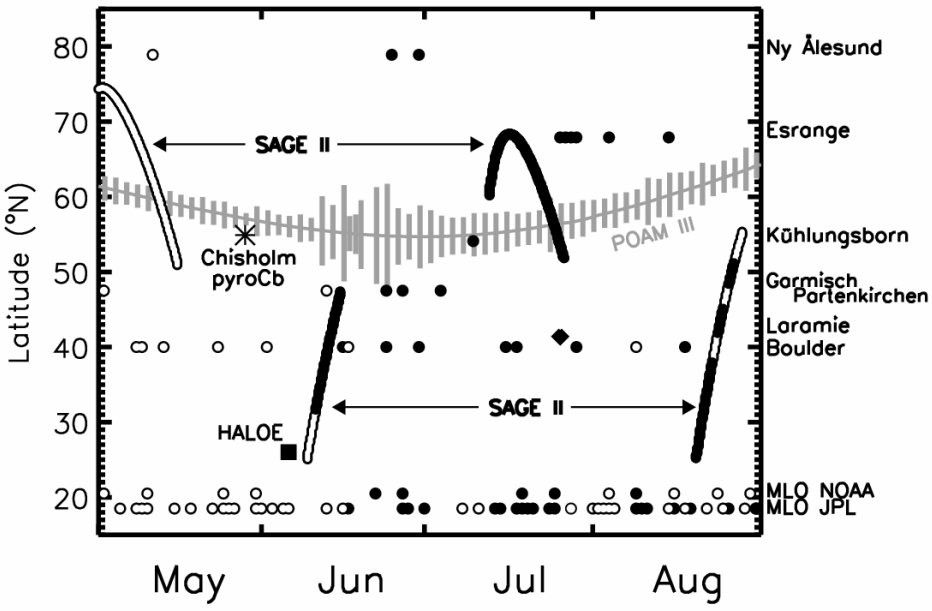

Figure 4.1. Location and date of the observations reported in this paper, expressed in time (abscissa) and latitude (ordinate). The Chisholm pyroCb is marked by an asterisk. POAM III data are represented as gray vertical bars straddling the POAM measurement latitude (gray line connecting the bars); bar length proportional to stratospheric AOD (see text for details). SAGE II symbols are circles, one per day, open for dates with no stratospheric aerosol layers, filled black if one or more layers detected. Lidar symbols are circles, open for no-aerosol-layer, filled black for layer observations. HALOE symbol: square. Laramie in situ symbol: diamond. Lidar-location names at approximate instrument latitude along the right axis (Mauna Loa lidars separated for clarity).

Figure 4.1 shows that this assemblage of instruments gives an effective seasonal sampling of the stratosphere from the Arctic to the tropics. Together they also offer a sampling frequency that permits an assessment of intraseasonal trends throughout much of this latitude range. The Chisholm latitude (54°N) and pyroCb date (28 May) are also indicated on Figure 4.1. It is apparent that there were no stratospheric aerosol enhancements in the month before the pyroCb, and many after. Next we present the details.

4.3.1 Satellite Solar Occultation (SO) Observations

4.3.1.1 Individual SO Profiles

In this section we present four individual SO extinction profiles chosen to reveal important characteristics of the Chisholm pyroCb stratospheric plume. In Chapter 3 it was determined that the Chisholm smoke plume the morning after the pyroCb—29 May 2001—was an optically opaque cloud that reached 15 km, ~4-5 km above the local tropopause. Rosenfeld et al. [2007] showed that in the active convection the tops of the smoke-contaminated anvil were 1-2 km above the local temperature minimum (T_{min}), the top of the tropopause region. Here we attempt to reconcile such values with the first two unambiguous stratospheric aerosol layers after 29 May, and a third layer observed two weeks after the pyroCb.

On 1 June POAM III made a measurement over Quebec, shown in Figure 4.2. The figure shows both the 1018 nm aerosol extinction ratio (normalized by Rayleigh extinction) and color ratio (the ratio of the 442 nm to 1018 nm extinctions). These are both shown in the context of the collocated temperature profile and tropopause altitude. The extinction ratio peaks at 12 km at three times Rayleigh, distinctly above background for that altitude. The tropopause is at roughly 9.5 km and the T_{min} is ~11 km. Thus this layer is unambiguously in the lowermost stratosphere (the potential temperature at 12 km was 355 K). The color ratio profile implies differences in particle size between the aerosol layer and the unperturbed altitudes above. In the limit, a particle population generally larger than 1018 nm would give no wavelength dependence—a color ratio of 1. We see that the color ratio decreases between the unenhanced altitudes and those with the aerosol layer. However, the color ratio even at the peak is considerably larger than one. Thus, the aerosol layer is composed of particles generally smaller than 1 μm. A non-negligible wavelength dependence is found in the preponderance of the POAM and SAGE smoke layers.

Figure 4.2. POAM III 1018 nm extinction ratio profile (black line) at 56.5ºN, 71.8ºW on 1 June 2001. POAM III color ratio (442 nm/1018 nm), gray line. Collocated temperature profile, black dashed line. Collocated tropopause height; horizontal dotted line.

We used HYSPLIT [Draxler and Hess, 1998] to evaluate the source of this aerosol layer. Figure 4.3 shows a back trajectory started at the POAM layer at the measurement time of 01 UTC. The trajectory passes over the Chisholm area at around the time of the pyroCb (~02 UTC 29 May). Moreover it traces a path consistent with the early evolution of the Chisholm plume as described in Chapter 3. Hence we believe the POAM aerosol enhancement in Figure 4.2 is smoke from the Chisholm pyroCb.

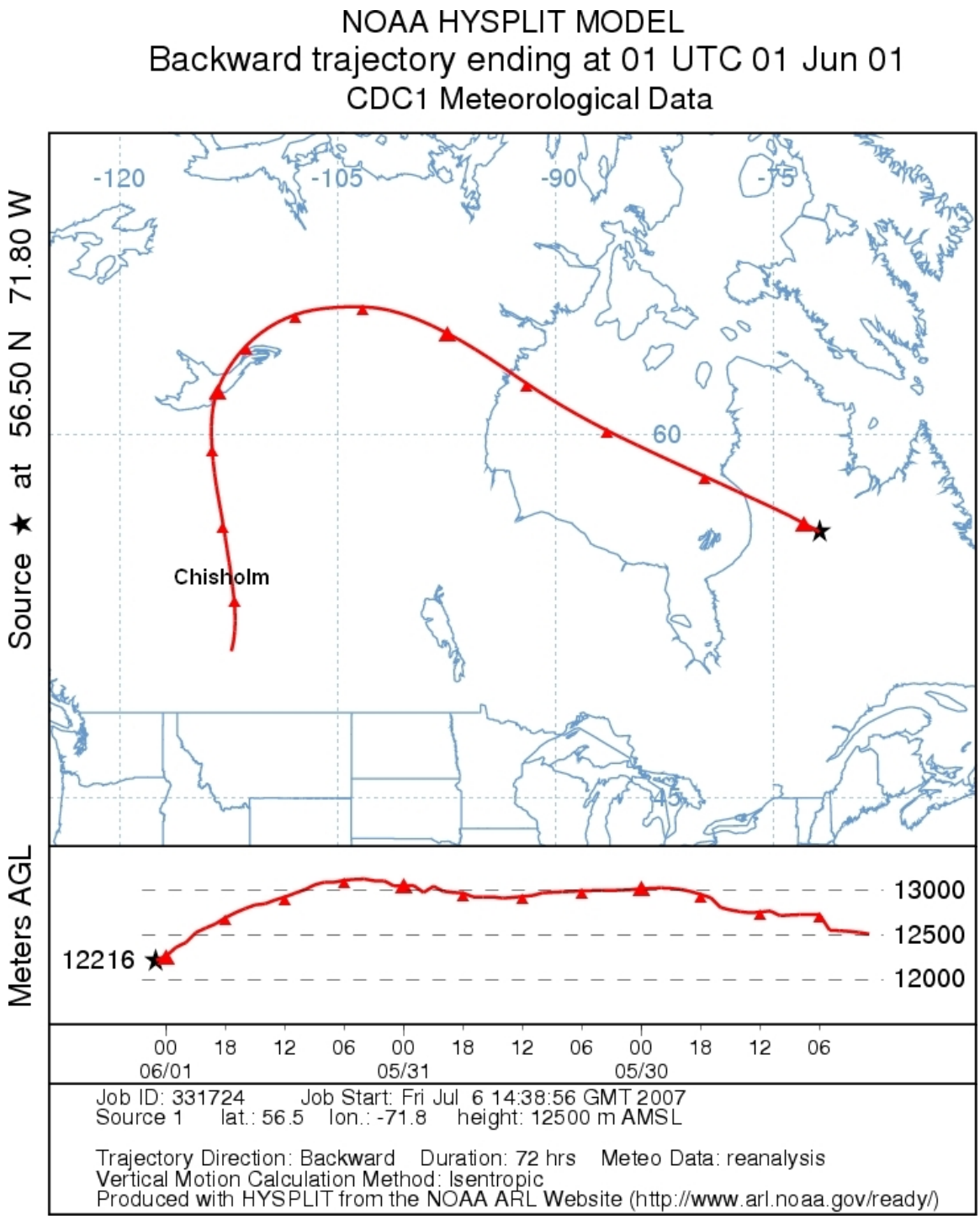

Figure 4.3. HYSPLIT backward trajectories initiated at the POAM III 1 June aerosol profile location (Figure 4.2). Length of trajectory is 72 hours, roughly the time between the POAM measurement and the Chisholm pyroCb. Trajectory-start altitude is 12.5 km. PyroCb location is near the annotation "Chisholm."

HALOE's measurement pattern in June 2001 began with sunset occultations on 5 June at about 30°N and subsequent southward progression such that by 8 June they passed 15°N and by 11 June passed south of the Equator. In Figure 4.4 we see an enhancement of extinction on 5 June in HALOE's 2.45 μm channel in a profile over the sub-tropical Atlantic. This was the only sunset profile showing dramatically larger extinction in the lowermost stratosphere in early June. The layer of enhanced extinction extends from 1 to 4 km above the local tropopause. In this vicinity of the Atlantic (26°N, 45°W), we showed in Chapter 3 that the Chisholm plume was plainly evident in terms of the progression of the TOMS AI enhancements—the plume had initially passed north over north-central Canada, then south over Hudson Bay into the eastern US by 1 June. In the four days thereafter part of the plume wound north toward Greenland and then southeast toward Europe while another portion moved into and apparently swirled in the area very close to the HALOE observation.

Figure 4.4. HALOE extinction profile, at 26.3ºN, 44.6ºW on 5 June 2001. Back line is the 2.45 nm extinction. Gray line is the color ratio (2.45 nm/5.26 nm). Vertical, gray dashed line at color ratio = 1 for reference. Collocated tropopause is shown by horizontal dashed line.

Also in Figure 4.4 is a plot of color ratio using HALOE's 2.45 μm and 5.26 μm channels. Here we see color ratios much larger than 1 in the layer, peaking at nearly 4. The values of the 2.45 μm /5.26 μm color ratios of 3 to 4 from the HALOE measurements above the tropopause are incompatible with those of normal sulfuric acid stratospheric aerosols. Model calculations by Hervig et al. [1998] show that for typical background stratospheric aerosols the color ratio would be about 0.5 or less (see their Figure 2), which is consistent with what is observed above the smoke layer. For typical volcanically enhanced aerosols the color ratio would be about 1.0 to 2.0. Even the maximum color ratio Hervig et al. find (2.5) for particle radii of about 1.2 μm, is still less than the measured values of 3 to 4. Hence we conclude that this substantial extinction enhancement with a unique HALOE color ratio is part of the Chisholm smoke plume.

In the first week after injection the Chisholm pyroCb plume (Figure 3.15) dispersed in such a way that the 14-15 daily Northern Hemisphere measurements from each SO instrument, separated by the typical 25° in longitude such as POAM's and HALOE's, had few opportunities to intercept. The two profiles discussed above were the best/earliest examples of an indisputable aerosol layer well above the tropopause in the first week after the pyroCb. There were no such stratospheric aerosol layers in POAM and HALOE earlier in 2001.

By 11 June the daily frequency of stratospheric smoke layers as observed by SO instruments had begun increasing. On this date SAGE II (the June 2001 latitudinal measurement progression of which was such that it swept north to midlatitudes by 10 June) had four consecutive orbits of enhanced stratospheric aerosols over East Asia and the western Pacific, as seen on the map in Figure 4.5. Note also the positions of the POAM profile measurements and aerosol-layer detections extending across most of Russia marked on the same map. The map is highly suggestive of a plume that was broadening both zonally and meridionally. Figure 4.6 displays a SAGE aerosol profile on 11 June with an extinction enhancement--greater than 40 times Rayleigh--in a layer well above the tropopause.

This layer also exhibits strong wavelength dependence. Thus, like the POAM layer on 1 June, these particles have a characteristic radius less than 1 μm.

Figure 4.5. Polar map projection showing location of POAM III (red) and SAGE II (blue) measurements on 11 June 2001. Dots show where stratospheric aerosol enhancements were detected; plus signs identify unenhanced profiles.

Figure 4.6. SAGE II 1020 nm extinction-ratio profile (black line) at 38.6ºN, 113.6ºE on 11 June 2001. SAGE II color ratio (525 nm/1020 nm), gray line. Vertical, gray dashed line at color ratio = 1 for reference. Collocated tropopause height; horizontal dotted line.

Over the course of the northern spring/summer of 2001 there were over one hundred POAM, SAGE, and HALOE profiles with lower stratospheric aerosol enhancements. One of the most remarkable of these is the POAM profile on 9 July at 54°N, 90°W shown in Figure 4.7. The aerosol-layer's peak extinction was at an altitude of 18 km, approximately 9.5 km above the tropopause. This aerosol layer was one of four POAM aerosol layers observed at 17-18 km, all of which occurred in July. These represent the highest Chisholm smoke layers observed by the instruments discussed herein, and higher in potential temperature than any observed after the pyroCbs documented by Fromm et al. [2005 and 2006]. It is outside the scope of this paper to analyze the Chisholm plume's smoke-layer altitude; however it is an important aspect of the pyroCb phenomenon that calls for future exploration.

Figure 4.7. POAM III 1018 nm extinction ratio (1018 nm total extinction/Rayleigh) at 54.4ºN, 90.0ºW on 9 July 2001. Collocated tropopause is shown by horizontal dashed line.

4.3.1.2 Analysis of POAM, SAGE, and TOMS

In the northern spring/summer of 2001 there were many POAM and SAGE profiles with stratospheric aerosol layers. The abundance of observations lends itself to statistical organization of these data.

As mentioned in section 2.1, POAM made its measurements in a small latitude range (54° to 65° N). Every other day POAM made a full hemispheric complement (~14) of profiles. Because the vertical aerosol distribution was highly variable the 1018 nm extinction measurements are expressed in terms of lower stratospheric AOD by integrating between 30 km and the lowest altitude bin 2 km above the tropopause. A time series of the zonal average AOD from 1 May, before the Chisholm pyroCb, to the end of August is shown in Figure 4.8. The daily maximum TOMS AI within the hemispheric belt bounded by latitudes 45° and 75°N, encompassing the boreal forest zone, is also shown in Figure 4.8.

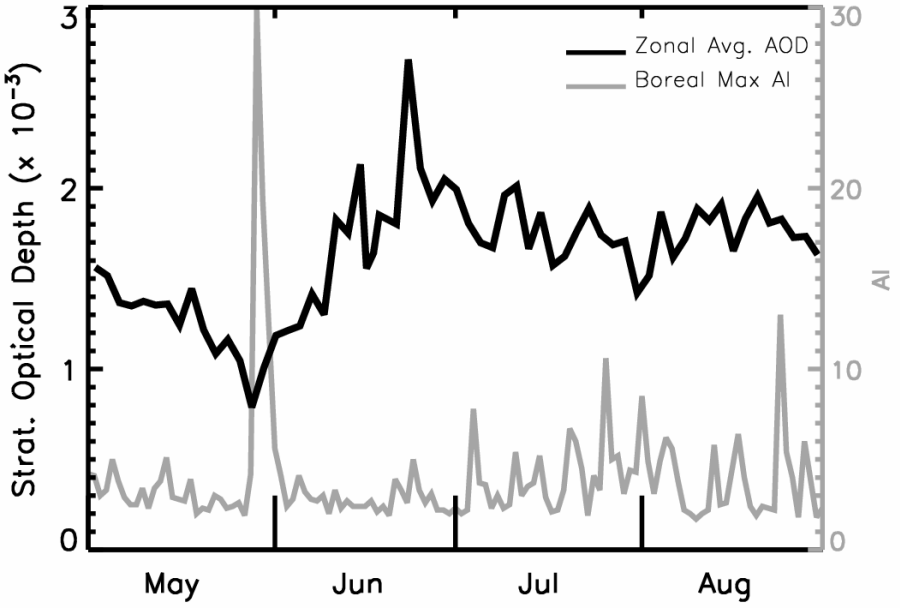

Figure 4.8. Daily/zonal average 1018 nm POAM III AOD, May-August, 2001, black line. Optical depth calculated by summing 1018 nm extinction from tropopause+2 km to 30 km. Gray line: daily maximum TOMS aerosol index north of 45ºN.

The AI pattern in Figure 4.8 has one dominant feature, the large spike on 29 May, the day after the Chisholm pyroCb. The maximum AI on this day was the largest in the entire span of Nimbus VII and Earth Probe TOMS between 1979 and 2004. As discussed in Chapter 3, extreme AI such as this indicates strongly absorbing, elevated (i.e., UTLS) and optically dense plumes. The summer of 2001 contained no other AI plume nearly as extreme as that of 29 May. Figure 4.8 shows that in July and August the daily maximum AI did increase on several days to values well above the "background," for instance the double-digit AI plume on 25 August. Thus, there may have been other pyroconvective activity at those times, but between May and August 2001 the AI from the Chisholm pyroCb is over twice as large as any other. Thus the Chisholm pyroCb was 1) a singularly extreme event and 2) the only extreme smoke injection until at least late July or August.

The POAM zonal average AOD before 29 May decreases slightly, reaching a minimum in late May. Soon after the pyroCb, AOD started increasing and by 23 June was roughly double the pre-pyroCb values. After 23 June the zonal average AOD declines somewhat, but is still greater at the end of the time series than prior to the Chisholm blowup. The doubling of the zonal average AOD is roughly equivalent to the AOD increase reported by Fromm et al., [2006] in the case of the Canberra Australia pyroCb, and roughly half of the AOD jump reported by Fromm et al. [2000 and 2005] in the case of the Norman Wells NT pyroCb of August 1998. These three cases are also those for which the TOMS AI plume peaked at the largest values in the TOMS record. Considering the AI pattern in Figure 4.8, the POAM AOD perturbation between June and August is most likely attributable exclusively to the Chisholm pyroCb.

The inclined SAGE II orbit results in rapidly changing measurement latitudes relative to POAM. In the May-August 2001 time frame SAGE explored the mid and high northern latitudes in several discrete intervals, each lasting a few weeks. For this reason SAGE 1020 nm extinction ratio (total/Rayleigh) profiles are converted to a tropopause-relative altitude grid before computing range, mean, and median for those measurements north of 25°N. In Figure 4.9 the May time frame (before the Chisholm impact) is illustrated with the range shaded, and the median and mean overplotted. This unperturbed time frame is characterized by extinction ratio between about 1.8 at 3 km above the tropopause to 2.1 10 km above. In the entire vertical domain of Figure 4.9 the May mean and median are the same indicating the extinction ratio distribution is normal. In June the mean extinction ratio is larger than for May from bottom to top in Figure 4.9. From 7 to 10 km above the tropopause, the June mean and median are roughly equal; for lower altitudes, the mean departs considerably from the median (indicating a few extreme values) and ranges far outside the May maximum. In July the mean and median extinction ratio are nearly identical to May from 7-10 km above the tropopause. Below that the July mean and median diverge somewhat, but are both greater than the May maximum between 3 and 5 km above the tropopause. The August mean and median are roughly equal throughout the

domain, mimicking the June values above 7km above the tropopause. In the lower half, the August values appear to be relaxing back from the July values, but are still far larger than both May and June means.

Figure 4.9. SAGE II 1 micron extinction ratio statistics for mid-latitude spring/summer 2001 profiles. The bottom of this tropopause-relative ordinate is +3 km. May 2001 statistics include the range (shaded), median (white line) and average (black dashed line). Other months have only median (solid) and average (dashed). June (red); July (blue); August (green).

The SAGE variations in Figure 4.9 are a function of the specific latitude ranges sampled (see Figure 4.1) and the impact of the Chisholm smoke. Above 7 km with respect to the tropopause the extinction ratio distributions are exclusively normal. The shifts in these values from month to month are the result of variations in the sampling latitude. From 3-6 km above the tropopause the SAGE extinctions are strongly perturbed in June-August. The perturbation is spatially concentrated in June, indicated by the large mean-median difference. This decrease of this differential in July and August suggests that the enhanced aerosol burden is spread hemispherically.

4.3.2 Lidar Observations of the Chisholm Smoke

In addition POAM, SAGE, and HALOE, seven ground-based lidars contributed measurements of the Chisholm plume. The lidar locations, wavelengths, and measurement dates are listed in Table 4.1. The subsections below are organized by instrument, in the order of decreasing latitude.

4.3.2.1 Ny Ålesund (79°N)

Between May and August 2001 the lidar at Ny Ålesund was operated when meteorological conditions permitted. On 24 and 29 June anomalous stratospheric enhancements in backscatter and depolarization were recorded. In Figure 4.10 we show time-height curtain plots of backscatter coefficient and volume depolarization. The aerosol enhancements are manifested as small yet persistent increases in both backscatter and depolarization. On 24 June there is primarily a single aerosol layer between roughly 12.5 and 13 km altitude, 2 km above the tropopause, lasting the entire 10 hours of measurements. On 29 June, the tropopause is at 9.5 km and above it are three aerosol layers. These layers are somewhat more highly backscattering and depolarizing than the 24 June layer. Two layers on 29 June, at about 12 and 13 km, persisted for the entire 12-hour measurement span. A higher layer, at about 14 km (4.5 km above the tropopause) appears midway during the measurement time and lasted over 9 hours. All of these backscattering layers on both dates exhibited depolarization, indicating a consistent composition of non-spherical (solid) particles. This same combination is what led Siebert et al. [2000] to conclude the existence of a smoke layer with solid particulates (possibly soot) over Scandinavia in July 1998. The persistence of these layers indicates that the aerosol enhancement is a large, quasi-continuous feature on both dates. The observations five days apart suggest that the aerosols being transported in the high Arctic one month after Chisholm were broad in horizontal scope. It was at this time (late June) that the POAM zonal average AOD reached its peak.

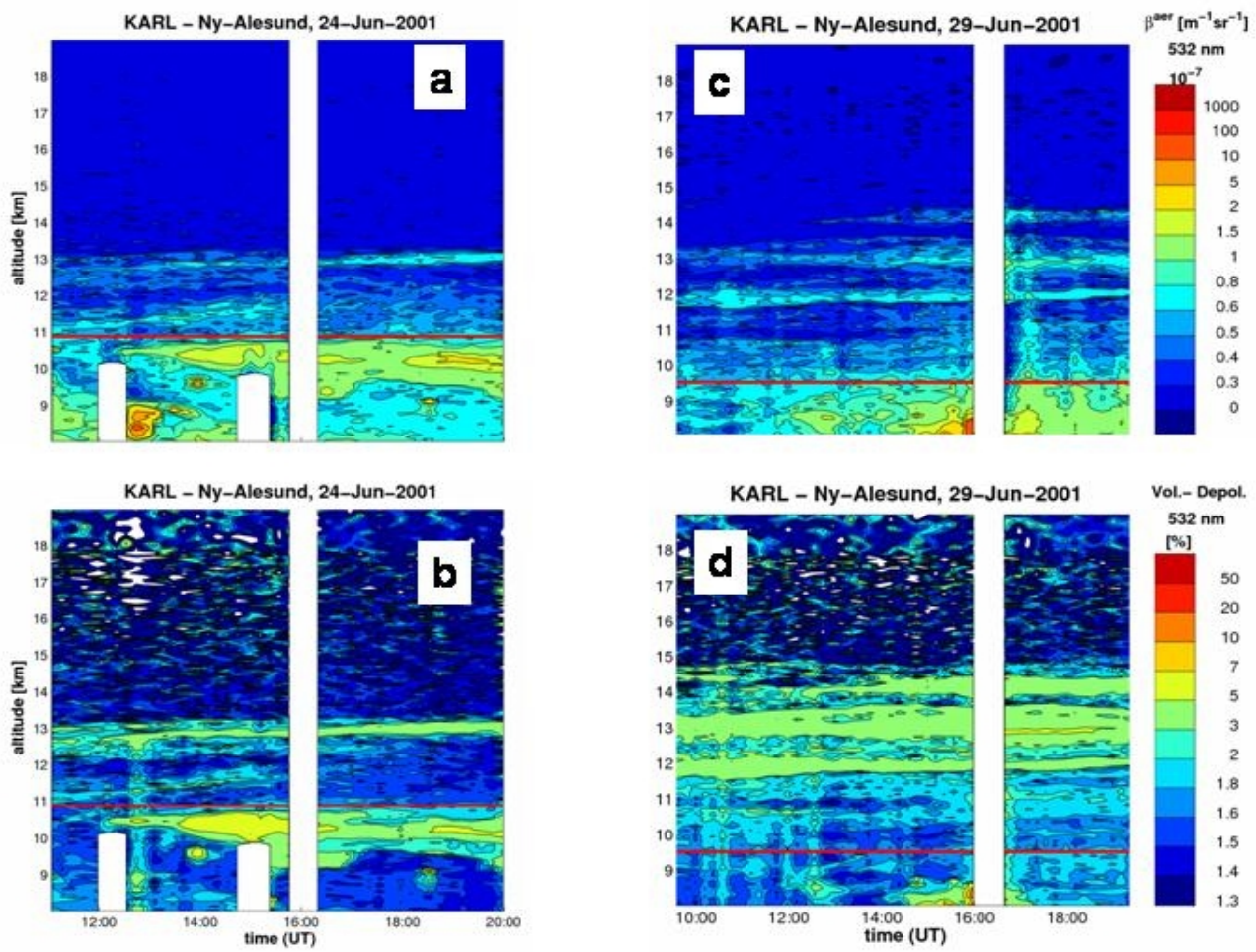

Figure 4.10. Ny Ålesund lidar time-height curtain of 532 nm backscatter coefficient (a, c) and volume depolarization, in percent (b and d) for 24 June (a, b) and 29 June (c, d) 2001. Thin red line is the tropopause altitude.

In Figure 4.11 we display the depolarization data on each date as a single profile, and show an accompanying temperature profile from a radiosonde launched at the same location and time as the lidar measurement. There is a generally positive correlation between temperature and the aerosol abundance in the neighborhood of the layers. This correlation, which we characterize as a "warm" layer coincident with the aerosol enhancement may suggest that the solid aerosols are imbedded in a layer which has been radiatively modified by the aerosols. The temperature sounding is an independent measurement with high vertical resolution, but spatially separated by the drift of a balloon. Considering the deduced large horizontal extent of the persistent layers, it is likely that the radiosonde passed through the aerosol layer. Thus,

although we have only two measurements of locally "warm" aerosol layers, we can state that: 1) there is no inherent measurement contamination, 2) the lidar and radiosonde were likely sampling exactly the same air mass, and 3) an aged layer of absorbing aerosols such as smoke would reasonably have such a temperature impact.

Figure 4.11. Depolarization profiles for a segment of the data shown in Figure 4.10. Panel a is for 24 June, b for 29 June. Black lines are the lidar data. Gray lines show radiosonde temperature (K). Depolarization scale is at bottom; temperature scale along the top. The vertical dashed line is a nominal, background depolarization value. The gray horizontal line is the altitude of the temperature minimum.

The aerosol feature on 29 June in Figure 4.11 is a double-peaked. The coincident radiosonde gives evidence of localized "warming" that matched remarkably well with the two distinct aerosol enhancements. The two local maxima in temperature at the altitudes of peak depolarization are indeed small, however they are imbedded in a larger surrounding envelope of greater temperature with respect to the levels immediately above and below the two-layer aerosol enhancement.

4.3.2.2 Esrange (68°N)

The Esrange lidar operated on six dates from July 25 to August 14. Enhanced aerosols in the lower stratosphere, which might be smoke particles, were measured on each occasion (Figure 4.12). Figure 4.12 a-d reveals that aerosol enhancements were detected at Esrange on four consecutive days. This daily detection of enhanced stratospheric aerosols is suggestive of a quasi-continuous feature. Moreover, Figure 4.12e-f shows that one week later, on 3 August and again on 14 August depolarizing layers were observed. Figure 4.8 indicates that in late July the zonal average lower stratospheric AOD (two months after Chisholm) was still elevated with respect to pre-Chisholm. Thus, the POAM and Esrange lidar data are giving distinct yet consistent indications of a hemispheric aerosol perturbation.

The depolarizing signal indicates solid aerosols, which makes them compatible with smoke and the observations made at Ny Ålesund. Below about 14 km altitude down to the tropopause aerosols are present on each is measurement day and show little fluctuation with altitude and a cross-polarized backscatter ratio of 1.5 to 2. On the first four measurement occasions, 25-28 July there are one or two narrow layers (600 m thick) in the altitude range 15 to 17 km. These "top-layers" appear to be "cloud-like", i.e., they existed only for a few days, while the "bottom" layer from 14 km to the tropopause was present for three weeks as if the entire lowermost stratosphere was filled with solid particulates.

Figure 4.12. Lidar data from the Esrange. Six panels, one for each measurement date. Top: four profiles from July 2001; bottom: two August 2001 profiles. Black line and symbols, parallel polarization 532 nm backscatter ratio. Red lines and symbols, perpendicular polarization backscatter ratio. Green line is radiosonde temperature (K) from Bodø, Norway (67.3°N, 14.7°E, ~279 km west of Esrange) at the measurement time closest to the lidar data. Temperature scale, along the top axis, color coded with the temperature plot.

Figure 4.12 also shows temperature profiles from the radiosonde location closest to the Esrange, at Bodø (67.2°N, 14.4°E, 279 km from Esrange). These temperature measurements are shown to support the tropopause determination, and to qualitatively show a thermal character of the air mass in which the aerosol layers were observed. We cannot draw similarly strong conclusions here as we did with Ny Ålesund because of the much greater radiosonde-lidar distance here and the variable time difference in measurements. However, the temperature profiles show that the aerosol enhancements are above the cold-point tropopause. Moreover, on 4 of the 6 dates shown, 25-27 July and 14 August there is some indication of locally warmer air in proximity to the aerosol layers.

4.3.2.3 Kühlungsborn (54°N)

One quantitative measurement was made by the Kühlungsborn lidar in summer 2001, on 9 July (Figure 4.13). The profile shows little or no enhancement in backscatter in the un-polarized channel, but a substantial increase in the perpendicularly polarized channel. Here the enhancement occupies altitudes from above the local T_{min} (recorded by the Lindenberg radiosonde launched at 52°N, 14°E, 261 km from the lidar) to 16 km, 5 km above the T_{min}. The increase in cross-polarized backscatter indicates the presence of non-spherical particles. The accompanying temperature measurement, while not truly coincident, is close in both time and space to the lidar measurement. As with the Ny Ålesund observations, there is a correlation of the aerosol layer with an apparent "warm" layer that, together with the findings discussed earlier may be consistent with air radiatively impacted by absorbing smoke aerosols.

Figure 4.13. Lidar data from Kühlungsborn. Black solid line, backscatter ratio at 532 nm (unpolarized). Black dashed line, perpendicular polarization backscatter ratio. Gray line is radiosonde temperature (°C) from Lindenberg (52.2°N, 14.1°E, ~261 km from Kühlungsborn) at the measurement time closest to the lidar data. Temperature scale, along the top axis, gray shaded as is the temperature plot.

4.3.2.4 Garmisch Partenkirchen (47°N)

Lidar operation in spring 2001 was infrequent, and interrupted after 3 July for a field campaign. Four measurements were made in June and July 2001. The first one on 12 June (not shown) does not show any sign of a plume above the tropopause. Figure 4.14 shows observations on 23 and 26 June, and 3 July, of aerosol layers in the lowermost stratosphere at Garmisch Partenkirchen. The tropopause level is taken from the Munich radiosonde which is launched about 100 km to the north at 0 and 12 UTC. On 23 June there is a sharp enhancement, approximately 2 km thick, with a backscattering peak 2 km above the tropopause (z=13.8 km). On 26 June there is a multi-layer enhancement 1-4 km above the tropopause (between 13 and 16 km). One week later, on 3 July, a relatively broad layer resides about 3 km above the tropopause (centered at 14.6 km), and the layer extends to 17 km.

Figure 4.14. Three lidar profiles from Garmisch Partenkirchen, and radiosonde temperature profiles from Munich (~90 km from the lidar). Vertical axis (in km) is a tropopause relative grid. Black line, parallel polarization 532 nm backscatter ratio; gray line is temperature (°C, scale on top and color coded to match plot). Panels are for 23, 26 June, and 3 July. Radiosonde measurement is from the 00 UTC ascent closest to lidar measurement.

The temperature profiles reinforce the pattern in the layer observations from Ny Ålesund, Esrange, and Kühlungsborn –localized "warm" layers in proximity to the aerosol enhancements. Once again, we can only conclude that there is an apparent correlation, but the weight of the similar findings at four sites and ten

occasions of aerosol layers provide sufficient motivation for a more systematic and exhaustive analysis of coincident smoke and UTLS temperature observations in future work.

The 23 and 26 June measurements were made within three days of the two layer observations at Ny Ålesund. At this time POAM was recording its maximum zonal mean optical depth, at ~54°N. Thus, it is evident that by this time the stratospheric Chisholm smoke was distributed around the hemisphere zonally and meridionally between at least 47°-79°N.

4.3.2.5 Boulder (40°N)

Measurements by the lidar in Boulder in 2001 were taken on 14 dates scattered between May and August (Table 4.1). Backscatter ratio profiles, on a tropopause-relative altitude grid, are shown in Figure 4.15. The tropopause height is from the standard World Meteorological Organization (WMO) definition for Denver radiosondes (~30 km south of Boulder) launched at ~00 UTC on measurement dates. For each month we color code the profile as a day-of-month scaling—violet on the rainbow scale for first, red for last. The four May profiles (Figure 4.15a) all appear similar, with gradual, monotonic increases from tropopause+10 km downward to tropopause+2 km, and a more rapid increase from there to the tropopause. There is no evidence in May of an aerosol layer above the tropopause. Stratospheric aerosol layers over Boulder began showing up sporadically in mid-June 2001. On 1 and 16 June (Figure 4.15b) two profiles have an appearance similar to the May profiles, but on 15, 23, and 29 June unambiguous aerosol enhancements are manifest. The 15 June profile has broad, multi-layer backscatter enhancements from the tropopause to tropopause+4 km. On 23 June there are two distinct aerosol layers 1 and 3 km above the tropopause. The 29 June profile shows aerosol enhancements in a single, thick layer between 1 and 3 km above the tropopause.

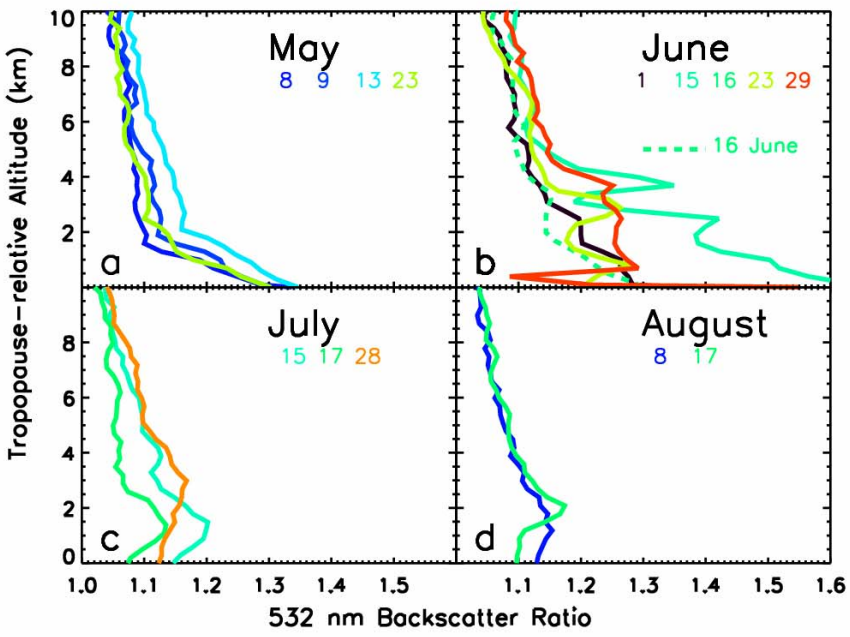

Figure 4.15. Lidar data from Boulder. Panels a-d are for May-August, respectively. Backscatter ratio profiles at 532 nm are color coded to distinguish day of month. A rainbow color scale is used, violet for first day of month, red for last. Vertical axis (in km) is a tropopause relative grid. The profile in (b) for 16 June is plotted as a dashed line to distinguish it from the 15 June plot.

The 5 profiles in July and August (Figure 4.15c and d) each show local backscatter maxima 1-3 km above the tropopause. None of the backscatter ratios in the layer peak were as large as the layers observed in June. The Boulder observations in July and August are suggestive of a frequent but decaying aerosol layer just above the tropopause, a pattern similar to that observed at Esrange.

4.3.2.6 Mauna Loa (20°N)

Two lidar systems operated at Mauna Loa. Because of differences in wavelength and ancillary data available, the measurements are displayed separately. Figure 4.16 (4.17) gives the JPL (NOAA GMD) lidar results. The profiles are color coded as for the Boulder measurements. The JPL lidar data files in the NDACC database include temperature and pressure, allowing the calculation of potential

temperature (θ) for the vertical coordinate. θ in Figure 4.16 and altitude for the NOAA GMD data in Figure 4.17 give alternate perspectives on the height of layer features observed at essentially the same location. Between the two instruments there are a total of 61 profiles between May and August 2001, enough to gain a qualitative sense of temporal changes in frequency of anomalous features. Figures 4.16 and 4.17 also show, in a single gray shade, all the profiles for May-August 2000, to give a basis with which to compare 2001 features.

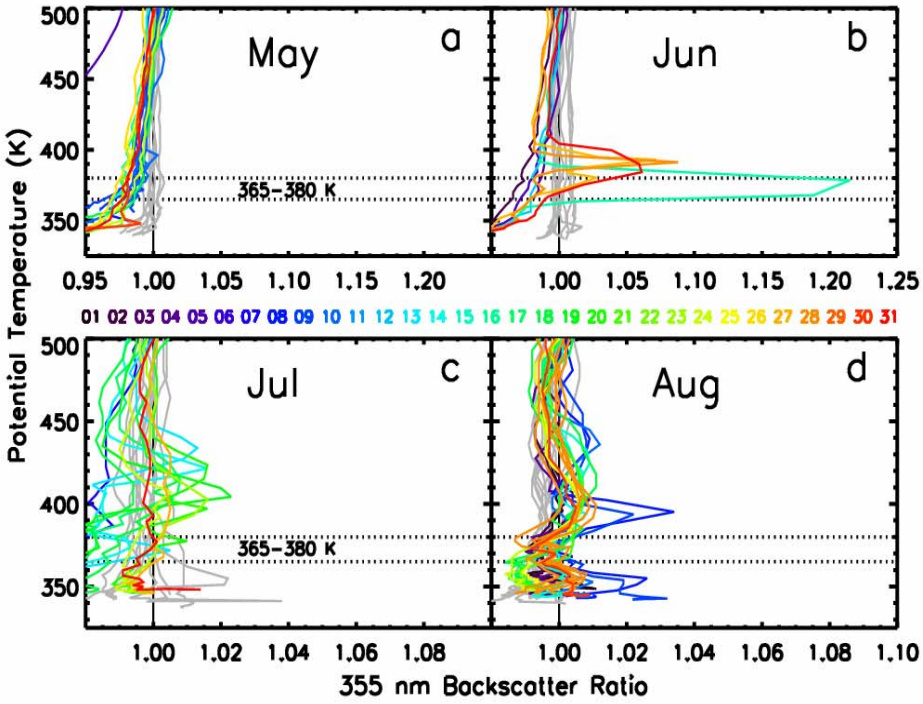

Figure 4.16. JPL lidar data from Mauna Loa. Panels a-d are for May-August, respectively. Backscatter ratio profiles at 355 nm are color coded to distinguish day of month, using the rainbow color, violet for first day of month, red for last (see enumeration between upper and lower panels). Profiles for the same month of 2000 are plotted as gray lines. Vertical axis is potential temperature (K). Horizontal dashed lines at 365 and 380 K bracket the canonical lowermost stratosphere regime. Note the abscissa range for May and June is 0.9-1.25, whereas the July and August range is 0.95-1.10.

First we establish the baseline. In Figure 4.16 the gray profiles of May 2000 and the colored profiles of May 2001 show no enhancements in backscatter ratio between 350 and 500 K, which for Mauna Loa includes the tropical tropopause region and the stratosphere "overworld" [Holton et al., 1995], the regime that anywhere on the globe is considered to be above the tropopause region. Although our understanding of the boundaries and transitions in the tropical troposphere/stratosphere interface is still being refined, there is no debate that θ>400K is exclusively in the province of the stratosphere overworld. It is evident from the four panels of Figure 4.16 that there were no aerosol enhancements in 2000 at θ>400K; furthermore, at θ<380K, there were no enhancements in May, June, and August and at most only modest increases in two July profiles. We also evaluated the 1999 JPL lidar profiles (not shown) and found that, like 2000, there were no aerosol enhancements between May and August.

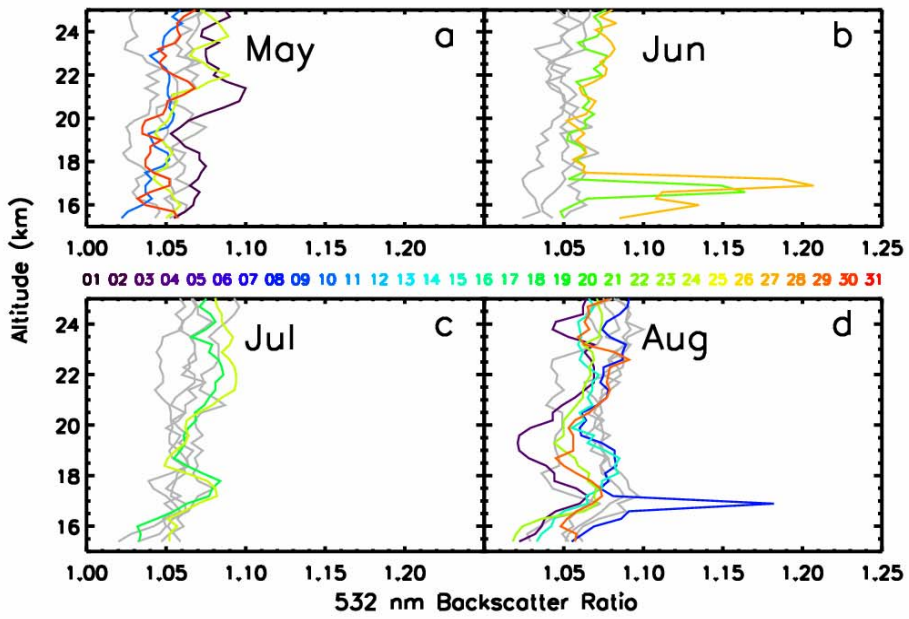

Figure 4.17. NOAA GMD lidar data from Mauna Loa. Panels a-d are for May-August, respectively. Backscatter ratio profiles at 532 nm are color coded as described for Figure 4.16. Profiles for the same month of 2000 are plotted as gray lines. Vertical axis is altitude (km).

The baseline picture of May 2000/2001 and June-August 2000 is in stark contrast to the observations in both instruments after May 2001. Figure 4.16b and 4.17b show that in June 2001, distinctive layer enhancements begin appearing in both the JPL and NOAA GMD measurements. The layers reside in the θ range 365-400K and the height range 15.5-17.5 km. There were no NOAA GMD measurements in the first half of June, but there were five JPL lidar profiles between 2 and 15 June that exhibited no layers. From 16-30 June every NOAA GMD and JPL profile contains an aerosol layer in the lowermost stratosphere. Notably, there was an aerosol layer detected on 26 June (Figure 4.16b), the same day that the Garmisch Partenkirchen lidar detected a stratospheric layer (and between observations at Ny Ålesund on 24 and 29 June). Thus, on or within a few days in late June 2001, anomalous aerosol in the lower stratosphere was spread from the tropics to the high Arctic.

For July and August, the panels (c and d) of Figure 4.16 have a smaller abscissa range than for Figure 4.16 a and b—the layer enhancements trended to smaller peak values. The two July 2001 NOAA GMD profiles (Figure 4.17c) have a small enhancement at about 17 km. The JPL lidar, with measurements between 7 and 31 July (Figure 4.16c), exhibited layers on the majority of measurement days, some extending to θ=430K.

In early August both instruments captured a relatively sharp layer at about 400K (JPL) and 17 km (NOAA GMD). At that same time the JPL profiles also exhibited a second, smoother layer peak at about 440-450K. This peak does not appear in the NOAA GMD measurements. As in July, the August JPL lidar profiles are enhanced somewhere in the lower stratosphere on a large majority of the days of measurement. There appears to be a systematic decrease of top-layer altitude (and to a lesser extent, strength as manifested by the peak backscatter) with day of month—from roughly 440 to 400K.

The two Mauna Loa lidars operated with sufficient frequency in the summers of 2000 and 2001 to conclude that there was a distinctive perturbation in the aerosol profile at this tropical location after the Chisholm pyroCb. The perturbation was first detected in mid-June, and was a dominant feature through August. The onset of this aerosol perturbation was about 2.5 weeks after the pyroCb. To determine if it is reasonable for the Chisholm plume to have arrived at Mauna Loa by in mid-June, we ran HYSPLIT forward trajectories (not shown) from the four SAGE II layers at 38°N shown in Figure 4.5, out to 16 June, when the first Mauna Loa layers were detected. Two of the four trajectories showed clearly that air-flow from the SAGE point crossed the Mauna Loa latitude. Thus, we consider it reasonable that: 1) the Chisholm plume in midlatitudes was transported into the tropical regime, 2) the arrival time at Mauna Loa is consistent with other layer profiles and the ambient meteorology, and 3) perhaps the Mauna Loa observations capture part of the leading edge of the Chisholm plume on its first sweep around the globe after the late-May injection.

4.3.3 In Situ Observations of the Chisholm Smoke at Laramie (41ºN)

In situ size-resolved aerosol concentration measurements above Laramie on 25 July 2001 may have also captured aerosol from the Chisholm pyroCb, after at least one circumnavigation. The aerosol appeared as concentration enhancements, by factors of 2 to 4, for aerosol between 0.15 and 0.30 μm radius at altitudes of 13 to 18 km (Figure 4.18). The concentration enhancements span the UTLS, peaking at 16.5 km (~1.5 km above the local tropopause) and extending 3 kilometers into the stratosphere. There is a hint of a concentration enhancement in a narrow layer at 17 km in the condensation nuclei profile (not shown), but no signature of the layer for particles > 0.50 μm. The aerosol profiles on 25 July 2001 are shown compared with measurements on 31 August 2000, an unperturbed summer profile with a similar temperature profile, and tropopause ~14 km. In August 2000 the aerosol exhibit a typical profile for non-volcanic UTLS aerosol, displaying a minimum in the UTLS,

then increasing to a concentration maximum near 22 km, the well known stratospheric aerosol layer.

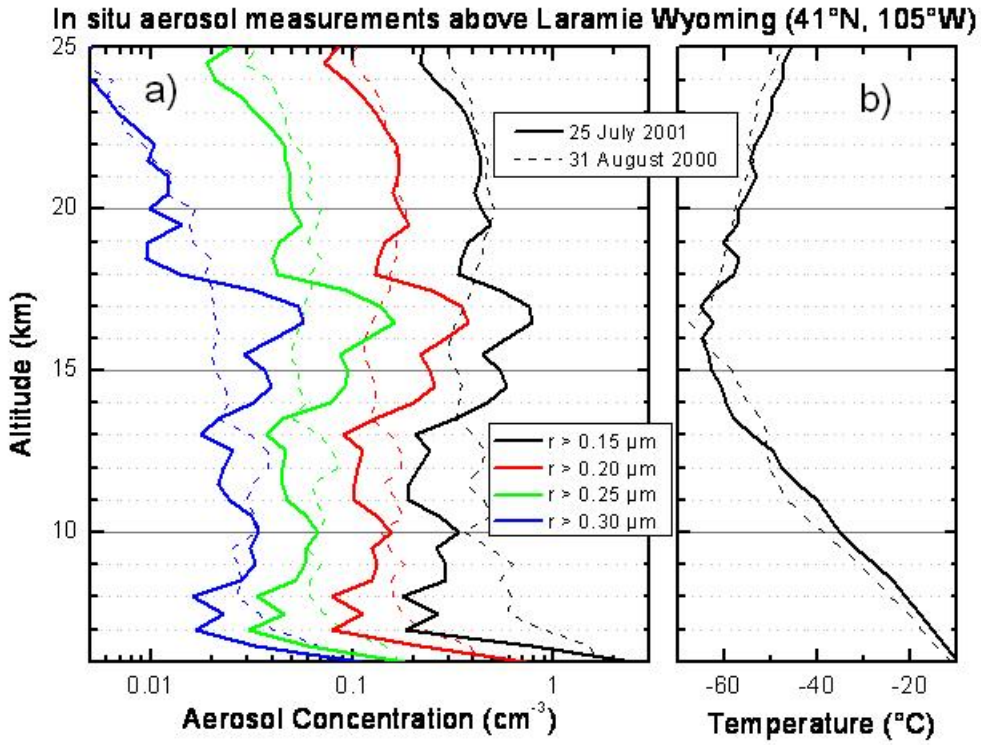

Figure 4.18. a) Aerosol concentration profile at 4 sizes above Laramie, Wyoming, on 31 August 2000 (dashed lines) and 25 July 2001 (solid lines). b) Temperature and potential temperature profiles on 31 August 2000 and 25 July 2001, indicating a tropopause between 14 and 15 km on the two days, respectively.

For an indication of the aerosol enhancement carried in the Chisholm pyroCb plume the aerosol concentration measurements were fitted with bimodal lognormal size distributions [Deshler et al., 2003] which were then used to calculate volume distributions for aerosol layers in and above the plume on 25 July 2001 and for similar altitudes on 31 August 2001. These are shown in Figure 4.19 as both differential and cumulative volume distributions. The distributions at 20 km on both days are quite similar and are narrower than the distributions at 16.5 km, as expected. The distributions at 16.5 km have approximately the same width, but the layer on 25 July 2001 shows a significant volume enhancement between 0.03 and 0.6 µm. The cumulative volume carried in the unperturbed layers on 31 August 2000 and at 20 km

on 25 July 2001 were all similar, 0.3 - 0.4 μm^3 cm^{-3}, whereas the aerosol in the 16.5 km layer on 25 July 2001 had a volume of near 0.9 μm^3 cm^{-3}, a factor of 2 to 3 larger.

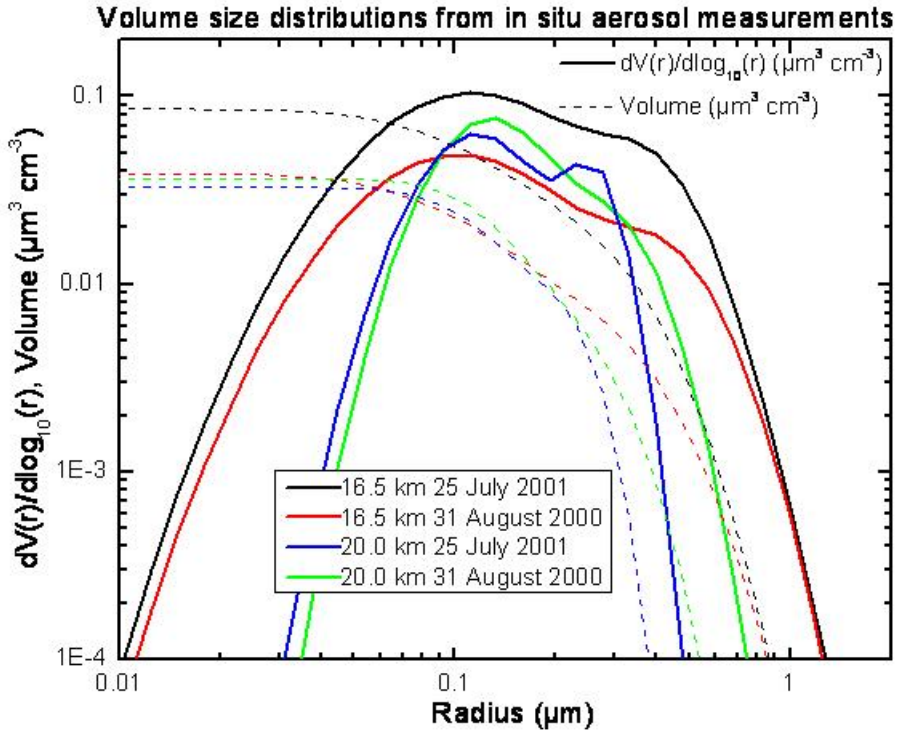

Figure 4.19. Differential and cumulative volume distributions from bimodal lognormal size distributions fit to the aerosol measurements at 16.5 and 20 km on 31 August 2000 (red and green) and 25 July 2001 (black and blue). The total volume carried in each layer is given by the point where the cumulative distribution lines intersect the left axis.

4.4 Summary and Conclusions

This chapter complements the studies of the Chisholm (Alberta) pyroCb by Fromm and Servranckx [2003] and Rosenfeld et al. [2007] who described the convective lifecycle, injection of smoke into the UTLS, and the young stratospheric smoke plume. Here, we analyzed profiles measured by three solar occultation instruments (POAM III, SAGE II, and HALOE), seven ground based lidars, and a balloon-borne aerosol instrument. The satellite observations were between 25° and 69°N; the lidars are stationed between 20° and 79°N. Each instrument's peculiar

measurement pattern in space and time was synthesized to develop a picture of the Chisholm plume's impressive spread into a hemispheric phenomenon.

The Chisholm pyroCb on 28 May 2001 caused a spike in the TOMS AI that was the most intense AI plume in the more than two-decade history of TOMS measurements. This stand-alone spike allowed us to conclude that the stratospheric aerosol perturbation reflected in the various profiles was smoke and that the Chisholm pyroCb was the singular cause.

We used two SO profiles, from POAM III and HALOE, on 1 and 5 June respectively, to confirm and characterize the stratospheric impact of Chisholm within a week of the eruption. Back trajectories from the POAM layer matched the Chisholm blowup precisely; the HALOE profile—the first HALOE measurement identified as a stratospheric smoke layer—showed that the smoke plume reached sub-tropical latitudes in agreement with TOMS AI enhancements reported in Chapter 3. A second POAM profile, in July, showed the remarkable result that Chisholm smoke reached an altitude at least as high as 18 km, Θ=458K, 9.5 km above the tropopause. By 11 June 2001, two weeks after the pyroCb, the Chisholm plume was sufficiently broad that it was detected by several POAM and SAGE profiles. The "leading edge" at that time was over far eastern Asia and the northern Pacific Ocean at these two instruments' measurement latitudes.

The stratospheric Chisholm smoke plume caused a doubling of the zonal average POAM AOD four weeks after the eruption, a gradual subsequent decay, yet still perturbed through August 2001. On or about 24 June (the time of the doubled AOD), aerosol layers were recorded at 79°, 54°, 47°, 40°, and 20°N—the plume ranged from the high Arctic to the northern tropics. SAGE data were presented in monthly statistical profiles to show that the plume persisted as high as 6 km above the tropopause, and spread from a regional phenomenon in June to hemispheric in July and August.

In addition to the first-ever stratospheric smoke layer identified in HALOE data, this report also presented first-ever smoke signatures from ground-based lidar at Ny Ålesund, Esrange, Kühlungsborn, Garmisch Partenkirchen, Boulder, and Mauna Loa.

The Ny Ålesund measurements provided two new insights: 1) new constraint on north poleward transport of stratospheric pyroCb smoke, and 2) a possible link between the smoke layer and localized increase in temperature. A similar (albeit qualitative) correlation between aerosol and temperature was observed at Esrange, Kühlungsborn, and Garmisch Partenkirchen. This suggests an important forcing between the absorbing stratospheric smoke and diabatic heating. These preliminary findings call for a more exhaustive, systematic approach for future work.

The lidar at Garmisch Partenkirchen also measured Chisholm smoke layers on three dates in late June and early July. Lidar data from this location have been a cornerstone of stratospheric aerosol research dating back to 1976 [Jäger, 2005]. We are presently investigating the possibility that some episodes of enhanced aerosols in the lowermost stratosphere at this location, formerly characterized as volcanically forced, may have instead been caused by pyroCb.

Perhaps the most surprising new insight gained from the many observations of the Chisholm smoke plume come from Mauna Loa. Two lidars, which recorded 61 profiles from May-August 2001, revealed a persistently perturbed aerosol condition at a location often influenced by tropical air masses. Our investigation showed that this perturbation did not occur in the prior two summers, that the altitude of many of the layers ruled out sub-visual cirrus, and that the top-most impacted altitude was in close agreement with the POAM layer observation (at 55°N) at 458K. These findings call for a deeper investigation into low-latitude profiles from both lidar and space-based instruments to assess the occurrence of tropical smoke layers, to distinguish UTLS smoke layers from subvisual cirrus, and to model stratospheric transport pathways between the mid-latitudes and tropics.

The Chisholm pyroCb was indeed a remarkable stratospheric pollution event. A single pyroconvective impulse, lasting on the order of 3 hours, injected enough smoke into the UTLS to blanket the northern hemisphere from the tropics to the high Arctic, double the aerosol burden, and persist for at least 3 months. With the other pyroCbs reported in the literature, the Chisholm phenomenon signifies a recurring albeit episodic eruptive force akin to some minor volcanic eruptions. A preliminary indication discussed herein--that the smoke pall perturbed stratospheric temperature--is another aspect of the pyroCb that calls for more research.

Chapter 5: Thermal Impact of Stratospheric Smoke

5.1 Introduction

We have seen that the pyroCb eruption can pollute the stratosphere on hemispheric scales, in apparent violation of long-held assumptions regarding the effectiveness of the tropopause to suppress violent upward motions [e.g. Poulida et al., 1996]. What is the potential for climatic impact of pyroCb on the troposphere and stratosphere? This chapter presents relations between stratospheric smoke and both temperature and tropopause height on a zonal average scale. Using measurements of lower stratospheric aerosol extinction and AOD and temperature/tropopause analyses we show that in two different boreal seasons, three distinct pyroCb injections significantly perturbed stratospheric aerosol loading coincident with stratospheric warming, tropospheric cooling, and lowered tropopause height. In addition we present a radiative transfer model simulation of a stratospheric smoke pall giving results consistent with the observations. Thus the newly discovered phenomenon, which occurs with newfound frequency, may play a significant role in climate as well as atmospheric chemistry/dynamics.

The climate impact of a hemispheric smoke pall in the UTLS was the subject of theoretical studies regarding the phenomenon called "Nuclear Winter" in the 1980s [Crutzen and Birks, 1982; Turco et al., 1983; Pyne and Omi, 1986] and more recently [Toon et al., 2007]. Smoke from large-scale conflagrations, lifted convectively, would warm the UTLS and cool the lower troposphere. The warming is a result of absorption of solar radiation by carbonaceous smoke aerosols. The cooling is a consequence of increased reflection of incoming solar radiation by the aerosols which in the global net create a brighter surface than the aerosol-free condition. Case studies have confirmed such a cooling effect on a regional scale [Robock, 1991; Westphal and Toon, 1991]. In these studies it was noted that there was no compensating warming because smoke particle size made them transparent at THIR wavelengths. A UTLS aerosol layer has a long lifetime owing to its position above

precipitation scavenging processes or in the stably stratified stratosphere; hence even a relatively optically thin layer could have a considerable radiative impact.

Another manifestation of stratospheric episodic aerosol increase, that due to volcanic injection of sulfur-containing gases, is the only heretofore observed form of a hemispheric aerosol perturbation with climatic impact [Labitzke and McCormick, 1992; Minnis et al., 1993]. The sulfuric acid droplets that evolve from the volcanic injection cool the lower troposphere by the increased reflection of solar radiation described above [Robock, 2000]. Stratospheric warming also results, albeit primarily from increased absorption of terrestrial long-wave radiation by the aerosol layer [Robock, 2000]. Thus in a qualitative sense the manifestation of a plinian volcanic eruption's thermal effect may be considered similar to that of a stratospheric smoke pall.

Here we will relate POAM aerosol data with two independent temperature data sets and tropopause-height analyses to establish correlations between LS smoke anomalies and temperature in the LS as well as the lower troposphere (LT). Then we perform calculations with a radiative transfer model to explore heating localized heating effects of a LS aerosol consistent with observations.

5.2 Method

In 1998 POAM III observed at least two smoke injections—in July and August. The second, larger injection in August was tied to a massive pyroCb in northwestern Canada [Fromm et al., 2005]. The July anomaly was attributed to pyroconvection [Fromm et al., 2000] without proof. (Unpublished current work has now identified at least one pyroCb, on 4 July 1998 in British Columbia, linked to stratospheric smoke layers.) As revealed in Chapter 4, the Chisholm pyroCb in 2001 doubled stratospheric zonal average AOD at the POAM measurement latitude and to pollute the stratosphere from Arctic to tropical latitudes. Moreover, several of the

stratospheric aerosol-layer observations were shown to coincide with increased temperature suggestive of a localized shortwave-absorption radiative impact.

Here we employ POAM III daily zonal average AOD data as previously reported, with two additional data sets to explore the linkage between the three 1998 and 2001 smoke injections and atmospheric impact. One temperature data set is from the long-term satellite-borne Microwave Sounding Unit (MSU) and Advanced MSU (AMSU) [Christy et al., 2000, 2003]. This record, from 1979 on, consists of daily-resolved zonal average temperatures on a latitude-grid of 2.5º. The temperature product is a temperature "anomaly," a value normalized by differencing from a long-term average. This temperature data set, which has been used for studies of temperature trends and volcanic impact [Robock, 2000; Dutton and Christy, 1992], includes a lower tropospheric and lower stratospheric component.

The second temperature data set consists of radiosonde measurements. We chose profiles between 55° and 65°N, and mandatory levels (925, 850, 700, 215, and 100 hPa) to represent lower troposphere, upper troposphere, and lower stratosphere, respectively. From all the radiosonde locations we calculated daily zonal average temperature.

In addition to the temperature data we calculate daily zonal average tropopause height using meteorological analyses from the UK Met Office [Swinbank and O'Neill, 1994]. Tropopause height is calculated using the dynamical definition, iusing the threshold of pv=+3PVU.

From the MSU temperature and tropopause data we calculate "climatological" values with which to compare the season of interest. We are interested in 3-month periods in 1998 (mid-June to mid-September) and 2001 (May to July). The climatological period is 1995-2005. An 11-year average for each date in the analysis period is calculated. Standard deviation is calculated using the entire 3-month period.

For the radiosonde-based temperature analysis the 11-year average is computed but the analysis discussed next uses the 11-year range.

The analysis of the temperature and tropopause data in relation to POAM LS AOD is a time series. The AOD time series is overplotted on the temperature and tropopause series to facilitate the identification of temporal correlations. POAM AOD in the season of interest is plotted along with the AOD for a single year during which there was no detectable perturbation—1999. This serves to provide a qualitative measure of the pyroCb-event perturbation.

We use the Santa Barbara DISORT Atmospheric Radiative Transfer (SBDART) code [Ricchiazzi et al., 1998] to simulate shortwave heating of an absorbing smoke layer in the lowermost stratosphere. Input to the model are daily zonal average profiles of 550 nm aerosol extinction from POAM III. Individual profiles are converted to a tropopause relative grid before daily averaging. To determination the optical properties, North American biomass burning model reported by Dubovik et al. [2002] was used. Single scattering albedo values obtained by this model are ~0.93. Daily heating rate is calculated based on solar zenith angle consistent with day of year and POAM measurement latitude. Integration of heating rate is performed for the period 1-23 August 1998, the period during which POAM AOD evolved from unenhanced to peak perturbation.

5.3 Results

5.3.1 Data analysis

The 3-month time series in summer 1998 (Figure 5.1) includes the July and August pyroCb-caused AOD perturbations. In the earliest weeks AOD is unperturbed. MSU lower stratospheric temperature (LST) varies within one standard deviation of the norm; lower tropospheric temperature (LTT) is consistently warmer than the norm; and tropopause height varies little from the norm. In July when AOD

doubles, LST increases beyond the one-sigma envelope, LTT drops well below the norm, and tropopause height reaches a local minimum. After the August 1998 pyroCb, AOD quintuples, LST increases to a local maximum well beyond the one-sigma envelope for approximately two weeks, LTT again drops tangibly, as does tropopause height. In September, as AOD relaxes, LST, LTT, and tropopause height generally converge back toward the norm. Figure 5.2 gives a similar time series but with radiosonde temperature. The 100 hPa zonal average temperature in 1998, in relation to the 1995-2005 range, exhibits a pattern quite similar to the MSU LST. Perceptible episodic increases of 100 hPa in mid-July and in the last half of August are coincident with the AOD anomalies. The temperature departure from the 11-year mean is largest at the time of the two AOD perturbation maxima. In particular the August temperature increase is as great as any in the 11-year envelope for more than one week. At 215 hPa (roughly the UT jet stream level) the correlation with AOD is more complex. However, at 700 and 850 hPa a perceptible localized decrease in temperature with respect to the average occurs in coincidence with the AOD maxima. A similar yet muted signal is also observed at 925 hPa, which at different locations and times of day can represent the free troposphere or the planetary boundary layer.

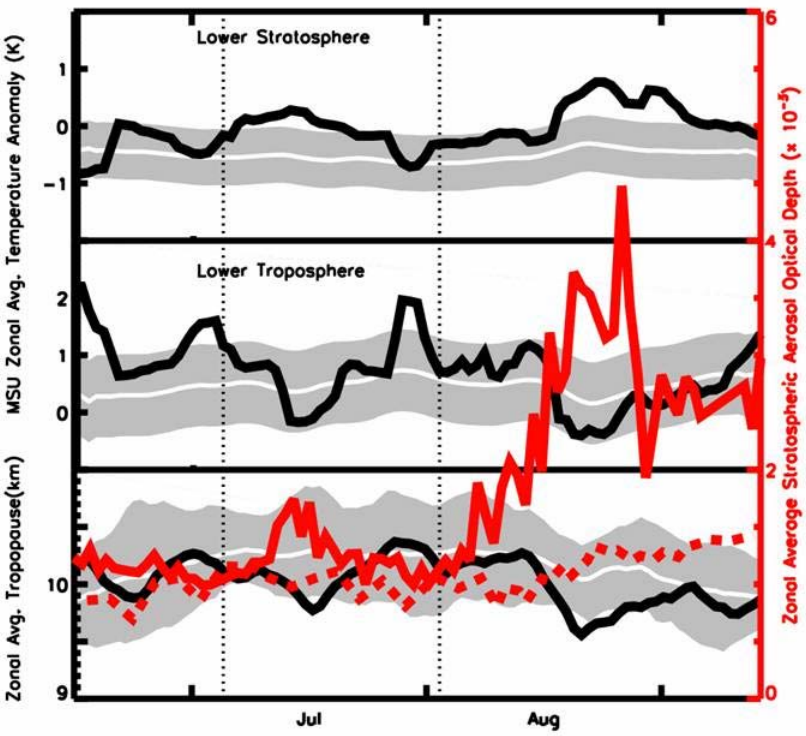

Figure 5.1 | Time series of stratospheric AOD, temperature, and tropopause height in summer 1998. Period: 15 June – 15 September. Temperature and tropopause data are daily zonal averages at 60ºN. POAM latitude varies gradually between 55 and 68ºN. Red solid line is 1998 AOD; dotted line is 1999. Thick black lines are 1998. White line and gray shaded area are the norm (average) and +/- one standard deviation respectively, for 1993-2003. Top panel: MSU lower stratosphere temperature anomaly. Seven-day smoothing is applied. Middle panel: MSU lower troposphere temperature anomaly. Bottom panel: tropopause height, calculated using the dynamical definition based on potential vorticity. Vertical dotted lines indicate date of pyroCb eruptions.

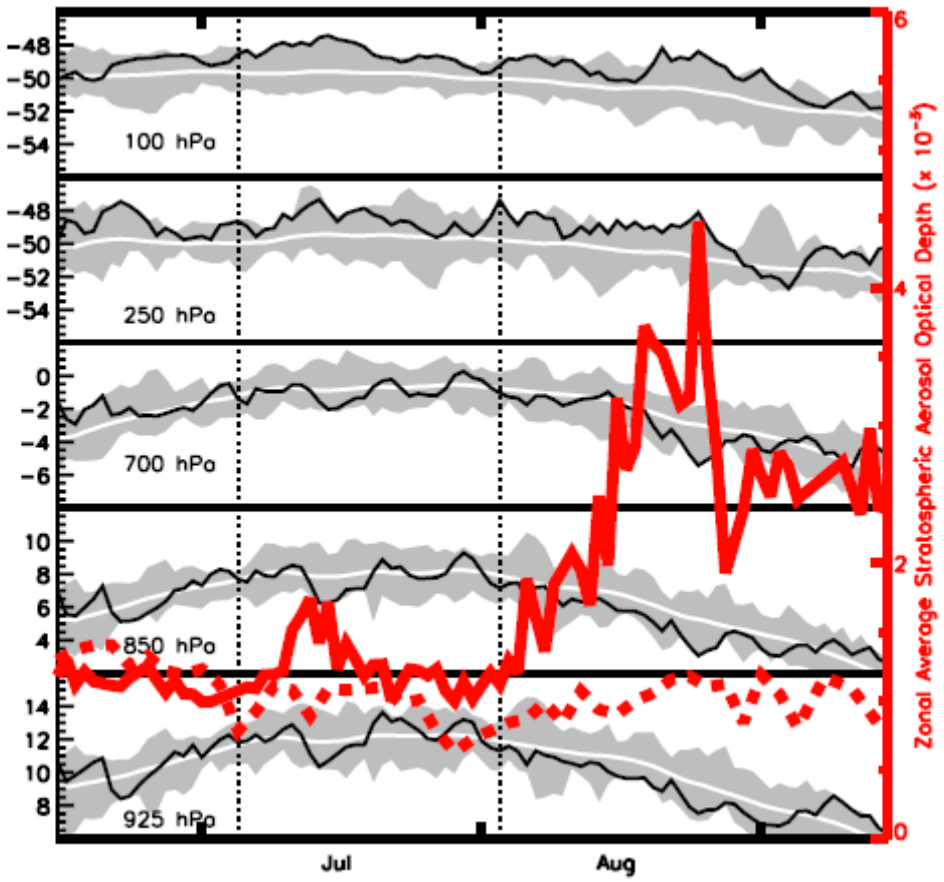

Figure 5.2 |Time series as in Figure 5.1, showing radiosonde daily zonal average for sites between 55 and 65N. Shaded area is the range for the 11-year period 1995-2005. White line is the 11-year average. Black line is for 1998. Five mandatory levels are shown, as labeled.

In 2001 (Figure 5.3), the spring/summer period is characterized by the singular AOD perturbation caused by the Chisholm pyroCb eruption. Prior to the AOD spike LST was generally near or cooler than the norm and LTT was consistently warmer. Except for a localized minimum in mid-May, tropopause height was greater than normal. When the Chisholm pyroCb AOD enhancement peaked in the last third of June, LST rose well above the norm and persisted in that state for roughly three weeks. LTT dropped sharply at the AOD increase and remained low for three weeks. At the same time the tropopause height dropped and remained relatively low.

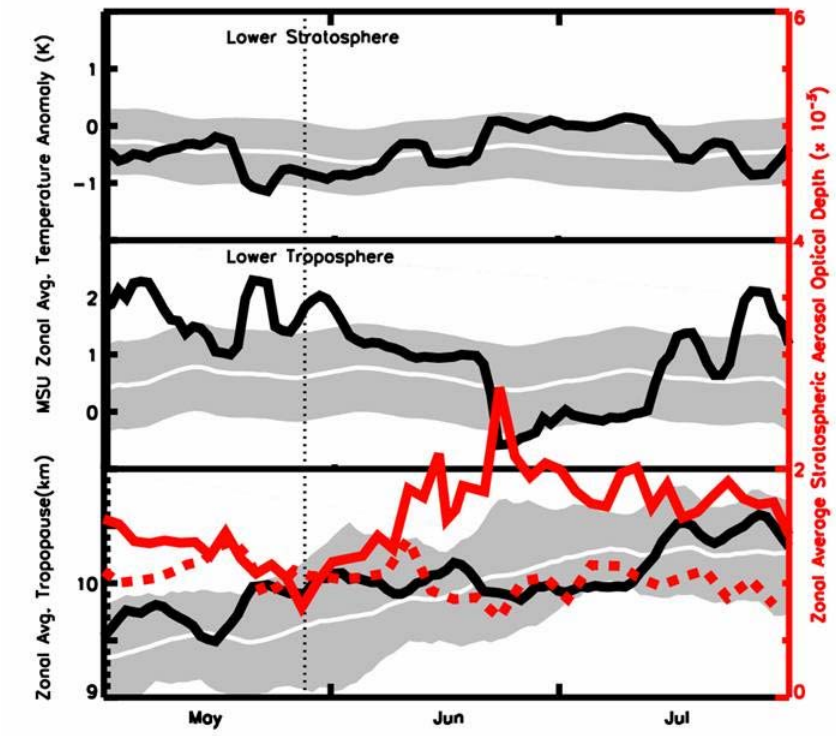

Figure 5.3 | Time series of stratospheric AOD, temperature, and tropopause height in spring/summer 2001. Period: 1 May – 31 July. As in Figure 5.1 except the norm and standard deviation are for 1996-2006.

5.3.2 Model Simulation

Daily heating rate in the LS between 1 and 23 August is shown in Figure 5.4 The heating rate is representative of the entire atmospheric layer from tropopause+2km to tropopause+15 km, consistent with the POAM aerosol profiles used. The integrated heating rate time series in Figure 5.4 illustrates that an aerosol abundance consistent with the POAM measurements in August 1998 and with a single scatter albedo representative of smoke gives a positive radiative stratospheric forcing in a zonal average scale in reasonable agreement with observations. We also analyzed heating rate at four individual altitudes, from tropopause+2km to tropopause+5km, and integrating in time from 1 to 23 August (not shown). The alternate view of accumulated heating indicates that at these altitudes, temperature increased in response to perturbed aerosol abundance between ~0.35 and 0.4 K. This

simplified simulation is meant only to show first-order estimates. For instance no processes such as smoke optical property evolution [Westphal and Toon, 1991] or diabatic-heating/lofting is considered here. Moreover, we do not assess the tropospheric radiative impact of a LS smoke layer. These are beyond the present scope but will be pursued in future investigations.

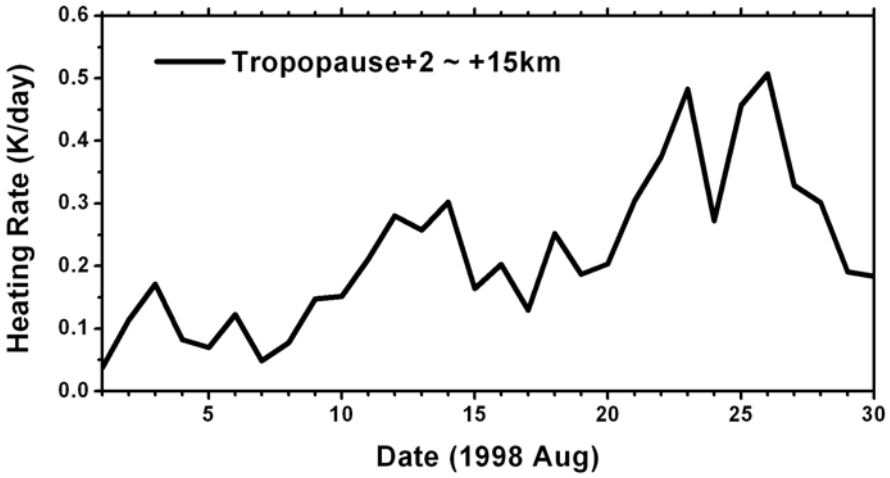

Figure 5.4 | Simulated stratospheric heating due to ambient smoke. (See Methods for details.) Time series of integrated lower stratospheric daily heating rate for period 1-23 August at POAM latitude (~58-62ºN). The integration is from tropopause+2km to tropopause+15km. Zonal average AOD enhancements (not shown) spanned from the tropopause to tropopause+7 km.

5.4 Discussion and Summary

The smoke injection from the three events illustrated here spanned stratospheric altitudes up to 9 km above the tropopause. However the pyroconvective process is known to inject emissions throughout the UTLS [Damoah et al., 2006]. Thus the radiative effect of these absorbing aerosols would straddle the tropopause. It is then reasonable to expect that any consequent warming would alter the temperature profile in such a way as to effectively warm the UTLS while lowering the tropopause height consistent with the results shown here. Hence the reported zonal average signal, persistent for days to weeks, suggests that the pyroCb effect strongly changes hemispheric UTLS properties and dynamics. This impact is not presently considered in any models of atmospheric dynamics or climate.

The hemispheric-scale, persistent lower tropospheric cooling shown in Figures 5.1-5.4 is as much as 1-2 K, but not as strongly evident as the coincident LS temperature/AOD correlation. The zonal average cooling is certainly consistent with expectations and findings based on tropospheric smoke palls, but the link we reported here requires more observational cases and modeling to strengthen and constrain the conclusions.

The localized pyroconvective eruptive phenomenon has important hemispheric ramifications. Considering the evolution of such plumes from an initial, concentrated perturbation to a zonally extensive pall, it is also reasonable to expect stronger, regional impact on temperature and thus weather. Assessing regional impact is thus an important area of future research. In light of the relatively recent discovery of pyroCb emissions in the stratosphere and these results implicating a strong radiative impact, it will be necessary to more fully characterize the pyroCb dynamic, occurrence frequency, impact on weather, and relation to climate change scenarios.

Chapter 6. Summation

6.1 Summary of Findings

The first reports of forest fire smoke in the stratosphere and discovery of pyroCb were published only recently (since 2000) [Fromm et al., 2000]. Since that time a few additional cases have been reported [e.g. Jost et al., 2004; Livesey et al., 2004], and modelling of pyroCb processes has begun [e.g. Trentmann et al., 2006]. However, quantitative studies of pyroCb frequency, smoke plume composition, and atmospheric impact are still needed. This dissertation is a contribution to the area of work thus called for.

Herein we reported on a pyroCb in Canberra, Australia on 18 January 2003. This is the first finding and end-to-end analysis of a southern hemisphere pyroCb event with considerable stratospheric smoke pollution. This Australian firestorm was one of several large fires in the austral summer of 2002/2003; other deep pyroconvection was in evidence but not explored here. Nonetheless, now it is established that this phenomenon occurs in midlatitudes of both hemispheres and may be a recurring phenomenon in both as well. Moreover, this study showed that the pyroCb spawns peculiar cloud microphysics—abnormally small cloud droplets/crystals—which may represent a positive feedback on updraft strength. The reported F2 tornado is consistent with this extreme behavior. Like northern pyroCbs previously reported [e.g. Fromm et al., 2005] the Canberra pyroCb increased stratospheric AOD on a hemispheric scale; a pall which persisted at least one month.

A previously reported [Fromm and Servranckx, 2003] pyroCb near the hamlet of Chisholm in Alberta in May 2001 was the subject of two chapters herein. This remarkable fire storm is a special case in that it occurred in a season noted for the relative absence of fire activity in the boreal realm [Brian Stocks, personal communication, 2007; Pu et al., 2007]. In fact it is concluded herein that the Chisholm pyroCb was singularly responsible for a doubling of zonal average AOD in the lowermost stratosphere. The stratospheric smoke—observed as high as 9 km above the tropopause—spread from Arctic to tropical meteorological regimes

[Hudson et al., 2003] and persisted for more than one month. Smoke particle effective mean radius was found to be typically between 0.3 and 0.6 μm. Some of the smoke-layer measurements were accompanied by temperature profiles that were suggestive of localized warming. The circumstantial evidence was bolstered by the apparent smoke-layer warming at several lidar locations and measurement times. Thus these may be the first reported hints of an expected radiative impact of light-absorbing aerosols in the stratosphere as put forward in, for instance, the Nuclear Winter scenario [Turco et al., 1983].

The pyroCb eruption deposited a peculiar cloud that continues to defy straightforward characterization. Thermal infrared brightness-temperature difference analysis revealed that the storm's young effluent cloud consisted of particles on the order of 10 μm, much smaller than normal cirrus ice. However, the cloud was optically thick at brightness temperatures lower than the tropopause-region cold point for more than 8 hours after convection ceased. The cloud was characterized as smoke-polluted ice that "dried" to transparent (with respect to thermal IR) over a span that exceeded 1.6 days. This revelation implies a considerable transport of water into the stratosphere as well.

First attempts were made to calculate smoke mass injected into the stratosphere. The Chisholm pyroCb injected roughly 20,000 t of smoke, which represented a non-negligible proportion of the hemispheric background sulphate aerosol mass. This finding and the characterization reported herein of initial smoke plume horizontal and vertical extent are necessary for initializing transport or general circulation models for the study of such events.

Building on the suggestive relation of stratospheric smoke and locally warmed air reported in Chapter 4, Chapter 5 presented an assessment of large-scale radiative impact of pyroCb smoke in the stratosphere. Through data analysis of combined zonal average AOD and temperature, it was shown that in two different boreal summers containing at least three major pyroCb smoke injections to the stratosphere, measured stratospheric temperature increased during the smoke-perturbed periods. It

was also shown that lower tropospheric zonal average temperature decreased in concert with the smoke-palls. Future exploration of this is called for to determine the robustness of this correlation.

To test the apparent link between the warmer and smokier stratosphere, a radiative transfer simulation of one of the three perturbed periods was performed. The radiative transfer model was driven by aerosol measurements when stratospheric AOD increased five-fold in August 1998 at ~60°N. Daily, zonal average heating rate calculations produced a positive thermal impact on the order of 0.5K in the lowermost stratosphere; the observational approach indicated a positive effect ~1K. Hence we conclude that the observations were supported by radiative transfer theory and that the documented pyroCb events led to a detectable, persistent positive thermal impact at the level of the smoke perturbation. These results call for continued and expanded investigations of this type.

6.2 Future Work

The still young area of pyroCb research is ripe for new investigations. There is still large uncertainty regarding global pyroconvective processes in terms of frequency, intensity, trends, and relationship—if any—with climate change. It is also insufficiently known how and when significant pyroCb injections have impacted the stratosphere in the past. The peer-reviewed literature contains many references to "mystery cloud" events and occasions when a suspected volcanic cloud had characteristics inconsistent with expectations [e.g. Sassen and Horel, 1990; Sassen et al., 1994]. Perhaps stratospheric smoke has been the unknown feature of some past phenomena and thus can provide a new and better interpretation of the atmospheric processes and impact. Climate models do not account for pyroconvective processes and presently there is no accounting for light-absorbing in the UTLS in climate simulations. Hence the future directions for pyroCb research include experimental and theoretical avenues.

A natural and important vein of future pyroCb research is to focus on the satellite era to build a pyroCb climatology. For example, TOMS or TOMS-like

instruments have been recording global aerosol index since 1978. Works such as this dissertation have shown that AI may be a strategic data resource for building a climatology of dense, young, UTLS smoke plumes. Then in combination with visible and IR imagery—which also date to 1978—links with large fire and pyroconvection can be ascertained by objective hot spot and burn-scar detection [e.g. Li et al., 2003]. Moreover, satellite-based aerosol profiles such as those from SAM II and SAGE I-III sample the globe for the identical range of time and can be exploited to better characterize pyroCb cause and effect.

Since 2000 a new mix of satellites that can be employed strategically in pyroCb research has been placed into orbit. It is beyond the scope here to make a complete survey. However, a particular mention of NASA's A-Train is warranted. The formation flying of AURA, MODIS, CloudSat, CALIPSO, and Aqua provide an unprecedented opportunity to study pyroCb from the standpoint of cloud microphysics (e.g. CloudSat and CALIPSO), injection height (CALIPSO), plume composition (e.g. CALIPSO, AURA Microwave Limb Sounder CO, O_3, and H_2O), and plume transport (CALIPSO and AURA OMI AI). In addition to satellite networks, ground-based systems such as AERONET and the Micro-pulse lidar network (MPLNET) can be strategically employed as well.

Basic and important physical and optical properties of wild fire smoke are still lossley constrained. For instance, smoke-particle single scatter albedo—critical to characterizing its radiative impact—varies in the literature from values between 0.3 and 0.95. Moreover it is essentially unknown how the properties of smoke in the lower stratosphere, deposited through a moist pyroconvective updraft, are altered and affected by aging. Hence it will be important to strive for direct measurements of UTLS smoke plumes in the future.

In addition to observations, model simulations of pyroCb processes are also needed. It is still unclear how "regular" deep convection relates to the pyroconvective counterpart. Air mass thunderstorms are known to be effective agents of pollution transport to high altitudes [Dickerson et al., 1987]. For instance, how

similar are the turbulent exchanges of material at the top of energetic UTLS convection columns for these two processes? The answer to such questions will most likely fall in the domain of modelling, based on insights gained from case studies. Hence it will be valuable to establish observational records of deep "regular" and pyroconvection in similar environmental conditions and employ sufficiently detailed models to simulate the processes and verify the results.

This work presented initial studies of the radiative impact of pyroCb smoke plumes on the stratosphere and lower troposphere. These attempts indicate that there is a sufficiently strong temperature signal indicating hemispheric impact akin to the Nuclear Winter scenario (i.e UTLS warming and tropospheric cooling) to justify additional observation-based studies and model simulations. In particular it would be strategic to employ transport models with a radiative transfer code to assess regional temperature impact and compare with observations. Realistic modelling of observation-based pyroCb plume characteristics on a global scale will also be invaluable for assessing the relative radiative forcing attributable to UTLS pyroCb emissions in relation to more firmly established global radiative forcing terms.

References

Alfred, J., M. Fromm, R. Bevilacqua, G. Nedoluha, A. Strawa, L. Poole, and J. Wickert (2007), Observations and analysis of polar stratospheric clouds detected by POAM III and SAGE III during the SOLVE II/VINTERSOL campaign in the 2002/2003 Northern Hemisphere winter, *Atmos. Chem. Phys.*, **7**, 2151-2163.

Alpers, M., R. Eixmann, J. Höffner, T. Köpnick, J. Schneider, and U. von Zahn (1999), The Rayleigh/Mie/Raman lidar at IAP Kühlungsborn, *J. Aerosol. Sci.*, **30**, Suppl. 1, S637-S638.

Alpers, M., R. Eixmann, C. Fricke-Begemann, M. Gerding, and J. Höffner (2004), Temperature lidar measurements from 1 to 105 km altitude using resonance, Rayleigh, and Rotational Raman scattering, *Atmos. Chem. Phys.*, **4,** 793-800.

Arking, A., and J. Childs (1985), Retrieval of Cloud Cover Parameters from Multispectral Satellite Images, *J. Clim. and Appl. Meteor*., 24, 322-333.

ASRD: Final Documentation Report (2001), Chisholm Fire (LWF-063), Forest Protection Division, ISBN 0-7785-1841-8, Tech. rep., Alberta Sustainable Resource Development.

Beekmann, M., G. Ancellet, S. Blonsky, D. De Muer, A. Ebel, H. Elbern, J. Hendricks, J. Kowol, C. Mancier, R. Sladkovic, H. G. J. Smit, P. Speth, T. Trickl, and P. Van Haver (1997), Regional and global tropopause fold occurrence and related ozone flux across the tropopause, *J. Atmos. Chem.*, **28**, 29-44.

Bertaux, J.-L., E. Kyrölä, and T. Wehr (2000), Stellar occultation technique for atmospheric ozone monitoring: GOMOS on Envisat, *Earth Observation Quarterly*, **67**, 17-20.

Bevilacqua, R.M., M. D. Fromm, J. M. Alfred, J. H. Hornstein, G. E. Nedoluha, K.W. Hoppel, J. D. Lumpe, C. E. Randall, E. P. Shettle, E. V. Browell, C. Butler, A. Dörnbrack, and A. W. Strawa (2002), Observations and analysis of PSCs detected by POAM III during the 1999/2000 northern hemisphere winter, *J. Geophys. Res.*, **107(D20)**, 8281, doi:10.1029/2001JD000477.

Bhartia, P.K. (2007), Total Ozone from backscattered ultraviolet measurements, pp 48-63 in *Observing Systems for Atmospheric Composition*, G. Visconti, P. Di Carlo, W.H. Brune, M. Schoeberl, A. Wahner, editors, Springer.

Blum, U. and K. H. Fricke (2005), The Bonn University lidar at the Esrange: technical description and capabilities for atmospheric research, *Ann. Geophys*., **23**, 1645-1658, SRef-ID: 1432-0576/ag/2005-23-1645.

Bluth, G., W. Rose, I Sprod, and A Krueger (1997), Stratospheric loading of sulfur from explosive volcanic eruptions, *J. Geol*., **105**, 671-683.

Bovensmann, H., J. Burrows, M. Buchwitz, J. Frerick, S. Noël, V. Rozanov, K.Chance, and A. Goede (1999), SCIAMACHY: Mission objectives and measurement modes, *J. Atmos. Sci*., **56***, 2*, 127-150.

Brasseur, G., and S. Solomon (1986), Aeronomy of the Middle Atmosphere, Reidel, Dordrecht, 452 pp.

Christy, J., Spencer, R., Norris, W., and Braswell, W., (2003), Error estimates of version 5.0 of MSU-AMSU bulk atmospheric temperatures, J*ourn. Atmos. Oc. Tech*. **20**, 613-629.

Christy, J., Spencer, R., and Braswell, R., (2000), MSU tropospheric temperatures: dataset construction and radiosonde comparisons, *Journ. Atmos. Oc. Tech*. **17**, 1153-1170.

Crutzen, P. and J. Birks (1982), The atmosphere after a nuclear war: twilight at noon, *Ambio*, **11**, 114-125.

Daerden, F., N. Larsen, S. Chabrillat, Q. Errera, S. Bonjean, D. Fonteyn, K. Hoppel, M. Fromm (2007), A 3D-CTM with detailed online PSC-microphysics: analysis of the Antarctic winter 2003 by comparison with satellite observations, *Atmos. Chem. & Phys.*, **7**, 1755-1772.

Damoah, R., N. Spichtinger, R. Servranckx, M. Fromm, E. Eloranta, I. Razenkov, P. James, M. Shulski, C. Forster, and A. Stohl (2006), A case study of pyro-convection using transport model and remote sensing data, *Atmos. Chem. Phys.*, **6**, 173-185.

de Graaf, M., P. Stammes, O. Torres, R. B. A. Koelemeijer (2005), Absorbing Aerosol Index: Sensitivity analysis, application to GOME and comparison with TOMS, *J. Geophys. Res.*, **110**, D01201, doi:10.1029/2004JD005178.

Deshler, T., M. E. Hervig, D. J. Hofmann, J. M. Rosen, and J. B. Liley (2003), Thirty years of in situ stratospheric aerosol size distribution measurements from Laramie, Wyoming (41°N), using balloon-borne instruments, *J. Geophys. Res., 108(D5)*, 4167, doi:10.1029/2002JD002514.

Deshler, T., R. Anderson-Sprecher, H. Jäger, J. Barnes, D. J. Hofmann, B. Clemesha, D. Simonich, R. G. Grainger, S. Godin-Beekmann (2006), Trends in the non-volcanic component of stratospheric aerosol over the period 1971-2004, *J. Geophys. Res.,* **111***, D01201*, doi: 10.1029/2005JD006089, 21.

Dickerson, R., G. Huffman, W. Luke, L. Nunnermacker, K. Pickering, A. Leslie, C. Lindsey, W. Slinn, T. Kelly, A. Delany, J. Greenberg, P. Zimmerman, J. Boatman, J. Ray and D. Stedman, Thunderstorms: An Important Mechanism in the Transport of Air Pollutants, *Science,* **235**, 460-465, 1987.

Draxler, R., and G. Hess (1998), An overview of the HYSPLIT_4 modelling system for trajectories, dispersion, and deposition, *Aust. Meteorol. Mag*., **47**, 295-308.

Diner, D.J., J.C. Beckert, T.H. Reilly, C.J. Bruegge, J.E. Conel, R. Kahn, J.V. Martonchik, T.P. Ackerman, R. Davies, S.A.W. Gerstl, H.R. Gordon, J-P. Muller, R. Myneni, R.J. Sellers, B. Pinty, and M.M. Verstraete (1998), Multi-angle Imaging SpectroRadiometer (MISR) description and experiment overview. *IEEE Trans. Geosci. Rem. Sens.*, **36** (4), 1072-1087.

Dutton, E., and Christy, J., (1992), Solar radiative forcing at selected locations and evidence for global lower tropospheric cooling following the eruption of El Chichón and Pinatubo, *Geophys. Res. Lett.* **19**, 2313-2316.

Freudenthaler, V., F. Homburg, H. Jäger (1994), Ground-based mobile scanning lidar for remote sensing of contrails, *Ann. Geophys*., **12**, 956–961.

Fromm, M., J. Alfred, K. Hoppel, J. Hornstein, R. Bevilacqua, E. Shettle, R. Servranckx, Z. Li, and B. Stocks (2000), Observations of boreal forest fire smoke in the stratosphere by POAM III, SAGE II, and lidar in 1998, *Geophys. Res. Lett.*, **27,** 1407-1410.

Fromm, M., and R. Servranckx (2003), Transport of forest fire smoke above the tropopause by supercell convection, *Geophys. Res. Lett.*, **30 (10)**, 1542.

Fromm, M., J. Alfred, and M. Pitts (2003), A unified, long-term, high-latitude stratospheric aerosol and cloud database using SAM II, SAGE II, and POAM II/III data: Algorithm description, database definition, and climatology", *J. Geophys. Res.*, **108(D12),** 4366, doi:10.1029/2002JD002772.

Fromm, M., R. Bevilacqua, B. Stocks, and R. Servranckx (2004), New Directions: Eruptive transport to the stratosphere: add fire-convection to volcanoes, *Atmos. Env.,* **38**, 163-165.

Fromm, M., R. Bevilacqua, R. Servranckx, J. Rosen, J.P. Thayer, J. Herman, and D. Larko (2005), Pyro-cumulonimbus injection of smoke to the stratosphere: observations and impact of a super blowup in northwestern Canada on 3-4 August 1998, *J. Geophys. Res.*, **110** (D8), D08205.

Fromm, M., A. Tupper, D. Rosenfeld, R. Servranckx, and R. McRae (2006), Violent pyro-convective storm devastates Australia's capital and pollutes the stratosphere *Geophys. Res. Lett.*, **33**, L05815, doi:10.1029/2005GL025161.

Gothe, M. and H. Grassl (1993), Satellite remote sensing of the optical depth and mean crystal size of thin cirrus clouds and contrails, *Theor. Appl. Climatol.*, **48**, 101-113.

Guo, S., W. Rose, G. Bluth, I. M. Watson (2004), Particles in the great Pinatubo volcanic cloud of June 1991: The role of ice, *Geochem. Geophys. Geosystems*, **5**, 5, Q05003, doi:10.1029/2003GC000655.

Herman, J.R., P.K. Bhartia, O. Torres, C.Hsu , C. Seftor, and E. Celarier (1997), Global Distribution of UV-absorbing Aerosols From Nimbus-7/TOMS data*, J. Geophys. Res.*, **102**, 16911-16922.

Hobbs, P., J. Reid, J. Herring, J. Nance, R. Weiss, J. Ross, D. Hegg, R. Ottmar, C. Liousse (1996), Particle and trace-gas measurements in smoke from prescribed burns of forest products in the Pacific Northwest, in: *Biomass Burning and Global C*hange, Vol. 1, edited by: Levine, J. S., 697-715, MIT Press, New York, 1006.

Hervig, M.E., T. Deshler, and J.M. Russell (1998), Aerosol size distributions obtained from HALOE spectral extinction measurements, *J. Geophys. Res.*, **103**, 1573-1583.

Hervig, M. E. (1999), Stratospheric clouds over England, *Geophys. Res. Lett*., **26**, 1137-1140.

Hervig, M. and M. McHugh (1999), Cirrus detection using HALOE measurements, *Geophys. Res. Lett.*, **26**, 719-722.

Hofmann, D. J., J. M. Rosen, T. J. Pepin, and R. G. Pinnick (1975), Stratospheric aerosol measurements, I, Time variations at northern midlatitudes, *J. Atmos. Sci.,* **32**, 1446-1456.

Hofmann, D. (1990), Increase in the stratospheric background sulfuric-acid aerosol mass in the past 10 years, *Science*, **248**, 4958, 996-1000.

Hofmann, D. J. and T. Deshler (1991), Stratospheric cloud observations during formation of the Antarctic ozone hole in 1989, *J. Geophys. Res.,* **96**, 2897-2912.

Holton, J., P. Haynes, M. McIntyre, A. Douglas, R. Rood, and L. Pfister (1995), Stratosphere-troposphere exchange, *Rev. Geophys*., **33**, 403-439.

Horváth, Á. and R. Davies (2001), Simultaneous retrieval of cloud motion and height from polar-orbiter multiangle measurements. *Geophys. Res. Lett*., **28**, 2915-2918.

Hudson, R., A. Frolov, M. Andrade and M. Follette (2003), The total ozone field separated into meteorological regimes, Part I Defining the regimes, *J. Atmos. Science*, **60**, 1669-1677.

Jäger, H. (2005), Long-term record of lidar observations of the stratospheric aerosol layer at Garmisch-Partenkirchen, *J. Geophys. Res*., **110**, D08106, doi: 10.1029/2004JD005506, 9 pp.

Jost, H., K. Drdla, A. Stohl, L.Pfister, M. Loewenstein, J. Lopez, P. Hudson, D. Murphy, D. Cziczo, M. Fromm, T. Bui, J. Dean-Day, M. Mahoney, E. Richard, N. Spichtinger, J. Vellovic, E. Weinstock, J. Wilson, and S. Wofsy (2004), In-situ observations of mid-latitude forest fire plumes deep in the stratosphere, *Geophys. Res. Lett.*, **31**, L11101, doi:10.1029/2003GL019253.

Jovanovic, V.M., M.A. Bull, M.M. Smyth, and J. Zong (2002), MISR in-flight camera geometric model calibration and georectification performance. *IEEE Trans. Geosci. Remote Sens.,* **40**, 1512-1519.

Jovanovic, J., C. Moroney, and D. Nelson (2007), Multiangle geometric processing for globally geo-located and co-registered MISR image data. *Rem. Sens. Environ*., **107**, 22-32.

Kalnay E, M. Kanamitsu, R. Kistler, W. Collins, D. Deaven, L. Gandin, M. Iredell, S. Saha, G. White, J. Woollen, Y. Zhu, M. Chelliah, W. Ebisuzaki, W. Higgins, J. Janowiak, K. Mo, C. Ropelewski, J. Wang, A. Leetmaa, R. Reynolds, R. Jenne, D. Joseph (1996), The NCEP/NCAR 40-year reanalysis project, *Bull. Am. Meteor. Soc*., **77**, 437-471.

Kaufman, Y. J., D. Tanré, L. A. Remer, E. F. Vermote, A. Chu, and B. N. Holben (1997), Operational remote sensing of tropospheric aerosol over land from EOS moderate resolution imaging spectroradiometer. *J. Geophys. Res.*, **102**, 17051-17068.

Kempfer, U., W. Carnuth, R. Lotz, T. Trickl (1994), A wide-range UV lidar system for tropospheric ozone measurements: development and application, *Rev. Sci. Instrum.*, **65**, 3145-3164.

Kent, G., and M. McCormick (1984), SAGE and SAM II measurements of global stratospheric aerosol optical depth and mass loading, *J. Geophys. Res*., **89,** D4, 5303-5314.

King, M. D., Y. J. Kaufman, W. P. Menzel, and D. Tanré (1992), Remote sensing of cloud, aerosol, and water vapor properties from the Moderate Resolution Imaging Spectrometer (MODIS). *IEEE Trans. Geosci. Remote Sens.*, **30**, 1-27.

King, M. D., W. P. Menzel, Y. J. Kaufman, D. Tanré, B. C. Gao, S. Platnick, S. A. Ackerman, L. A. Remer, R. Pincus, and P. A. Hubanks (2003), Cloud and aerosol properties, precipitable water, and profiles of temperature and humidity from MODIS. *IEEE Trans. Geosci. Remote Sens.*, **41**, 442-458.

Klett, J. D. (1985), Lidar inversions with variable backscatter / extinction ratios, *Appl. Opt.,* **24,** 1638-1643.

Labitzke, K., and M. P. McCormick (1992), Stratospheric temperature increases due to Pinatubo aerosols, *Geophys. Res. Lett.*, **19**, 2, 207-210.

Levizzani, V. and M. Setvak (1996), Multispectral, high resolution satellite observations of plumes on top of convective storms, *J. Atmos, Sci*., **53**, 361-369.

Li, Z., R. Fraser, J. Jin, A. A. Abuelgasim, I. Csiszar, P. Gong, R. Pu, and W. Hao, 2003, Evaluation of algorithms for fire detection and mapping across North America from satellite, *J. Geophys. Res.*, **108(D2)**, 4076, doi:10.1029/2001JD001377.

Livesey, N., M. Fromm, J. Waters, G. Manney, M. Santee, and W. Read (2004), Enhancements in lower stratospheric CH3CN observed by UARS MLS following boreal forest fires, *J. Geophys. Res.*, **109** (D06308), doi:10.1029/2003JD004055.

Lucke R.L., D. Korwan, R.M. Bevilacqua, J.S. Hornstein, E.P. Shettle, D.T. Chen, M. Daehler, J.D. Lumpe, M.D. Fromm, D. Debrestian, B. Neff, M. Squire, G. König-Langlo, & J. Davies (1999), The Polar Ozone and Aerosol Measurement (POAM III) Instrument and Early Validation Results, *J. Geophys. Res.*, **104**, 18,785-18,799.

Luderer, G., J. Trentmann, T. Winterrath, C. Textor, M. Herzog, H. F. Graf, M. O. Andreae (2006), Modeling of biomass smoke injection into the lower stratosphere by a large forest fire (Part II): sensitivity studies, *Atmos. Chem. Phys.*, **6**, 5261-5277.

Marchand, R.T., T.P. Ackerman, and C. Moroney (2007), An assessment of Multi-angle Imaging SpectroRadiometer (MISR) stereo-derived cloud top heights and cloud top winds using ground-based radar, lidar and microwave radiometers. *J. Geophys. Res*., in press.

Mauldin, L.E., III, N.H. Zaun, M.P. McCormick, J.H. Guy, and W. Vaughn (1985), Stratospheric Aerosol and Gas Experiment II instrument: A functional description, *Opt. Eng.*, **24**, 307-312.

Minnis, P., Harrison, E., Stowe, L., Gobson, G., Denn, F., Doelling, D., Smith, W., (1993), Radiative climate forcing by the Mount-Pinatubo Eruption, *Science,* **259**, 1411-1415.

Moroney, C., R. Davies, and J-P. Muller (2002), Operational retrieval of cloud-top heights using MISR data. *IEEE Trans. Geosci. Remote Sens.*, **40**, 15-41.

Muller, J-P., A. Mandanayake, C. Moroney, R. Davies, D.J. Diner, and S. Paradise (2002), MISR stereoscopic image matchers: Techniques and results. *IEEE Trans. Geosci. Remote Sens.*, **40**, 1547-1559.

Nance, J., P. Hobbs, L. Radke, D. Ward (1993), Airborne measurements of gases and particles from an Alaskan wildfire, *J. Geophys. Res.*, **98**, 14873-14882.

Naud, C., J.-P. Muller, and E. E. Clothiaux (2002), Comparison of cloud top heights derived from MISR stereo and MODIS CO2-slicing, *Geophys. Res. Lett.,* **29**, Art. No. 1795.

Naud C., J.-P. Muller, M. Haeffelin, Y. Morille, and A. Delaval (2004), Assessment of MISR and MODIS cloud top heights through inter-comparison with a back-scattering lidar at SIRTA, *Geophys. Res. Lett.,* **31**, L04114.

Naud, C. M., J. P. Muller, E. C. Slack, C. L. Wrench, and E. E Clothiaux (2005a), Assessment of the performance of the Chilbolton 3-GHz advanced meteorological radar for cloud-top-height retrieval, *J. App. Meteor*., **44**, 866-877.

Naud, C. M., J.-P. Muller, E. E. Clothiaux, B. A. Baum, and W. P. Menzel (2005b), Intercomparison of multiple years of MODIS, MISR and radar cloud-top heights. *Annales Geophysicae*, **23**, 1–10.

Palm, S. P., M. Fromm, and J. Spinhirne (2005), Observations of Antarctic polar stratospheric clouds by the Geoscience Laser Altimeter System (GLAS), *Geophys. Res. Lett.,* **32**, L22S04, doi:10.1029/2005GL023524.

Penndorf, R. (1953), On the phenomenon of the colored sun, especially the “blue” sun of September 1950, AFCRC Technical Report 53-7, Air Force Cambridge Research Center, Cambridge, Massachusetts, 20, 41 pp.

Poulida, O., R. Dickerson, and A. Heymsfield (1996), Stratosphere-troposphere exchange in a midlatitude mesoscale convective complex 1. observations, *J. Geophys. Res.,* **101**, D3, 6823-6836.

Prata, A. J. (1989), Infared radiative transfer calculations for volcanic ash clouds, *Geophys. Res. Lett*., **16**, 11, 1293-1296.

Prata, A. J. and I. J. Barton (1993), A multichannel, multiangle method for the determination of infrared optical depth of semitransparent high cloud from an orbing satellite. Part I: Formulation and simulation, *J. Applied Meteor*., **32**, 7, 1623-1637.

Prata, A. J. and I. F. Grant (2001), Retrieval of microphysical and morphological properties of volcanic ash plumes from satellite data: Application to Mt. Ruapehu, New Zealand., *Q. J. R. Meteorol. Soc.*, **127** (576B), 2153-2179.

Pu, R., Z. Li, P. Gong, R. Fraser, I. Csiszar, W. Hao, S. Kondragunta, F. Weng (2007), Development and Analysis of a 12-year Daily 1-km Forest Fire Dataset across North America from NOAA/AVHRR Data, *Rem. Sens. Environ.*, **108**, 198-208, doi: 10.1016/j.rse.2006.02.027.

Pyne, S., and P. Omi (1986), Wildland Fires and Nuclear Winters: Selected Reconstruction of Historical Large Fires, Defense Documentation Center, DNA-TR-85-396, unclassified report to Defense Nuclear Agency, 167 pp, February 1986.

Randall, C.E., R.M. Bevilacqua, J.D. Lumpe and K.W. Hoppel (2001), Validation of POAM III Aerosols: Comparison to SAGE II and HALOE, *J. Geophys. Res*., **106**, 27,525-27,536.

Rauthe, M., M. Gerding, J. Höffner, and F.-J. Lübken (2006), Lidar temperature measurements of gravity waves over Kühlungsborn (54°N) from 1-105 km: a winter-summer comparison, *J. Geophys. Res*., doi. 10.10129/2006JD007354.

Reber, C.A., C.E. Trevathan, R.J. McNeal, and M.R. Luther (1993), The Upper Atmosphere Research Satellite (UARS) Mission", *J. Geophys. Res.*, **98**, 10,643-10,647.

Reid, J., R. Koppmann, T. Eck, and D. Eleuterio (2005a), A review of biomass burning emissions part II: intensive physical properties of biomass burning particles, *Atmos. Chem. Phys.*, **5**, 799-825.

Reid, J., T. Eck, S. Christopher, R. Koppmann, O. Dubovik, D. Eleuterio, B. Holben, E. Reid, J. Zhang (2005b), A review of biomass burning emissions part III: intensive optical properties of biomass burning particles, *Atmos. Chem. Phys.*, **5**, 827-849.

Remer, L. A., Y. J. Kaufman, D. Tanré, S. Mattoo, D. A. Chu, J. V. Martins, R.-R. Li, C. Ichoku, R. C. Levy, R. G. Kleidman, T. F. Eck, and E.; Vermote, (2005), The MODIS aerosol algorithm, products and validation. *J. Atmos. Sci.*, **62**, 947-973.

Ricchiazzi, P., S. Yang, and C. Gautier, (1998), SBDART: A research and teaching software tool for plane-parallel radiative transfer in the earth's atmosphere. *Bull. Amer. Meteor. Soc.,* **79,** 2101–2114.

Ritter, C., Kische, A., Neuber, R.(2004). Tropospheric Aerosol characterized by a Raman Lidar over Spitsbergen, 22nd International Laser Radar Conference (ILRC 2004) : 12 - 16 July 2004, Matera, Italy. Editors: Gelsomina Pappalardo, Aldo Amodeo. ESA Publications Div., 459-462. (ESA SP. 561), ISBN: 92-9092-872-7

Rizi, V., F. Masci, G. Redaelli, P. Di Carlo, M. Iarlori, G. Visconti, and L. Thomason (2000), Lidar and SAGE II observations of Shishaldin volcano aerosols and lower stratospheric transport, *Geophys. Res. Lett.*, **27**, 3445-3448.

Robock, A., (1991), Surface cooling due to forest fire smoke. *J. Geophys. Res.*, **96**, 20,869-20,878.

Robock, A., (2000), Volcanic eruptions and climate. Reviews of Geophyics **38**, 191-219.

Rose, W., Y. Gu, I. Watson, T. Yu, G. Bluth, A. Prata, A. Krueger, N Krotkov, S Carn, M. Fromm, D. Hunton, G. Ernst, A. Viggiano, T. Miller, J. Ballentin, J. Reeves, J. Wilson, B. Anderson, D Flittner (2003), The February-March 2000 eruption of Hekla, Iceland from a satellite perspective, *AGU Geophysical*

Monograph 139: Volcanism and the Earth's Atmosphere, ed by A Robock and C Oppenheimer, pp. 107-132, ISBN 0-87590-998-1.

Rose, W., D. Delene, D. Schneider, G. Bluth, A. Krueger, I. Sprod, C. McKee, H. Davies and G. Ernst (1995), Ice in the 1994 Rabaul eruption cloud: implications for volcano hazard and atmospheric effects, *Nature*, **375**, 477-479.

Rosen, J. M. (1964), The vertical distribution of dust to 30 km, *J. Geophys. Res.,* **69***,* 4673- 4676.

Rosenfeld, D., and I. Lensky (1998), Spaceborne sensed insights into precipitation formation processes in continental and maritime clouds, *The Bulletin of American Meteorological Society*, **79**, 2457-2476.

Rosenfeld, D., M. Fromm, J. Trentmann, G. Luderer, M. Andreae, R. Servranckx (2007), The Chisholm firestorm: observed microstructure, precipitation, and lightning activity of a pyro-cumulonimbus, *Atmos. Chem. Phys.*, **7**, 645-659.

Russell, J. M., III, L. Gordley, J. Park, S. Drayson, W. Hesketh, R. Cicerone, A. Tuck, J. Frederick, J. Harries, and P. Crutzen (1993), The Halogen Occultation Experiment, *J. Geophys. Res.,* **98**, 10,777-10,797.

Russell, P., J. Livingston, B. Schmid, J. Eilers, R. Kolyer, J. Redemann, S. Ramirez, J-H. Yee, W. Swartz, R. Shetter, C. Trepte, A. Risley, Jr., B. Wenny, J. Zawodny, W. Chu, M. Pitts, J. Lumpe, M. Fromm, C. Randall, K. Hoppel, R. Bevilacqua (2005), Aerosol optical depth measurements by airborne sun photometer in SOLVE II: Comparisons to SAGE III, POAM III and airborne spectrometer measurements, *Atmos. Chem. Phys.*, **5**, 1311-1339.

Sassen, K., and J. D. Horel, (1990), Polarization lidar and synoptic analyses of an unusual volcanic aerosol cloud. *J. Atmos. Sci.*, **47**, 2881-2889.

Sassen, K., T. Peter, B. P. Luo, and P. J. Crutzen, (1994), Volcanic Bishop's ring: Evidence for a sulfuric acid tetrahydrate particle aureole. *Appl. Opt.*, **33**, 4602-4606.

Siebert, J., C. Timmis, G. Vaughan, K. Fricke (2000), A strange cloud in the Arctic summer stratosphere 1998 above Esrange (68ºN), Sweden, *Ann. Geophys.,* **18,** 505-509.

Sigurdsson, H., B. Houghton, S. McNutt, H. Rymer, and J. Stix (2000), Encyclopaedia of Volcanoes, Academic Press, ISBN 012643140X, 1417 pp.

Stenchikov, G., M. Fromm, E. Shettle (2006), Study of long-range transport and stratosphere-troposphere exchange in smoke plumes from forest fires caused by aerosol solar heating", *Eos Trans. AGU,* 87(52), Fall Meet. Suppl., Abstract A43A-0114.

Stocks, B. and D. McRae (1991), The Canada/United States Cooperative Mass Fire Behavior and Atmospheric Environmental Impact Study, pp 478-487, *Proc. Eleventh Conf. Fire and For. Meteorol.*, April 16-19, 1991, Missoula, MT.

Stocks, B., Fosberg, M., Lynham, T., Mearns, L., Wotton, B., Yang, Q., Jin, J-Z., Lawrence, K., Hartley, G., Mason, J., and McKenney, D., (1998), Climate change and forest fire potential in Russian and Canadian boreal forests. *Climatic Change*, **38(1)**, 1-13.

Swinbank, R. and A. O'Neill (1994), A stratosphere-troposphere data assimilation system, *Mon. Weather Rev*., **122**, 686-602.

Thomason, L., L. Poole, and T. Deshler (1997), A global climatology of stratospheric aerosol surface area density as deduced from SAGE II: 1984-1994, *J. Geophys. Res*., **102**, 8967-8976.

Toon, O., Robock, A., Turco, R., Bardeen, C., Oman, L., (2007), Nuclear war - Consequences of regional-scale nuclear conflicts. *Science*, **315,** 1224-1225.

Torres, O., P. K. Bhartia, J. R. Herman, Z. Ahmad, J. Gleason (1998a), Derivation of aerosol properties from satellite measurements of backscattered ultraviolet radiation: Theoretical basis, *J. Geophys. Res.*, **103(D14)**, 17099-17110.

Torres, O., P. K. Bhartia, J. R. Herman, Z. Ahmad, J. Gleason (1998b), Correction to "Derivation of aerosol properties from satellite measurements of backscattered ultraviolet radiation: Theoretical basis" by Torres et al., *J. Geophys. Res.,* **103(D18)**, 23321-23322, 10.1029/98JD02709.

Torres O., P.K. Bhartia, J.R. Herman, A. Sinyuk, P. Ginoux, and B. Holben (2002a), A Long-term record of aerosol optical depth from TOMS observations and comparison to AERONET measurements, *J. Atmos. Sci.*, **59(3)**, 398-413.

Torres, O., R. Decae, J.P. Veefkind, and G. de Leeuw (2002b): OMI Aerosol Retrieval Algorithm, in OMI Algorithm Theoretical Basis Document: Clouds, Aerosols, and Surface UV Irradiance, Vol. 3, version 2, (OMI-ATBD-03, P. Stammes, Ed.), http://eospso.gsfc.nasa.gov/eos_homepage/for_scientists/atbd/docs/OMI/ATBD-OMI-03.pdf.

Torres, O., P. K. Bhartia, A. Syniuk, and E. Welton (2005),TOMS Measurements of Aerosol Absorption from Space: Comparison to SAFARI 2000 Ground-based Observations, *J. Geophys. Res.*, **110**, D10S18, doi:10.1029/2004JD004611.

Trentmann, J., G. Luderer, T. Winterrath, M. D. Fromm, R. Servranckx, C. Textor, M. Herzog, H.-F. Graf, M. O. Andreae (2006), Modeling of biomass smoke injection into the lower stratosphere by a large forest fire (Part I): reference simulation, *Atmos. Chem. Phys.*, **6**, 5247-5260.

Trickl, T., O. C. Cooper, H. Eisele, P. James, R. Mücke, A. Stohl (2003), Intercontinental transport and its influence on the ozone concentrations over central Europe: three case studies, *J. Geophys. Res.* **108**, 8530, doi:10.1029/2002JD002735, STA 15, 23 pp.

Tupper A., J. S. Oswalt, D. Rosenfeld (2005), Satellite and radar analysis of the volcanic-cumulonimbi at Mount Pinatubo, Philippines, 1991, *J. Geophys. Res.*, **110**, D09204, doi:10.1029/2004JD005499.

Turco, R., O. Toon, T. Ackerman, J. Pollack, and C. Sagan (1983), Nuclear winter: Global consequences of multiple nuclear explosions, *Science,* **222**, 1283-1292.

Waibel, A.E., H. Fischer, F.G. Wienhold, P.C. Siegmund, B. Lee, J. Ström, J. Lelieveld, and P.J. Crutzen (1999), Highly elevated carbon monoxide concentrations in the upper troposphere and lowermost stratosphere at northern midlatitudes during the STREAM II summer campaign in 1994, *Chemosphere: Global Change Science*, **1**, 233-248.

Wallace, J. and P. Hobbs (1977), *Atmospheric Science: An Introductory Survey*, Academic Press, ISBN 0-12-732950-1.

Wang, P., M. McCormick, L. Poole, W. Chu, G. Yue, G. Kent, and K. Skeens (1994), Tropical high cloud characteristics derived from SAGE II extinction measurements, *Atmos. Res.,* **34**, 53-83.

Wang, P. K., (2007), The thermodynamic structure atop a penetrating convective thunderstorm, *Atmos. Res.*, **83**, 252-262.

Wen, S. and W. Rose (1994), Retrieval of sizes and total masses of particles in volcanic clouds using AVHRR bands 4 and 5, *J.Geophys. Res.*, **99**, 5421-5431.

Westerling, A. L., Hidalgo, H. G., Cayan, D. R., Swetnam, T. W. (2006), Warming and earlier spring increase western US forest wildfire activity. *Science*, **313**, 940-943.

Westphal, D., and Toon, O., (1991), Simulations of microphysical, radiative, and dynamic processes in a continental-scale forest-fire smoke plume, *J. Geophys. Res.* **96**, 22379-22400.

Winker, D., W. Hunt, and C Hostetler (2004), Status and performance of the CALIOP lidar, *Proc. SPIE*, 5575, 8-15.

Yamanouchi, T., K. Suzuki, and S. Kawaguchi (1987), Detection of clouds in Antarctica from infrared multispectral data of AVHRR, *J. Meteorol. Soc*., **65**, 949-961.

Yang, P., L. Zhang, G. Hong, S. L. Nasiri, B. A. Baum, H. L. Huang, M. D. King, and S. Platnick (2007), Differences between collection 4 and 5 MODIS ice cloud optical/microphysical products and their impact on radiative forcing simulations. *IEEE Trans. Geosci. Remote Sens.* (In Press).

Zanis, P., T. Trickl, A. Stohl, H. Wernli, O. Cooper, C. Zerefos, H. Gaeggeler, A. Priller, C. Schnabel, H. E. Scheel, H. J. Kanter, L. Tobler, P. W. Kubik, P. Cristofanelli, C. Forster, P. James, E. Gerasopoulos, A. Delcloo, A. Papayannis, H. Claude (2003), Forecast, observation and modelling of a deep stratospheric intrusion event over Europe, *Atmos. Chem. Phys*. **3**, 763-777.

Zong, J., R. Davies, J-P. Muller, and D.J. Diner (2002), Photogrammetric retrieval of cloud advection and top height from the Multi-angle Imaging

SpectroRadiometer (MISR). *Photogramm. Eng. and Remote Sens.* **68**, 821-829.